POLITECNICO
MILANO 1863

SCUOLA DI INGEGNERIA INDUSTRIALE
E DELL'INFORMAZIONE

A Convexified Model Predictive Approach to SAR Satellites Formation Control

Tesi di Laurea Magistrale in
Space Engineering - Ingegneria Spaziale

Author: **Federico Guerinoni**

Student ID: 920705
Advisor: Prof. Michèle Lavagna
Co-advisor: Stefano Silvestrini
Academic Year: 2020-21

Abstract

Spaceborne Synthetic Aperture Radar (SAR) in the last two decades have become a reference technology in the fields of Earth imaging and monitoring. To overcome the intrinsic limitations of monolithic SAR missions, in the last years efforts have been made worldwide in the design of multi-static SAR missions, to achieve better results and add strong flexibility in the design. In this context, the work proposed focuses on the design of a control logic with a Model Predictive Control (MPC) based approach for a typical single-pass SAR interferometry mission, defined in its essential features. The overall control strategy is based on maintaining the Height of Ambiguity (HoA), one of the most important parameters for DEM generation, inside a small range. In particular two case studies are considered with different HoA ranges, adaptable to a large basin of landscapes and regions on the Earth's surface. Following the objective of implementing a computationally light controller to reduce the consumption of on-board resources, the MPC approach employs a linearised relative dynamics model including J_2 and differential drag perturbations to compute δv-optimal control actions. To fasten the controller performances, the original non-linear optimal control problem is convexified through an iterative technique and transformed into sequential second-order cone programming (SOCP) sub-problems, easily solved by state of the art interior-point algorithms. The results have been validated with a high-fidelity propagator including atmospheric drag and gravitational perturbations up to the fourth order. The main purpose of the validation campaign is to verify whether the impulsive solutions found by the algorithms, basing on a simplified model, can hold true also in a more detailed environment of simulation keeping the HoA (at least) in a close neighborhood of the desired behaviour. The campaign shows that, for both the case studies, the results can be in general considered valid over several orbits.

Keywords: SAR, convexification, model predictive control, height of ambiguity

Abstract in lingua italiana

Le applicazioni spaziali dei Radar ad Apertura Sintetica (SAR) nelle ultime due decadi sono diventate una tecnologia di riferimento per il monitoraggio e la mappatura terrestri. Per superare i limiti intrinseci di missioni monolitiche con SAR, negli ultimi si è sviluppata la tendenza al progetto di missioni SAR multi-statiche, che permettono di raggiungere migliori risultati e maggiore flessibilità nel design, In questo contesto, il lavoro qui proposto si focalizza sul progetto di un controllore con Controllo Predittivo basato su Modello (MPC) per una tipica missione SAR a singolo passaggio, definita nei sui tratti essenziali. La strategia di controllo sviluppata si basa sul mantenimento dell'Altezza di Ambiguità (HoA), uno dei parametri fondamentali nella generazione di Modelli Digitali di Elevazione (DEM), in un intervallo ristretto. Nello specifico, due casi studio sono stati considerati con diversi intervalli di HoA, adattabili a numerosi paesaggi sulla superifie terrestre. Per ridurre il consumo delle risorse di bordo, l'approccio MPC implementa un modello di dinamica relativa linearizzato, che comprende effetto J_2 e resistenza atmosferica differenziale, per ottimizzare le manovre. Per velocizzare le prestazioni del controllore, il problema originale non lineare da ottimizzare è stato convessificato tramite un metodo iterativo e trasformato in successivi sotto-problemi conici del secondo ordine (SOCP), agilmente risolti dagli algoritmi di interior-point odierni. I risultati ottenuti sono stati validati per mezzo di un propagatore ad alta fedeltà, che include resistenza atmosferica e perturbazioni del potenziale gravitazionale fino al quarto ordine. Lo scopo principale della validazione è stato quello di verificare che le manovre programmate dagli algoritmi, basati su un modello semplificato, potessero valere anche in un ambiente di simulazione più raffinato, mantenendo la HoA in un introrno stretto dell'andamento desiderato. La campagna ha dimostrato che per entrambi i casi studi, i risultati ottenuti possono essere considerati validi entro per svariate orbite.

Parole chiave: SAR, convessificazione, controllo predittivo modello, altezza di ambiguità

Contents

1 | Introduction

Spaceborne *Synthetic Aperture Radar* (SAR) in the last two decades have become a reference technology in the fields of Earth imaging and monitoring. What makes this instrument so appealing is the independence of its resolution on the flight altitude: a characteristic that introduces a lot of potential and flexibility into Synthetic Aperture Radar imaging. In addition to this, other remarkable advantages of this sensor are the day and night, weather-independent imaging capabilities, the very small resolutions are achievable and the large basin of possible applications (mapping and monitoring from space, topography, oceanography, moving target indication and more on [2]). In particular, with interferometry it's possible to differently combine two SAR images of the same region to retrieve various information, depending on the conditions in which the two pictures were taken. Among the most interesting applications there is the possibility of generating *Digital Elevation Models* (DEM), three dimensional computer graphics representations of a region's topology, starting from interferograms, to monitor the evolution of the Earth's surface.

1.1. SAR Missions

A key parameter for DEM generation is the Height of Ambiguity (HoA), a measure of the accuracy of the interferograms: the smaller the HoA, the lower is the influence of errors in the images caused by the instrument or the decorrelation effects. On the other hand, strong variations in the topography of a region, like sudden jumps, can only be resolved correctly if the height of ambiguity is larger than the jump height. Looking at Figure 1.1 it's possible to see how this parameter influences the accuracy of the interferograms and the related DEM.
Along with the HoA, another important factor that determines the quality of the interferograms is the time interval between the two SAR pictures acquisition, that should be kept as low as possible to enable a proper correlation of the images. Monolithic SAR mission in this sense are intrinsically limited, because of days-to-weeks revisit time constraints,

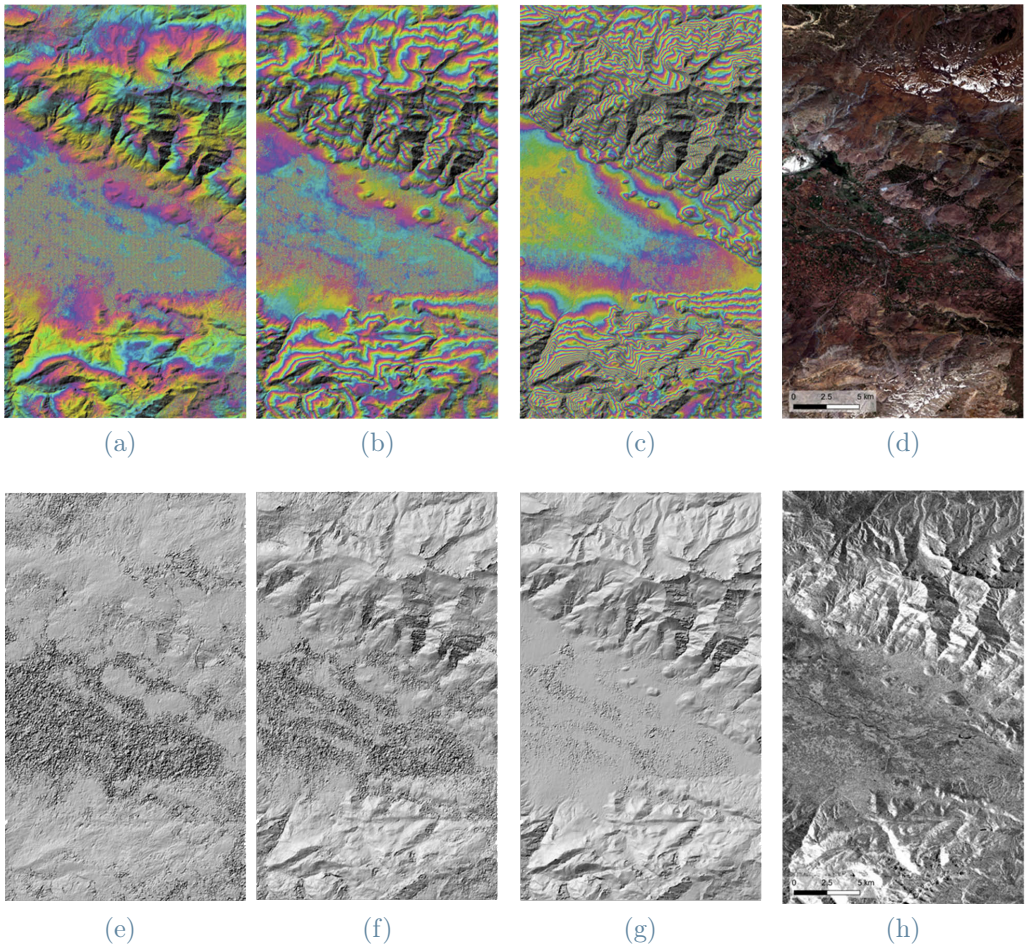

Figure 1.1: Comparison between interferograms (upper row) and associated DEM (bottom row) generated with different heights of ambiguity. From left to right, the images refer to heights of ambiguity of 540 m, 218 m and 97 m. Images (d) and (h) show optical and radar pictures of the same region for comparison.
Credits: Andreas Braun, Open Geosciences [3].

and employ a repeat-pass strategy to acquire the different pictures with multiple passages over the same area. To overcome this condition, in the last years many efforts have been made worldwide in the design of multi-static single-passage SAR missions [4, 25, 26], relying on multiple platforms flying at short distances to reduce (or even cancel) the interval between acquisitions, drastically increase the quality of the results and enhance flexibility in the missions design, along with all the advantages of a distributed satellite system. It's important to point out that the usual common factor for all these multi-static missions designs is the implementation of ground-in-the-loop formation control. However, considering the strong advantages of the research in the field of autonomous guidance, navigation and control of formation flying spacecrafts that has been made, it's of natural

interest to wander which could be the possibilities of implementation for this technology in a distributed SAR system. In this sense, the most important step that has been made is the TanDEM-X Autonomous Formation Flying (TAFF) Experiment [1], a demonstrative experience integrated inside an operative mission to verify the capabilities of autonomous formation flying SAR systems and assess the advantages in terms of scientific return. The experiment succeeded, demonstrating that the on-board system could correctly control the formation during its scientific operations and that significant improvements can be obtained in the control optimisation without the limitations of ground-visibility constraints for the manoeuvres planning and execution.

1.2. Thesis Objectives and Outline

The work proposed in this paper focuses on the design of an autonomous control strategy to implement on-board a multi-static SAR mission. The strict scientific requirements imposed to the mission require to maintain the height of ambiguity inside a defined range of ± 2 m around an objective value to enable data collection. Two different case studies have been considered, taking as reference two different values for the HoA, 50 m and 150 m, realistically adaptable to various situations and landscapes on Earth.
In Chapter 2, a more detailed dissertation on SAR and its functioning is carried on, particularly focusing on its applications through interferometry and the definition of the main formation's parameter and how they influence the scientific activities. Along with this, it is introduced the state-of-the-art relative dynamics model embedded in the control logic definition. Chapter 3 starts by introducing the operative scenario selected, setup inside the frame of a typical present-day mission and tacking inspiration from recent missions for the definition of the payload to employ and the absolute orbits. Then, the control strategy proposed is analysed in deep and the control problem formulation is introduced. In Chapter 4 this is reprised and detailed through the description of the algorithms implemented both for the maintenance and the reconfiguration of the formation in the two case studies considered. Chapter 5 presents the results of an extensive simulation campaign, aimed at verifying the behaviour and the results of the algorithms under different conditions. To conclude, Chapter 6 presents the outcomes of the validation process for the results introduced in the previous chapter.

2 | State Of the Art

2.1. Synthetic Aperture Radar Fundamentals

Synthetic Aperture Radar (SAR) is a multi-purpose class of active remote sensing instruments widely employed nowadays. As its name suggests, this class of radars mimics a very large, fictitious, aperture to overcome the intrinsic limitations of real aperture radars (RAR) and obtain high resolution images with a compact hardware. To achieve the synthetic aperture effect, the radar needs to be located on a moving platform: as its travels through space sending pulses, it can illuminate a target region on the surface of the Earth from different positions. Then, properly combining each of the images captured it's possible to recreate the effect of a larger aperture antenna. A typical spaceborne SAR acquisition geometry is represented in Figure 2.1.

SAR images are obtained illuminating a certain region of interest with an electromagnetic pulse. As the wave impacts the ground, it scatters and spreads in every direction, thus a small fraction of the transmitted signal echoes and returns back to the antenna. The information embedded in these backscatters (both amplitude and phase of the waves) are then recorded and post-processed to reconstruct the images. SAR bi-dimensional pictures are acquired inside a plane given by the flight and the slant range (or look) directions, called the *reference plane* or the *slant-azimuth plane*. This plane is divided in cells, called *resolution cells*, and each pixel in the image corresponds to a resolution cell on the reference plane (Figure 2.2). The dimensions of a cell define the azimuth (δ_a) and slant range (δ_r) resolutions, computed as

$$\delta_a = \frac{\lambda}{L_{sa}} R = \frac{L_a}{2} \tag{1.a}$$

$$\delta_r = \frac{c\tau}{2} \tag{1.b}$$

where λ is the transmitted signal wavelength, L_{sa} is the synthetic aperture equivalent antenna length, L_a is the antenna dimension parallel to the flight direction, c is the speed of light and τ is the signal transmission duration.

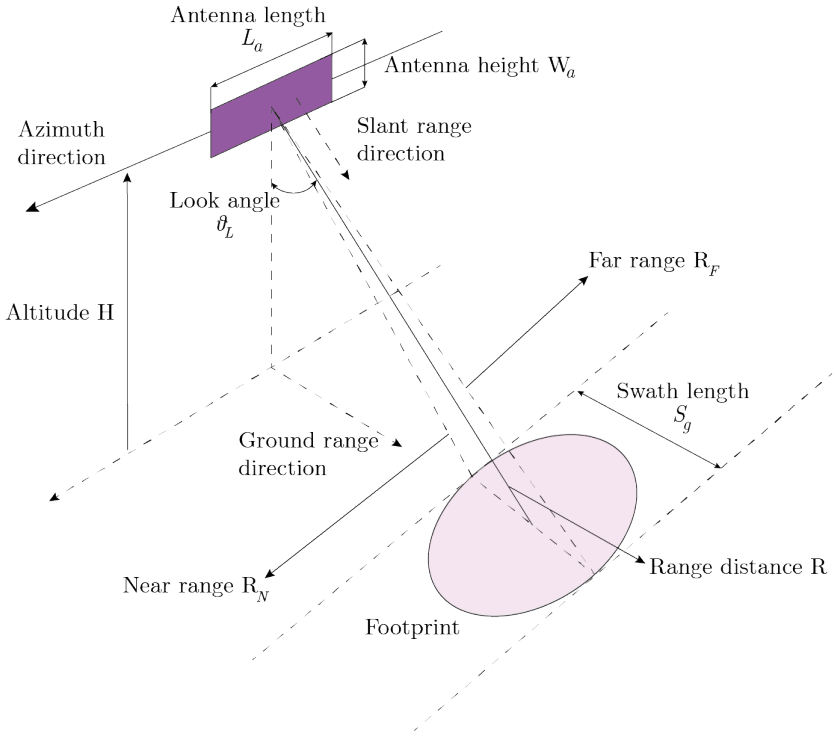

Figure 2.1: classic SAR acquisition geometry and its relevant parameters.
The purple rectangle represents the antenna mounted on the platform, with dimensions W_axL_a. The antenna is side-looking, inclined with an angle θ_L with respect to the nadir, and transmits pulses that describe a cone in space whose axis coincides with the slant range direction. The pink ellipsoid is the footprint of the beam on the ground.
Sectioning vertically the signal cone, the near and far range are defined (respectively) as the distances to the footprint's closest and the furthest points from the antenna.
The difference of their projections on the ground range direction is the swath length S_g.

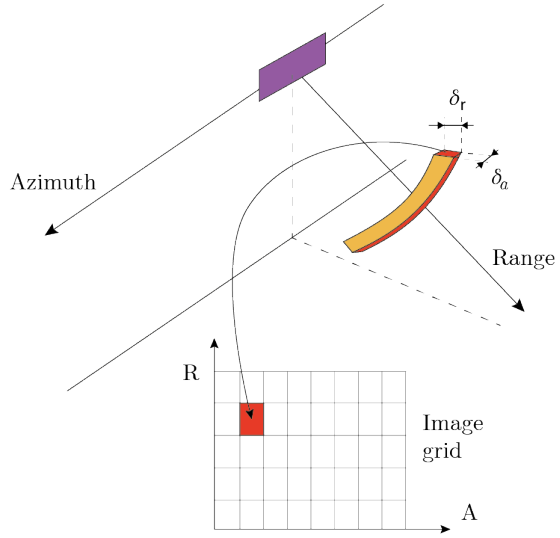

Figure 2.2: resolution cells and reference plane of SAR images.
Each cell has dimensions δ_a x δ_r and describes a slice in space with fixed range-azimuth coordinates. The echoes coming from the portion of the ground with those range-azimuth coordinates, will be imprinted in the pixel related to that cell.

Interferometry is one of the more prolific applications of spaceborne SAR. It's a technique employed to extract various information from different images of the same region. Each pixel of an image is associated to a complex value, representing the backscattered information (phase and amplitude) from the corresponding resolution cell on ground. The amplitude of the echo depends on various and usually poorly manipulable factors, but the phase instead consists mainly of three terms [20]:

- the two-way travel path from the sensor to the target
- the interaction between the incident signal and the scattering surface
- a phase shift introduced by the processing system

The first contribute, embedding the information on the traveled length, is the most interesting for interferometry. In particular, it's possible to demonstrate [18] that by taking two pictures of the same region "under the same conditions" but from slightly different positions, the difference in the paths traveled by the echoes create a phase difference in the pictures, and properly combining this phase information it's possible to reconstruct the elevation h_P on ground of the observed point:

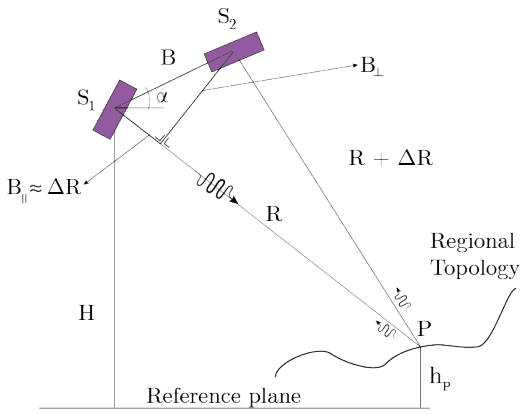

(a)

Figure 2.3: Geometry of SAR interferometry. S_1 represents the deputy, acting both as transmitter and receiver, while S_2 is the deputy.

$$h_P = -\frac{\lambda R \sin\theta_L}{4\pi B_\perp}\partial\Phi \tag{2.1}$$

where R is the slant-range distance and $B_\perp$ the component of the spacecrafts baseline perpendicular to the slant direction, denoted as *perpendicular baseline* (Figure 2.3). The term $\partial\Phi$ identifies the contribute to the phase shift introduced by a point with altitude different from zero. Indeed, the total phases difference $\Delta\Phi$ between the pictures can be considered as the results of two contributes: a $\Delta\Phi_{ref}$, the shift introduced by points on a reference flat-Earth plane, and the correction $\partial\Phi$ introduced by differences of elevation with respect to the reference. The constant term of the reference surface is

$$\Delta\Phi_{ref} = \frac{4\pi}{\lambda} B \sin(\theta_L - \alpha) \tag{2.2}$$

and the phases difference

$$\Delta\Phi = \Delta\Phi_{ref} + \partial\Phi. \tag{2.3}$$

By taking the complex conjugate of one of the two images and summing them, it's possible to obtain a map of the relative phase (or interferometric phase) between the two picutres: the interferogram. Since phases are always ambiguous with respect to integer multiples of 2π, and generally $\Delta R \gg \lambda$, in interferograms the phases difference undergoes multiple cycles in the $[0, 2\pi]$ interval called "fringes", and represented with a range of colours. By looking at Equation 2.1 it's possible to note that a 2π phase difference corresponds to a

$$h_{2\pi} = \frac{\lambda R_1 \sin\theta_L}{2B_\perp} \tag{2.4}$$

height variation, where $h_{2\pi}$ it's the height of ambiguity. This is a key parameter in SAR interferometry, that represents the sensitivity of the generated interferogram to altitude variations in the terrain and strongly influences the quality of the images necessary for the DEM generation. In interferometric SAR missions, depending on the region of interest it might be necessary to change the formation parameters and adapt the value of the height ambiguity.
Furthermore, as outlined above, two images can be interfered only if they're captured "in the same conditions". In principle, the two images can be taken at different instants, depending on the orbit geometry even after months. But not every pair of pictures can be interfered: it's required a certain level of correlation between the two, the risk otherwise is to obtain somehow corrupted results, even with pictures of the very same area. This is the concept of *coherence*. Coherence (γ) is a measurement of the correlation level between radar pictures. It ranges from 0 (un-correlated pictures) to 1 (complete correlation). There are numerous sources of decorrelation, and for each of them the coherence factor can be computed. The product of all these factors represent the total coherence of the images.
Generally speaking, values of coherence above $0.35 - 0.4$ are considered quite reliable [6]. There are two principal sources of decorrelation

- **temporal decorrelation**: by taking the second picture long after the first atmospheric agents, seasons, weather, geological effects and even mankind might determine sufficiently large changes in the reflective surface of the ground such that the interaction with the signal coming from the radar is altered, determining a loss of coherence. Beyond a certain limit pictures become un-correlated, and can't be interfered anymore.

- **spatial decorrelation**: the backscattering from the ground elements can be modeled as a particular case of reflective antenna. Thus, depending on the directions they're looked from, a different fraction of the original signal can be observed. The higher is the distance between the imaging spots, the higher is the effect of "random" variations between the pictures.

The second source in particular can be separated in two distinct cases: *baseline decorrelation* and *rotational decorrelation* [12]. The first verifies for too large values of the perpendicular baseline. From mathematical definitions, it's possible to estimate both the

coherence and the critical value of $B_\perp$, beyond which the images become un-correlated:

$$\gamma_{base} = 1 - \frac{2B_\perp}{\lambda R \tan\theta_L}\delta_r \tag{2.5}$$

$$B_\perp^{crit} = \frac{\lambda R \tan\theta_L}{2\delta_r} \tag{2.6}$$

The same considerations hold for the case of *rotational decorrelation*, arising when the along-track distance δr_t parallel to the flight direction between the antennas becomes too large

$$\gamma_{rot} = 1 - \frac{2\delta_a \sin\theta_L}{\lambda} \cdot \frac{\delta r_t}{R} \tag{2.7}$$

$$\delta r_t^{crit} = \frac{\lambda R}{2\delta_a \sin\theta_L} \tag{2.8}$$

However, to avoid inferring too much on the gathered data reliability for the work under presentation it has been decided to set as maximum limits for the perpendicular baseline and the along-track distance the 10% of their critical values.

2.2. Dynamical Models

In the context of single-pass SAR interferometry missions, given the strict correlation between the mission objectives (perpendicular baseline) and the relative position of the platforms, a relative dynamics model can be easily implemented in the GNC subsystem design. In this sense, in the field of Formation Flying in the late years several models have been developed to describe the evolution of formations subject to various environmental perturbations. This wide literature can be organised basing on various and different topics: linearised or non-linear models, with a state representation based on Cartesian coordinates, orbital elements or other parameters, models that apply for eccentric or near-circular orbits, and more again. For the scope of this work, the research of a feasible relative dynamics model to implement in the definition of a computationally fast optimal control logic focuses first of all on the class of linearised models. Furthermore, since generally SAR antennas gather a huge amounts of data during imaging, it is decided to enlighten the computational effort required to the on-board resources by considering the sub-class of linearised models. Considering the typical operational environment of a SAR mission (near-circular low-Earth orbits), it was possible to further focus the research on models based on a reference orbits with small eccentricity, capable of accounting at least for atmospheric drag and J_2, the two most important sources of perturbation in LEO.

Within this frame, the choice fell on the model developed by D'Amico [7], for multiple reasons. First of all its simplicity: it's a linear relative motion model that adopts the quasi non-singular relative orbital elements (ROE) state vector representation, with the mean argument of latitude as temporal variable. The ROE state vector comprises the relative semi-major axis, the relative mean longitude and the relative eccentricity/inclination vectors, well-known practical entities that provide a concrete insight on the relative orbit's geometry and introduce the concept of passive-safety formation design. Also, this model includes first-order secular effects of J_2 and differential drag for the spacecrafts. The second reason of this choice, it's the heritage. This model has been extensively employed in the literature [11, 23, 24] for the development of new formation design and control concepts, especially after the flight validation attained flying on-board missions like PRISMA [8, 22], GRACE [13, 16] and TanDEM-X [1, 15], that made it an undisputed reference in this field.

3 | Problem Modeling

This chapter introduces the work done starting from the setup of the problem and the first parameters definition, for both the radar and the orbits of the satellites. Among the most important topics included it's possible to find the modeling assumptions for the radar, the dynamics models employed to describe the spacecraft's motion and the control strategy selected for the mission.

3.1. Payload Design

The purpose of this work is to demonstrate how the proposed control strategy can be included in the context of modern-day or short-future SAR missions to obtain interferograms with tight height of ambiguity requirements. Therefore, for the payload design it can be useful to consider the state of the art and have a look at how in recent SAR missions the key parameters of the system have been selected. Table 3.1 reports these values for four recent missions: TanDEM-X, NovaSAR, ICEYE and ALOS-2 [9, 17, 29].

Mission	TanDEM-X	NovaSAR	ICEYE	ALOS-2
Antenna Length	4.78 m	3 m	3.2 m	9.9 m
Antenna Height	0.7 m	1 m	0.4 m	2.9 m
Carrier Frequency	9.65 GHz	3.2 GHz	9.65 GHz	1.2 GHz
Signal Bandwidth	100 MHz	100 MHz	30-300 MHz	60 MHz
Slant Range Resolution	6-12 m	6 m	3 m	3-10 m
Incidence Angle	20-45°	16-34°	15-35°	8-70°

Table 3.1: Recent important SAR missions and relative antenna parameters.

The definition of the radar parameters for this work is freely conducted taking this table as a reference, along with some general design considerations to keep into account when dealing with SAR systems [5, 19, 28].
Being located on a moving platform, a Doppler shift is introduced in the echoes from the target region to the antenna. To avoid aliasing the antenna Pulse Repetition Frequency (PRF, the reciprocal of the transmission interval between consecutive pulses, Figure 3.1)

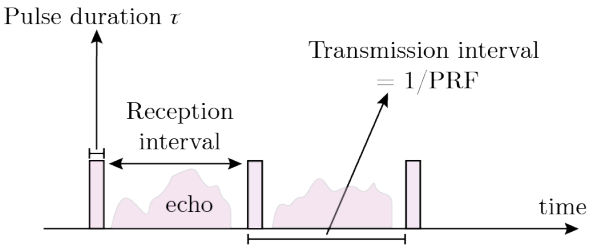

Figure 3.1: Transmission mechanism and its relevant parameters. The pulse duration is the reciprocal of the signal bandwidth. The reception interval must be sufficiently long to permit even the reception of the echoes coming from the furthest points, that is the far range R_F

shall be higher than

$$2\frac{\mathrm{v}}{L_a} = \frac{\mathrm{v}}{\delta_a} \leq PRF$$

where v is the platform velocity. This means that the transmissions shall occur at least once every $L_a/2$ meters travelled. Hence, the lower the antenna length, the higher the minimum PRF required. However, the time interval between consecutive pulses transmission cannot be arbitrarily short, otherwise the backscatters of different pulses from near and far range would overlap. In particular, making the hypothesis of flat-Earth and flat-terrain to consider equivalent the look and the incidence angles:

$$PRF \leq \frac{c}{2(R_F - R_N)} \approx \frac{c}{2S_g \sin\theta_L}$$

where S_g is the swath width and R_N, R_F the near and far ranges. To sum up:

$$\frac{v}{\delta_a} \leq PRF \leq \frac{c}{2S_g \sin\theta_L}$$

Thus, it's evident that by selecting a too small resolution in the azimuth direction the coverage capabilities of the radar get strongly reduced. It's important to follow the design keeping in mind that conflicts may arise between different requirements, and (often) trade-offs might be necessary.
The parameters adopted for this work are reported in Table 3.2.
Following the same approach, the absolute orbit of the chief spacecraft has been designed keeping into account the reference values of the missions listed above. It is a near-circular sun-synchronous orbit, with the sun-direction perpendicular to the line of nodes. Since SAR instruments have strong power requirements, they are usually operated in sunlit conditions. The last requirement permits therefore to maximise the scientific activity of the

Parameter	Value
Antenna Length	4 m
Antenna Height	1 m
Carrier Frequency	3 GHz
Signal Bandwidth	70 MHz
PRF	3800 Hz
Look Angle	25-40°
Azimuth Resolution	2 m
Slant Range Resolution	6 m
Swath Width	60-90 km
Look-side	Left

Table 3.2: SAR parameters selected for the mission.

spacecrafts during the orbits, avoiding zones of shadow. The selected orbital parameters can be found in Table 3.3.

Orbital Element	Value
Semi-Major Axis	6891 km
Eccentricity	0.0015
Inclination	97.46°
Arg. of Perigee	0°
β angle	82.54°

Table 3.3: Selected orbital elements for the chief spacecraft.

3.2. Spacecraft's Dynamics

Being a remote sensing instrument, SAR missions usually are operated in the context of highly inclined Low Earth Orbits (LEOs), because of the short periods and the mapping capabilities. It is well known that in this environment the major orbital perturbations are due to aerodynamic drag and the J_2 effect: it is therefore of primary importance to study and model adequately these effects.

The spacecraft's motion has been simulated by means of two different models: an absolute dynamics model, necessary to determine the altitude variations (primarily caused by drag) and the consequent changes in the atmosphere's density, and a relative dynamics model, to describe the formation's behaviour.

The absolute dynamics model employed is a high-fidelity propagator that numerically

integrates the equation of motion:

$$\ddot{\boldsymbol{r}} = -\frac{\mu}{r^3}\boldsymbol{r} + \boldsymbol{a}_{pert} \tag{3.1}$$

expressed in the ECI reference frame, where μ is the gravitational parameter of the central body, $\boldsymbol{r}$ represents the spacecraft's position vector, $\ddot{\boldsymbol{r}}$ the acceleration vector and $\boldsymbol{a}_{pert}$ is a general perturbing acceleration. The propagator is embedded into Simulink's *Orbit Propagator* block from the *Aerospace Blockset* library, and can be extended to include J_2 perturbation. Air drag instead was modeled autonomously and then fed to the propagator as perturbation:

$$\boldsymbol{a}_{drag} = -\frac{1}{2}\beta\rho v_{rel}^2 \frac{\boldsymbol{v}_{rel}}{||\boldsymbol{v}_{rel}||} \tag{3.2}$$

in which $\boldsymbol{v}_{rel}$ is the relative velocity of the spacecraft with respect to the rotating atmosphere and ρ is the atmosphere's density. The ballistic coefficient

$$\beta = \frac{c_D A_{cross}}{m_{s/c}} \tag{3.3}$$

is derived by A_{cross}, the cross-sectional area of the spacecraft perpendicular to $\boldsymbol{v}_{rel}$, the drag coefficient c_D and the spacecraft's mass $m_{s/c}$. The atmosphere's density is approximated with an exponential model of the type:

$$\rho(h) = \rho_0 \exp\left[-\frac{h - h_0}{h_{scale}}\right]$$

where h is the orbit altitude, ρ_0 the reference density and h_0 and h_{scale} the base altitude and the scale height of the model [27].
The relative dynamics model instead is employed to describe the relative motion of one of the spacecrafts, denoted as *deputy* (subscript "d"), with respect to the other, labeled as *chief* (subscript "c"). This model is set inside the Hill's reference frame (or Local-Vertical-Local-Horizontal frame), centered on the chief and defined by the vectors triad ($\boldsymbol{o}_r$, $\boldsymbol{o}_t$, $\boldsymbol{o}_n$) such that:

- $\boldsymbol{o}_r$ is aligned with the radius $\boldsymbol{r}_c$ of the chief and defines the *radial direction*, positive away from the Earth
- $\boldsymbol{o}_n$ points along the chief's orbit angular momentum, and defines the *normal*, or *out-of-plane* direction
- $\boldsymbol{o}_t$ completes the right-handed coordinate system defining the *tangential* or *along-*

track direction.

In this frame the relative state of the spacecraft can be represented either by Cartesian coordinates

$$\delta \boldsymbol{x}_{car} = \begin{pmatrix} \delta r_r \\ \delta r_t \\ \delta r_n \\ \delta v_r \\ \delta v_t \\ \delta v_n \end{pmatrix} = \begin{pmatrix} \Delta \boldsymbol{r} \cdot \boldsymbol{o}_r \\ \Delta \boldsymbol{r} \cdot \boldsymbol{o}_t \\ \Delta \boldsymbol{r} \cdot \boldsymbol{o}_n \\ \Delta \boldsymbol{v} \cdot \boldsymbol{o}_r + \Delta \boldsymbol{r} \cdot \dot{\boldsymbol{o}}_r \\ \Delta \boldsymbol{v} \cdot \boldsymbol{o}_t + \Delta \boldsymbol{r} \cdot \dot{\boldsymbol{o}}_t \\ \Delta \boldsymbol{v} \cdot \boldsymbol{o}_n + \Delta \boldsymbol{r} \cdot \dot{\boldsymbol{o}}_n \end{pmatrix} \tag{3.4}$$

where $\Delta \boldsymbol{r} = \boldsymbol{r}_d - \boldsymbol{r}_c$ and $\Delta \boldsymbol{v} = \boldsymbol{v}_d - \boldsymbol{v}_c$ and the dotted quantities represent time derivatives, or by relative orbital elements (ROE) through a non-linear combination of the quasi non-singular orbital elements of the spacecrafts

$$\delta \boldsymbol{x}_{roe} = \begin{pmatrix} \delta a \\ \delta \lambda \\ \delta e_x \\ \delta e_y \\ \delta i_x \\ \delta i_y \end{pmatrix} = \begin{pmatrix} (a_d - a_c)/a_c \\ u_d - u_c + (\Omega_d - \Omega_c)\cos i_c \\ e_{x,d} - e_{x,c} \\ e_{y,d} - e_{y,c} \\ i_d - i_c \\ (\Omega_d - \Omega_c)\sin i_c. \end{pmatrix} \tag{3.5}$$

where δa is the relative semi-major axis, $\delta \lambda$ is the mean longitude, $\delta \boldsymbol{e}$ and $\delta \boldsymbol{i}$ the relative eccentricity and inclination vectors and $[a,\ u,\ e_x,\ e_y\ i,\ \Omega]$ are the quasi non-singular orbital elements. In the definition of δa, the chief's semi-major axis is employed to a-dimensionalise the quantity, coherently with the rest of the relative state vector.
Under the hypothesis of small eccentricities and small relative distance (compared to the absolute orbit's radius), the relative motion model developed by D'Amico [7] expresses the evolution of the ROE under the effect of J_2 and differential drag as function of the initial condition and the mean argument of latitude u, taken as temporal variable:

$$\delta \boldsymbol{x}(u) = \begin{pmatrix} \delta a_0 \\ \delta \lambda_0 - \frac{21}{2}(\gamma \sin(2i_c)\delta i_{x,0} + \frac{1}{7}\delta a_0)(u - u_0) \\ \delta e_0 \cos(\phi_0 + \phi'(u - u_0)) \\ \delta e_0 \sin(\phi_0 + \phi'(u - u_0)) \\ \delta i_{x,0} \\ \delta i_{y,0} + 3\gamma \sin(i_c)^2 \delta i_{x,0}(u - u_0) \end{pmatrix} + \begin{pmatrix} -\frac{\Delta\beta}{n^2}\rho v^2 (u - u_0) \\ \frac{3\Delta\beta}{4n^2}\rho v^2 (u - u_0)^2 \\ 0 \\ 0 \\ 0 \\ 0 \end{pmatrix} \tag{3.6}$$

where

$$\gamma = \frac{J_2}{2}\left(\frac{R_E}{a}\right)^2 \frac{1}{\sqrt{1-e_c}^4}$$
$$\phi' = \frac{d\phi}{du} = \frac{3}{2}\gamma(5\cos(i_c)^2 - 1)$$
$$\Delta\beta = \beta_d - \beta_c.$$

In Equation 3.6 the polar notation has been introduced. That's an alternative way of representing the relative eccentricity and inclination vectors:

$$\delta\boldsymbol{e} = \begin{pmatrix}\delta e_x \\ \delta e_y\end{pmatrix} = \delta e \begin{pmatrix}\cos\phi \\ \sin\phi\end{pmatrix}, \qquad \delta\boldsymbol{i} = \begin{pmatrix}\delta i_x \\ \delta i_y\end{pmatrix} = \delta i \begin{pmatrix}\cos\theta \\ \sin\theta\end{pmatrix}, \tag{3.7}$$

where ϕ and θ are the *relative perigee* and the *relative ascending node*. The last contribute to include in the model is the one given by control actions. An impulsive manoeuvre $\Delta(\delta\boldsymbol{v})$ executed at the mean longitude u_M causes the following instantaneous variations $\Delta(\delta\boldsymbol{x})$ in the ROE state vector:

$$\begin{pmatrix}\Delta(\delta a) \\ \Delta(\delta\lambda) \\ \Delta(\delta e_x) \\ \Delta(\delta e_y) \\ \Delta(\delta i_x) \\ \Delta(\delta i_y)\end{pmatrix} \approx \begin{pmatrix} 2\Delta(\delta v_t)/na \\ -2\Delta(\delta v_r)/na - 3\Delta(\delta v_t)(u-u_M)/na \\ \Delta(\delta v_r)\sin u_M/na + 2\Delta(\delta v_t)\cos u_M/na \\ -\Delta(\delta v_r)\cos u_M/na + 2\Delta(\delta v_t)\sin u_M/na \\ \Delta(\delta v_n)\cos u_M/na \\ \Delta(\delta v_n)\sin u_M/na \end{pmatrix} \tag{3.8}$$

where u identifies the epoch of the relative orbital elements, and the term na is introduced to make the equations a-dimensional. Considering all the contributes presented above, the ROE can be then transformed into relative positions through the linear mapping:

$$\begin{aligned}\delta r_r/a_c &= \delta a - \delta e\cos(u-\phi) \\ \delta r_t/a_c &= \delta\lambda - \frac{3}{2}\delta a(u-u_0) + 2\delta e\sin(u-\phi) \\ \delta r_n/a_c &= \delta i\sin(u-\theta).\end{aligned} \tag{3.9}$$

Once the relative positions $\delta\boldsymbol{r}$ have been determined, it's possible to model the perpendicular baseline between the spacecrafts. Recalling that it is defined as the magnitude of the baseline component normal to the range direction (Figure 3.2), it can be computed in

the plane defined by ($\boldsymbol{o}_r$, $\boldsymbol{o}_n$) subtracting from $\delta\boldsymbol{r}$ its projection onto the range direction:

$$B_\perp = \left\| \begin{pmatrix} \delta r_n \\ \delta r_r \end{pmatrix} - \left[\begin{pmatrix} \delta r_n \\ \delta r_r \end{pmatrix} \cdot \begin{pmatrix} \cos\theta_L \\ -\sin\theta_L \end{pmatrix} \right] \begin{pmatrix} \cos\theta_L \\ -\sin\theta_L \end{pmatrix} \right\|. \tag{3.10}$$

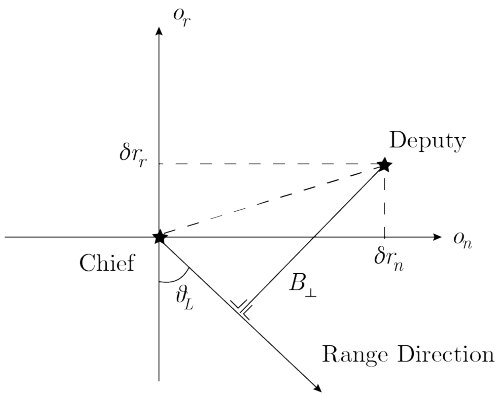

Figure 3.2: Perpendicular baseline. The plane orthogonal to the flight direction is the plane defined by $\boldsymbol{o}_r$ and $\boldsymbol{o}_n$, while the range direction is determined by the look angle θ_L.

3.3. Control Approach

The control plan developed in this work aims at achieving the scientific objectives while preserving the formation safety. To understand the motivations behind the formulated control logic it's important to recall the steps followed in its definition and the decisions taken, along with the rationale behind them.

3.3.1. Strategy Definition

To formalise the problem of control, it's first necessary to understand what are the essential features of the height of ambiguity (whose expression is recalled below for convenience) and how does these change during its evolution.

$$h_{2\pi} = \frac{\lambda R_1 \sin\theta_L}{2B_\perp}.$$

Looking at Figure 3.3 it's possible to observe the characteristic behaviour of the height of ambiguity over time, simulated from an arbitrary initial condition considering both J_2 and drag.

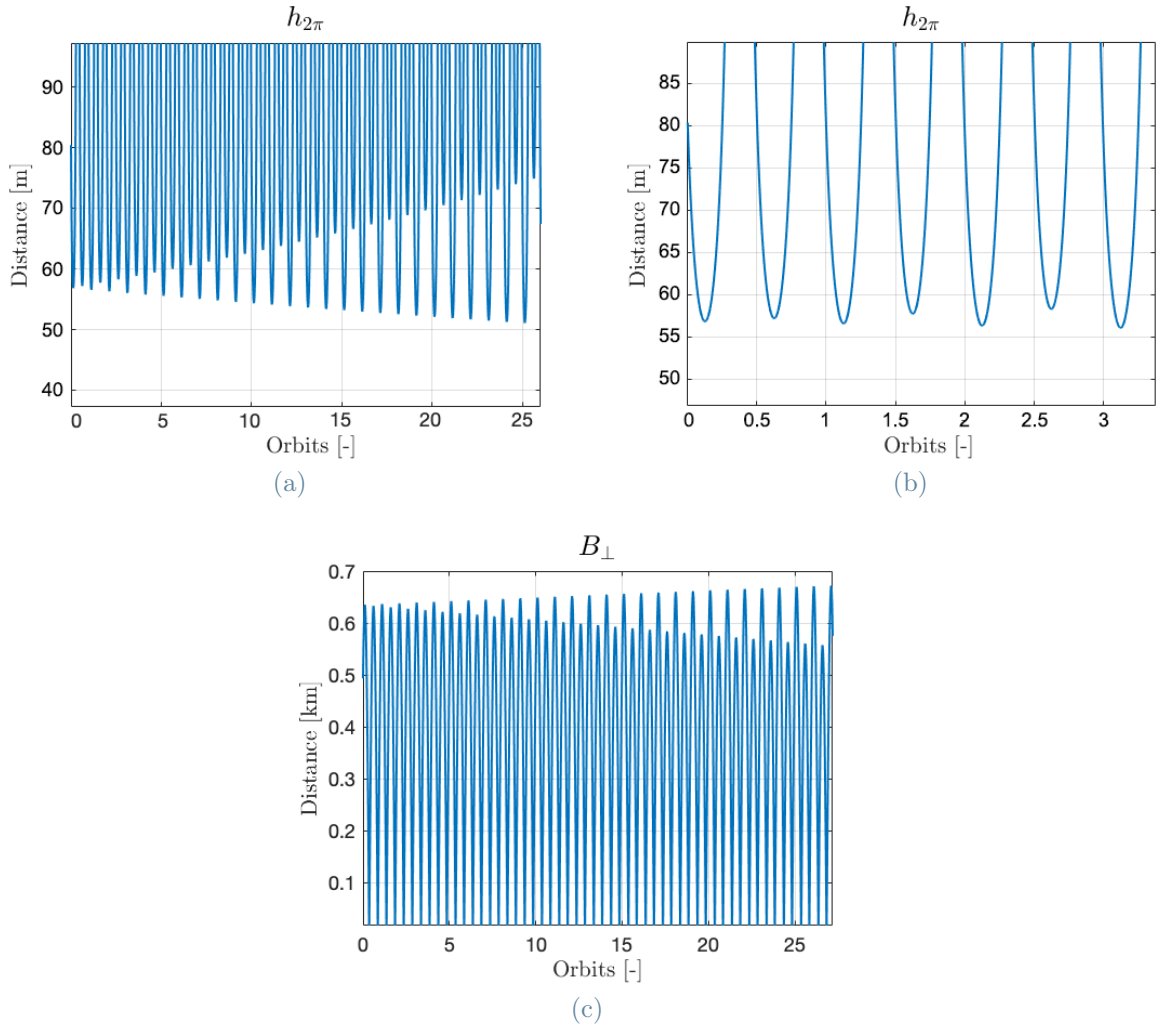

Figure 3.3: Height of ambiguity (a) under the influence of perturbations. In (b) a zoom of image (a), while in (c) is reported the corresponding evolution of the perpendicular baseline between the spacecrafts. The initial condition for this example is $a\delta\boldsymbol{x} = [0, 0, 140, 0, 120, 0]$ m. The radar parameters are $\lambda = 5$ cm, $\theta_L = \pi/4$ and $H = 490$ km.

The plot shows a periodic pattern with two lobes (minima) per each orbit separated by half an orbital period, diverging from each other because of perturbations. Specifically, by simulating under different conditions and scenarios it was verified that the main responsible for this is the drift introduced by drag on the relative semi-major axis. By maintaining a small bounded δa, the curve would show a stable behaviour with the lobes leveled at the same height. Assuming this ROE to be close to zero, by sizing correctly the function it would be possible to obtain two imaging windows per each orbit in which the height of ambiguity would remain inside the ± 2 m interval around its objective value. The size of the windows cannot be arbitrarily controlled, but depends on the harmonic behaviour of the relative positions δr_r and δr_n. Their location along the orbit instead is in principle always the same. However as observed in the figure, because of drag the drifting relative semi-major axis widens/shortens the windows size and shifts them downward/upward in the diagram.

To adequately carry out the scientific activity, the control system must be designed to counter-act the perturbations and maintain a stable height of ambiguity over time. In this way it would be possible to keep two fixed imaging windows for each orbit centered on two different great circles of latitude, symmetric with respect to the equator because the chief's orbit has zero argument of perigee. Exploiting the ground-track shift in every orbit it would be possible to image completely these two great circles in a few days or weeks, but in order to cover other latitudes it's necessary to shift the imaging windows from their location along the orbits. Through simulations it was verified that this can be achieved by changing the relative phase between relative eccentricity and inclination vectors. Therefore, alternated to the scientific activities, the control strategy is designed to foresee some maneuvering windows necessary to reconfigure the formation and shift the lobes on a different location on the orbit, correspondent to a different great circle of latitude.

Because of the different topologies that can be found on the Earth's surface, following the approach employed in other missions like TanDEM-X it was decided to analyse two case studies characterised by different objective values of the height ambiguity: 50 m and 150 m. These ranges can adapt to a lot of scenarios and landscapes on the Earth, from small elevated areas like countries, hills and vegetated areas to the highly elevated mountain regions and cities. Each case study will have its own windows size, and therefore a different number of configurations.

3.3.2. Control Problem Formulation

Once the strategy has been defined, the logic of the controller can be introduced. Since the objective of the control is to maintain the parameter of merit (height of ambiguity) inside a certain range ($h_{2\pi}^{obj} \pm 2$ m) during its evolution, a natural choice to implement it is to employ a Model Predictive Control (MPC) approach. Relying on a simplified model of the system, it can easily foresee how the formation would evolve subject to control actions and determine the best solution to actuate. However, even though the relative dynamics model is linearised, the definition of the height of ambiguity would involve dynamical constraints with strong non-linearities. As mentioned in the introduction, this work pursues the objective of enabling autonomous control with simplified on-board computations in order to lighten the overall work-load of the system, considering the large amount of data that need to be stored for the scientific activities. In this scenario, having to solve numerous non-linear optimisations would represent an important bottleneck for the control flow of the formation. Because of this, it is explored the possibility of softening the workload by exploiting convexification to transform a general non-linear optimisation problem into a convex optimal control problem, faster and easier to handle. Specifically, it is transformed into a second-order cone programming (SOCP) problem, a sub-class of convex optimisation problems efficently solvable with interior-point methods. The general SOCP problem is formulated as the minimisation of a linear cost function over a domain described by the intersection of an affine set and a second-order cone [21], like:

$$\min_{y} \quad \boldsymbol{c}^T \boldsymbol{y} \tag{3.11a}$$

$$\text{s.t.} \quad \|A_{sc}\boldsymbol{y} - \boldsymbol{b}_{sc}\| \leq \boldsymbol{d}_{sc}^T \boldsymbol{y} - \gamma_{sc} \tag{3.11b}$$

$$A_{eq}\boldsymbol{y} = \boldsymbol{b}_{eq} \tag{3.11c}$$

where the quantities with the subscript sc describe the second-order cone and A_{eq}, b_{eq} define the affine set.

Following the approach proposed by Lu and Liu [14], the dynamical constraints of the MPC approach can be convexified with an iterative procedure, by solving at each iteration two SOCP sub-problems. In the first step the i-th non-linear equality constraint $h_i(\boldsymbol{y}) = 0$ is linearised by expanding it at first order. The sub-problem to solve at each iteration

starting from the previous solution $\boldsymbol{y}^{[k]}$ is:

$$
\begin{aligned}
P_1: \quad & \min_{y} \quad \boldsymbol{c}^T \boldsymbol{y} && \text{(3.12a)}\\
& \text{s.t.} \quad h_i(\boldsymbol{y}^{[k]}) + \nabla h_i^T(\boldsymbol{y}^{[k]})(\boldsymbol{y} - \boldsymbol{y}^{[k]}) = 0\,, \quad i = 1, \ldots, n_{eq} && \text{(3.12b)}\\
& \qquad \|\boldsymbol{y} - \boldsymbol{y}^{[k]}\| \leq \rho_{trust} && \text{(3.12c)}
\end{aligned}
$$

where n_{eq} is the number of equality constraints and Equation 3.12c represents a trust-region constraint for a region of radius ρ_{trust}, formalised as a second-order cone, necessary for the method to enforce convergence. Once an optimal solution $\boldsymbol{y}^p$ is found for P_1 (note that this solution is dependent only on $\boldsymbol{y}^{[k]}$), it is employed in the computation of a corrective term of the second order (Equation 3.13) that guarantees superlinear convergence to the method and enhances robustness. The key point of the method selected is that this second-order correction doesn't require the computation of the Hessian matrix, and depends only on $\boldsymbol{y}^{[k]}$:

$$
h_i^{corr}(\boldsymbol{y}^{[k]}) = \frac{1}{2}(\boldsymbol{y}^p - \boldsymbol{y}^{[k]})^T(\nabla h_i(\boldsymbol{y}^p) - \nabla h_i(\boldsymbol{y}^{[k]})). \tag{3.13}
$$

Once computed, this correction term is introduced in the definition of the second sub-problem

$$
\begin{aligned}
P_2: \quad & \min_{y} \quad \boldsymbol{c}^T \boldsymbol{y}\\
& \text{s.t.} \quad h_i(\boldsymbol{y}^{[k]}) + \nabla h_i^T(\boldsymbol{y}^{[k]})(\boldsymbol{y} - \boldsymbol{y}^{[k]}) + h_i^{corr}(\boldsymbol{y}^{[k]}) = 0\,, \quad i = 1, \ldots, n_{eq}\\
& \qquad \|\boldsymbol{y} - \boldsymbol{y}^{[k]}\| \leq \rho_{trust}
\end{aligned}
$$

whose solution becomes the new $\boldsymbol{y}^{[k+1]}$. The Matlab function used to solve the SOCP sub-problems is *coneprog*, an algorithm that uses an interior-point method to solve the problem and introduces the possibility to add lower and upper boundaries to the optimisation variables. For each variable initial conditions, lower and upper boundaries have been empirically defined by trial and error. The boundaries are on purpose selected large, to leave to the algorithm the possibility of freely searching for an optimal result through the solutions space. Then, after the third iteration, the trust-region-like constraint is applied to help the algorithm focus in its research.
To control the iterative cycle, a stopping criteria has been defined, accounting for a tolerance on the error and the number of iterations. The cycles stop when both:

- the value of $h_i(\boldsymbol{y}^{[k+1]})$, for $i = 1, \ldots, n_{eq}$, is lower than 8e-8 for the last two consecutive iterations

- the number of iterations is greater than four, to ensure that the trust-region constraint has been introduced in the algorithm.

3.3.3. Formation Safety Requirements

For both the scenarios the same safety requirements are considered: the inter-satellite distance between the spacecraft shall be limited to a determined range. It means that both a lower and an upper boundary are imposed to their distance. The lower limit is introduced to preserve safely the formation, and avoid getting the spacecraft too close to each other considering possible errors or inaccuracies of the model. The upper boundary instead is imposed to remain inside the hypothesis of the model and consider it valid. Following the literature [10], the limits for the spacecrafts' distance are fixed to 150 m and 1000 m. In this sense, since by looking at the equations of motion the radial and out-of-plane positions have a pure oscillatory behaviour, as long as their amplitudes are limited the only contribute to keep controlled is the along-track position, that can drift in time.
Considering again a small controlled δa, the terms that introduce drift are due to drag, a non-zero δi_x and δv_t. Trying to prevent this drift, in principle the x-component of the relative eccentricity vector could be set to zero from the first configuration of each case study, and kept unchanged by maneuvering at locations with $u = \pi/2 + k\pi$ along the orbit. However, during the first simulations it was observed that even following this strategy in both the cases the along-track position had a negative drift, introduced by the positive δv_t term requested by the control system between each couple of manoeuvres. Furthermore as already mentioned to shift the location of the lobes along the orbits it is necessary to change the relative phase between $\delta \boldsymbol{e}$ and $\delta \boldsymbol{i}$. Different simulations proved that the best solution found by the control algorithm is to introduce a δi_x different from zero. Thus, the choice of introducing a zero δi_x would be applicable only for the first configurations. The strategy adopted to counteract the drift caused by non-zero δi_x, and maintain a bounded δr_t, is to apply an additional impulse in the along-track direction exploiting the drift introduced by the δv_t term to maintain a bounded δr_t. The control strategy selected implements a trigger logic for the additional impulse, and can be differentiated in two phases:

- a **coasting phase**, in which the average of δr_t is left free to drift until the oscillations reach the lower trigger value
- a **recovery phase** in which after each main manoeuvre the additional impulse is given to raise the average of δr_t, until the upper trigger is reached.

For each case study, the trigger values are set equal to plus or minus the minimum between δr_t^{crit} and 800 m.
The extra manoeuvre applied during the recovery phase might have a negative impact on the scientific activity, affecting the height of ambiguity lobes. To counteract this eventuality, after each reconfiguration the lobes will be designed to maintain a certain overlap margin with the lobes of the previous configuration, sufficiently small to keep the number of total configurations as low as possible.

4 | Control Algorithms

The algorithms developed for the formation design and control are all based on the convexification method illustrated in the previous chapter: each of them minimises a cost function that involves the specific problem parameters of the case. To follow the model predictive approach each optimisation has to be carried out subject to relative dynamics constraints and boundaries for the optimisation variables.
There are four principal algorithms to describe:

- *roe_initial*: to compute optimal initial conditions.
- *correct_h*: to correct the height ambiguity deviation of the next lobe.
- *shift_lat*: to shift the next lobe along the orbit.
- *da_to_di*: to compensate the δa term introduced during reconfiguration with an out-of-plane manoeuvre.

4.1. Algorithm 1: *roe_initial*

The first algorithm is run just once at the beginning of each simulation, to compute the optimal initial condition of the case study under exam. It's objective is to search for a set of ROE $\delta\boldsymbol{x}_0$ such that propagated over half an orbit determines an imaging window with maximised duration. Given this objective, it's necessary to understand how to impose the dynamic constraints to the problem, in order to search for the optimal solution.
Looking at the typical behaviour of the height ambiguity curve (Figure 4.1), it's possible to identify three points of interest:

- u_{in}: the instant (or mean argument of latitude) at which the curve gets inside the ± 2 m range around the objective value $h_{2\pi}^{obj}$.
- u_{out}: the instant at which the curve exits this range.
- u_{mid}: the instant in the middle of u_{in} and u_{out}, where the lobe reaches its minimum.

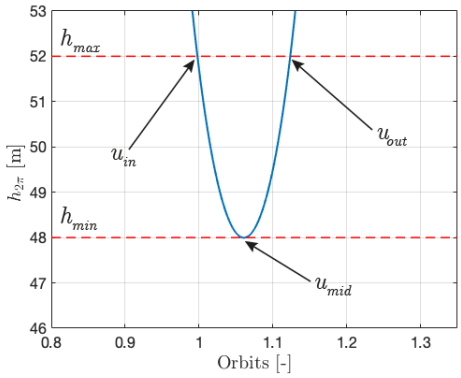

Figure 4.1: The three points of interest u_{in}, u_{mid} and u_{out} in the height ambiguity curve.

The idea adopted is to shape the curve as desired by imposing the location of these three points along the orbit, with u_{mid} close to the lower boundary: the objective of the optimisation can be hence translated into maximising the distance between u_{in} and u_{out}.

Along with these temporal coordinates, the optimisation shall also define the vector of initial ROE to be propagated. Following the considerations adopted in the previous sections, the structure of the ROE vector to be optimised is:

$$\delta \boldsymbol{x} = \begin{pmatrix} 0 \\ - \\ \delta e \\ \phi \\ \delta i_x \\ \delta i_y \end{pmatrix}$$

where the mean longitude (second entry) is not considered because it doesn't take part in the definition of the height ambiguity, and the polar notation for the relative eccentricity vector is adopted just for convenience. Applying the well-known concept of relative eccentricity-inclination separation e-i separation [16], the boundaries of the related four ROE are set to design a passively safe formation with almost parallel $\delta \boldsymbol{e}$ and $\delta \boldsymbol{i}$. This requirement shall be enforced at least for the first configurations, expected to be maintained for longer because designed to map the great circle at lower latitudes. Furthermore, following the considerations of the previous chapter related to the formation safety, it is decided to select only initial conditions that maintain an inter-satellite distance larger than 150 m at least for five orbits in case no control is applied.

The seven variables introduced above define the optimisation variables of the problem. However, before proceeding it is necessary to make a consideration. Since the optimisation

works to minimise linear a cost function of the type

$$\min_{\boldsymbol{y}} \boldsymbol{c}^T \boldsymbol{y}$$

to maximise the distance between u_{in} and u_{out} it's not possible to employ directly the latter in the equations, otherwise it would be minimised too. Instead, it's possible to introduce a new variable $\tilde{u}_{out}$, equal to the reciprocal of u_{out}, to be minimised.
To sum up, the optimisation variables of the problem are:

$$\boldsymbol{y} = [\delta e, \phi, \delta i_x, \delta i_y, u_{in}, \tilde{u}_{out}] = \left[\delta \boldsymbol{x}^{opt}, \delta \boldsymbol{u}^{opt}\right]$$

where $\delta \boldsymbol{x}^{opt}$ and $\delta \boldsymbol{u}^{opt}$ are vectors of optimisation variables. The optimisation has to be carried out subject to the dynamical constraints of the relative motion model adopted. As described in the previous section, for the problem of control the equations of motion must be linearised and imposed as linear constraints in the optimisation. But rather then imposing directly the constraints through the height ambiguity, it can be useful to work with the perpendicular baseline instead, because it simplifies a lot the definitions of the equations and the Jacobian in the convexification. To perform the optimisation, the set up and solution of the problem has been done using the *Symbolic Math Toolbox* of Matlab. Once the variables have been declared, the relative positions of the spacecrafts and the perpendicular baseline can be written as function of $\delta \boldsymbol{x}^{opt}$ and the generic temporal variable u, recalling Equations 3.9 and 3.10:

$$\begin{cases} \delta r_r = \delta r_r(\delta \boldsymbol{x}^{opt}, u) \\ \delta r_n = \delta r_n(\delta \boldsymbol{x}^{opt}, u) \\ B_\perp = B_\perp(\delta \boldsymbol{x}^{opt}, u) \end{cases} \tag{4.1}$$

The passage of the curve through the three points desired can then be enforced through the non-linear equation:

$$\boldsymbol{h}(\boldsymbol{y}) = \begin{bmatrix} B_\perp(\delta \boldsymbol{x}^{opt}, u_{in}) \; - \; B_\perp^{min} - s_{in} \\ B_\perp(\delta \boldsymbol{x}^{opt}, u_{mid}) - B_\perp^{max} + s_{mid} \\ B_\perp(\delta \boldsymbol{x}^{opt}, 1/\tilde{u}_{out}) - B_\perp^{min} - s_{out} \end{bmatrix} = \boldsymbol{0} \tag{4.2}$$

where $B_\perp^{min/max}$ represents the minimum/maximum values of the perpendicular baseline, associated to the maximum/minimum values of the height ambiguity in the range $h_{2\pi}^{obj} \pm 2$ m, and s_{in}, s_{mid} and s_{out} are dummy variables introduced to reduce the strength of the equivalence constraints. The sign of s_{mid} in the second equation is different in order to

search for a solution with the peak smaller than $B_{\perp}^{max}$, to maintain the height ambiguity above its lower limit. Therefore, the extended a-dimensional vector of optimisation variables is:

$$\boldsymbol{y} = [\delta e, \phi, \delta i_x, \delta i_y, u_{in}, \tilde{u}_{out}, s_{in}, s_{mid}, s_{out}] \,.$$

After an initial condition, a lower boundary and an upper boundary have been set for each variable, and the trust-region SOC constraint has been declared, the optimisation can start searching for a solution as described in the previous section until either both the stopping criteria (minimum number of iterations and norm of $\boldsymbol{h}(\boldsymbol{y})$) are satisfied, or the number of iterations surpasses 20. In the latter case, the simulation gets interrupted. The presentation of this section is concluded with the logic reported in Algorithm 4.1, that resumes the structure of all the algorithms presented in this chapter, and Table 4.1 that reports the numerical values of the optimisation parameters of algorithm *roe_initial* for the first case study. The values of the second case study are pretty similar to those of the table except for $\tilde{u}_{out}$, the only variable with substantially different boundaries ($1/30°$, $1/20°$) and initial condition ($1/25°$).

Algorithm 4.1 General Structure

```
Parameters Input
Symbolic Variables Declaration
Weights, boundaries and IC definition
Non-linear constraints definition
Jacobian computation
iter = 1, check1 = 0, check2 = 0
%Iterative process start
while check2 == 0 and iter < 3 do
    if iter > 20 then
        break
    end if
    if iter > 2 then
        Activate trust-region constraint
    end if
    %SOCP Problems setup and solution
    First SOCP Problem optimisation
    Second-order corrective term computation
    Second SOCP Problem optimisation
    %Update for stop criteria
    if check1 == 1 and ‖h(y)‖ < 8e-8 then
        check2 = 1
    else
        check1 = 0
    end if
    if ‖h(y)‖ < 8e-8 then
        check1 = 1
    end if
    iter = iter+1
end while
```

4.2. Algorithm 2: *correct_h*

The task of the second algorithm is to find suitable control actions to counteract the lobes drift of the height ambiguity plot. This algorithm has a similar structure with respect to the previous, however with two important differences. The first difference concerns

Variable	LB	UB	IC	Weight	Solution
δe	0	6e-5	4e-5	0	3.07e-5
ϕ	200°	360°	220°	0	213°
δi_x	-2e-5	2e-5	0	0	-7.65e-6
δi_y	-5e-5	5e-5	-6e-5	0	-5e-6
u_{in}	0	2°	0°	1	∼0°
$\tilde{u}_{out}$	1/46°	1/34°	1/34°	1	1/43.5°
s_{in}	0	1e-5	1e-8	100	4e-10
s_{mid}	0	1e-5	1e-8	100	4.6e-10
s_{out}	0	1e-5	1e-8	100	1.6e-7
ρ_{trust} = 1e-3					

Table 4.1: Numerical values of the optimisation parameters for algorithm *roe_ initial*, first case study ($h_{2\pi}^{obj}$ = 50 m). The columns identify the lower boundaries (LB), the upper boundaries (UB), the initial conditions (IC) and the weights of $\boldsymbol{c}$, while the last column reports the solution found from the optimisation. For convenience the angular quantities are reported in degrees, while the lengths are a-dimensionalised by a_c = 6891 km.

the treatment of the u_{out}. Since for the mission purposes it's important to maintain a constant size for the imaging windows (i.e. the time spent inside the ±2 m range around $h_{2\pi}^{obj}$), shall focus on this objective rather than trying to maximise the window size as in the previous algorithm. That's an important difference, because as it was observed it's possible,by introducing a non-zero relative semi-major axis, to enlarge the size of the windows. However, a too large value of the semi-major axis leads to instabilities in the height ambiguity plot and large distancing between the spacecrafts, both conditions that shall be avoided as possible. This is why at each run the control problem is setup to keep a size for the windows as close as possible to the one found with the algorithm *roe_ initial*, defined "condition 0" (u_{in0}, u_{out0}). This is done by introducing the variable u_{out} to replace its reciprocal, and fixing the boundaries for $u_{in/out}$ at the k-th run in a short interval of ±1° around $u_{in0/out0}+k\pi$ leaving the algorithm a certain degree of freedom in the research. Specifically, since the vector $\boldsymbol{y}$ is expected to have components in the order of 10^{-5} or even smaller, to avoid potential numerical problem at high mean arguments of latitude the problem is optimised with respect to two new variables u'_{in} and u'_{out} such that at the k-th run:

$$\begin{aligned} u_{in} &= u_{in0} + k\pi + u'_{in} \\ u_{out} &= u_{out0} + k\pi + u'_{out}. \end{aligned} \tag{4.3}$$

This ensures an almost constant level of flexibility to the algorithm in the research for all the values of u necessary for the simulations. As said above, since the objective is not to

maximise the windows size, the weights assigned to u'_{in} and u'_{out} in the optimisation are zero.
The second important difference is that the problem now is focused on the impulses, rather then the ROE. The new vector of optimisation variables is defined as:

$$\boldsymbol{y} = [\Delta(\delta v_r), \Delta(\delta v_t), \Delta(\delta v_n), u'_{in}, u'_{out}]$$

At each run, the state is propagated from the last u_{in} instant up to the new manoeuvre instant u_M. Recalling Equation 3.8 it's possible to define the relative state vector $\delta\boldsymbol{x}^{man}$ at the epoch u after the manoeuvre as function of the impulse given, the manoeuvre instant and the temporal variable u. This state vector is then employed in the definition of the dynamical constraints as explained above.

$$\boldsymbol{h}(\boldsymbol{y}) = \begin{bmatrix} B_\perp(\delta\boldsymbol{x}^{man}, u_{in}(u'_{in})) \; - \; B_\perp^{min} - s_{in} \\ B_\perp(\delta\boldsymbol{x}^{man}, u_{mid}(u'_{in}, u'_{out})) - B_\perp^{max} + s_{mid} \\ B_\perp(\delta\boldsymbol{x}^{man}, u_{out}(u'_{out})) - B_\perp^{min} - s_{out} \end{bmatrix} = \mathbf{0} \tag{4.4}$$

Then, the algorithm addresses the problem of total total $\Delta(\delta v)$ minimisation. Since the impulses can be either positive or negative, the variables vector is extended to include three other dummy variables η. These variables are employed in the definition of three additional SOC constraints of the type:

$$\|\Delta(\delta v)_i\| \leq \eta_i. \tag{4.5}$$

In this way, it's possible to minimise the $\Delta(\delta v)$ by setting non-zero weights for the variables η. The extended vector of optimisation variable then results to be:

$$\boldsymbol{y} = [\Delta(\delta v_r), \Delta(\delta v_t), \Delta(\delta v_n), u'_{in}, u'_{out}, s_{in}, s_{mid}, s_{out}, \eta_r, \eta_t, \eta_n]$$

The numerical values of the optimisation parameters of this algorithm for the case study $h_{2\pi}^{obj} = 50m$ are reported in Table 4.2.

4.3. Algorithm 3: *shift_lat*

The third algorithm concerns the first (and bigger) part of the reconfiguration phase. It's task is to sequentially shift the lobes of the height ambiguity curve backwards in the orbits. The backward shift proved to be more stable and effective with respect to the forward one, with the algorithms implemented.

Variable	LB	UB	IC	Weight
$\Delta(\delta v_r)$	-0.8e-4	0.8e-4	1e-7	0
$\Delta(\delta v_t)$	-0.8e-4	0.8e-4	1e-7	0
$\Delta(\delta v_n)$	-0.8e-4	0.8e-4	1e-7	0
u'_{in}	-1°	1°	0°	0
u'_{out}	-1°	1°	0°	0
s_{in}	0	1e-8	1e-9	100
s_{mid}	0	1e-8	1e-9	100
s_{out}	0	1e-8	1e-9	100
η_{in}	0	1e-4	1e-6	1
η_{mid}	0	1e-4	1e-6	1
η_{out}	0	1e-4	1e-6	1
$\rho_{trust} = 3\text{e-}3$				

Table 4.2: Numerical values of the optimisation parameters for algorithm *correct_h*. The $\Delta(\delta v)$ components are a-dimensionalised by $a_c n_c = 7.605$ km/s. These values refer to the case study $h_{2\pi}^{obj} = 50$ m, but are quite representative even for the values of the other case study.

The objective is achieved by a series of manoeuvres that shift the curve by a fraction of the imaging window, until the desired number of manoeuvres is reached. Shifting the whole lobe with a single manoeuvre would mean first of all to have much greater costs in terms of $\Delta(\delta v)$, and secondly the algorithm could have strong issues in the research of the solution for a problem too much constrained.
The algorithm was developed basing on the same approach and the same structure of the previous (*correct_h*), but with two substantial differences. The first difference regards the boundaries definition of $u_{in/out}$. Since it's necessary to shift the lobes, for each of the sequential manoeuvres these boundaries differ from the previous values $u_{in0/out0} + k\pi$ by a factor

$$-k\delta u_{shift} = -k\left(u_{out0} - u_{in0}\right)\frac{\Delta_{over}}{N_M} \tag{4.6}$$

where Δ_{over} is the overlay margin of the lobes (expressed as a percentage), k identifies the k-th maneuver and and N_M is the total number of manoeuvres desired.
The second difference regards the manoeuvre instant, that in this case is not fixed but considered as an optimisation variable. That's because, recalling the definition of the perpendicular baseline in Equation 3.10, to introduce this shift it's necessary to properly change the relative phase between the relative eccentricity and inclination vectors, and keeping the manoeuvres fixed at the location $u = \pi/2 + k\pi$ strongly limits the algorithm capabilities of research since a lot of contributions in Equation 3.8 cancel out. Following

the approach presented in the previous section to prevent numerical instabilities at high mean arguments of latitude, at each k run this new optimisation variable is defined as:

$$u_M = u_{in0} + (k-1)\pi - (k-1)\delta u_{shift} + u'_M.$$

that's basically the definition of u_{in} in the previous lobe without considering the $\pm 1°$ range. The variable u'_M is left free to vary between δu_{shift} and $\pi - \delta u_{shift}$, and the associated weight is zero. The greatest disadvantage of this choice is the introduction of another drift term in the along-track position due to δi_x, that must properly controlled to avoid too large distancing of the spacecrafts.
The optimisation variables vector $\boldsymbol{y}$ for this algorithm hence comprises:

$$\boldsymbol{y} = [\Delta(\delta \boldsymbol{v})_{opt}, u'_M, u'_{in}, u'_{out}, \boldsymbol{s}_{opt}, \boldsymbol{\eta}_{opt}]$$

with the compact notation introduced to represent all the variables described in the previous sections. Table 4.3, reports the numerical values of the optimisation parameters for the algorithm under exam.

Variable	LB	UB	IC	Weight
$\Delta(\delta v_r)$	-1.3e-4	1.3e-4	1e-6	0
$\Delta(\delta v_t)$	-1.3e-4	1.3e-4	1e-6	0
$\Delta(\delta v_n)$	-1.3e-4	1.3e-4	1e-6	0
u'_M	δu_{shift}	π - δu_{shift}	$2\delta u_{shift}$	0
u'_{in}	-1°	1°	0°	0
u'_{out}	-1°	1°	0°	0
s_{in}	0	1e-5	1e-9	100
s_{mid}	0	1e-5	1e-9	100
s_{out}	0	1e-5	1e-9	100
η_r	0	2e-4	1e-6	1
η_t	0	2e-4	1e-6	1
η_n	0	2e-4	1e-6	1
ρ_{trust} = 1e-2				

Table 4.3: Numerical values of the optimisation parameters for algorithm *shift_lat*. The $\Delta(\delta v)$ components are a-dimensionalised by $a_c n_c = 7.605$ km/s

4.4. Algorithm 4: *da_to_di*

The last algorithm regards the last manoeuvre of the reconfiguration phase. It was observed that the solutions found with algorithm three generally introduce large variations

in the relative semi-major axis, a potential danger for the successive science phase. The objective of the algorithm is to cancel this effect by introducing a change in the other ROE. In particular, it was observed that the most effective choice in this sense is to introduce a change in the relative inclination vector with an out-of-plane manoeuvre. To avoid other undesired variations of the δi_x component, apart from those already introduced with the reconfiguration, the maneuver is executed at an instant $u_M = \pi/2 + k\pi$, thus affecting only the y-component of the relative inclination vector. Therefore, only impulses in the tangential and out-of-plane directions are considered.
The first component, $\Delta(\delta v_t)$, is assigned. Since after half an orbit the science phase is expected to restart, this impulse is computed to leave a sufficiently small relative semi-major axis, such that at the next maneuver instant (after π radiants of mean longitude) it will become zero because of drag.

$$\begin{cases} \Delta(\delta a)_{des} = -\delta a_M + \Delta B \rho v_d^2 / n_d^2 \pi \\ \Delta(\delta v_t) = \Delta(\delta a)_{des}/2 \end{cases} \tag{4.7}$$

where δa_M is the value of the relative semi-major axis at the manoeuvre instant and the second term represents the variation introduced by drag after π radiants. The out-of-plane component $\Delta(\delta v_n)$ instead is computed through an optimisation, to satisfy the dynamical constraints as in the previous algorithms. The vector of optimisation variables in this case is reduced to:

$$\boldsymbol{y} = [\Delta(\delta v_n), u'_{in}, u'_{out}, s_{in}, s_{mid}, s_{out}, \eta_n] \,,$$

and numerical values for the relative optimisation parameters are reported in Table 4.4.

Variable	LB	UB	IC	Weight
$\Delta(\delta v_n)$	-1e-4	1e-4	1e-6	0
u'_{in}	-1°	1°	0°	0
u'_{out}	-1°	1°	0°	0
s_{in}	0	1e-5	1e-9	100
s_{mid}	0	1e-5	1e-9	100
s_{out}	0	1e-5	1e-9	100
η_{out}	0	1e-4	1e-7	1
ρ_{trust} = 1e-2				

Table 4.4: Numerical values of the optimisation parameters for algorithm *da_ to_ di*. The $\Delta(\delta v_n)$ component is a-dimensionalised by $a_c n_c = 7.605$ km/s

5 | Simulation

To test the designed control strategy, simulations have been run using Matlab and Simulink. The Matlab functions were implemented to simulate the relative dynamics of the spacecrafts and the control system operations. The Simulink model (Figure 5.1) instead was implemented to simulate the absolute dynamics of the Chief. For each orbit, estimations of the average spacecraft's altitude and atmosphere's density are obtained propagating under the effect of drag and J_2. Because of the short inter-satellite distances hypothesis, it is assumed that the same values of hold true for the Deputy, and these piece-wise constant average altitudes and densities are employed for the computation of the relative drag and the height ambiguity. The time-step for this simulation was set to 10 seconds. Figure 5.2 represents the averaged variations of altitude and density predicted with the model.

To verify the validity of the algorithms, the simulations shall prove both that the drift of the lobes can be correctly compensated over long periods and that the reconfiguration manoeuvres are effective in shifting the latitudes range of the curves. To this aim, two different simulations have been run for both the case studies.
The first is an extended one-month simulation of scientific activity in which relative orbital control is applied to correct the lobes drift of $h_{2\pi}$, with the aim of showing the results and the long term effectiveness of the algorithm *correct_h*. To give a better insight, for each case study this simulation runs over two different configurations, with a programmed reconfiguration in the middle. A complete reconfiguration with the scheme proposed can be obtained in three orbits for both the case studies. The resulting simulation layout foresees:

- 15 days (ca. 225 orbits) of imaging with the first configuration.
- Reconfiguration manoeuvres (three orbits).
- Other 15 days of scientific activity with the second configuration.

The second simulation instead aims at proving the efficacy of algorithms *shift_lat* and *da_to_di*. It verifies that, for each case study, the reconfiguration manoeuvres are effective in shifting the range of latitudes corresponding to the height ambiguity interval of interest.

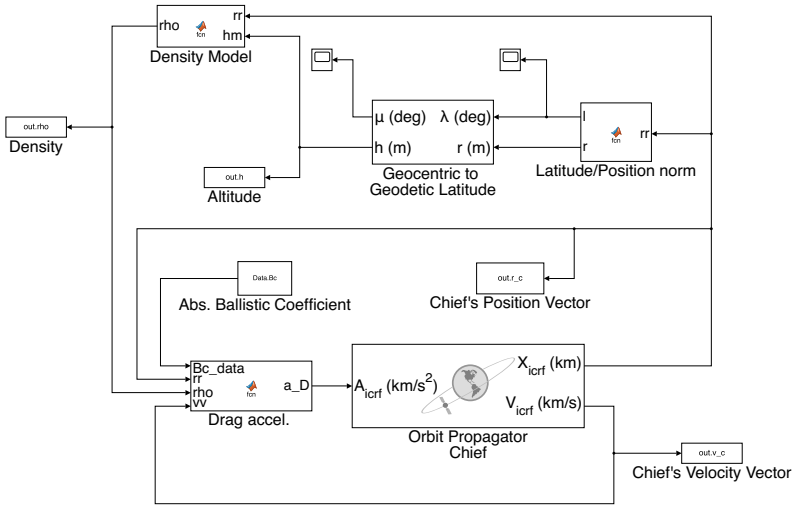

Figure 5.1: Simulink model of the Chief's orbital dynamics. The orbit altitude is computed by means of the *Geocentric to Geodetic Latitude* block, starting from the geocentric latitude and the norm of the position vector. With this, it's possible to estimate the atmosphere's density using the exponential density model described in Section 3.2. For each orbit, the altitude and the density will be averaged over one orbital period and taken as constants.

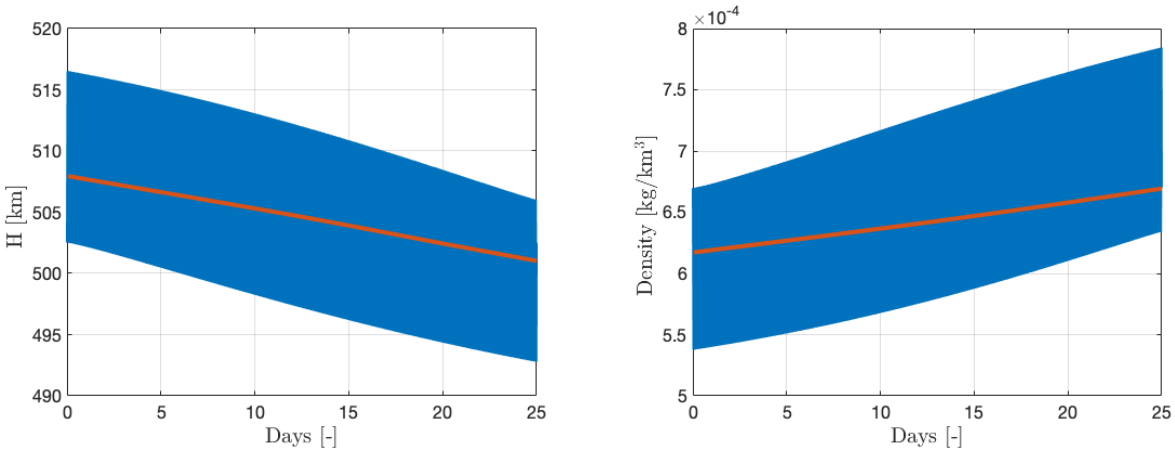

(a) (b)

Figure 5.2: Results of the Simulink model of the chief for the altitude (a) and density (b) variations, over 25 days simulation, subject to drag and J_2. The red lines identify the average values per orbit.

It is based on the following structure:

- 1 day (ca. 15 orbits) of imaging
- Reconfiguration manoeuvres (three orbits)

repeated as many times as necessary to cover all the latitudes possible, that means five times for the case $h_{2\pi}^{obj} = 50$ m and eight times for the case $h_{2\pi}^{obj} = 150$ m. Plus, the one day scientific activity permits, even if for short terms, to verify the validity of algorithm 1 also for the configurations not considered in the first simulation.
Both the simulations discretize the orbits with a 0.02 degrees step, and the differential drag coefficient is set to 0.01 m^2/kg.
The flowcharts of the simulations are reported below. Figure 5.3 represents the flowchart of the scientific activity simulation. After initialisation and initial condition computation with *roe_initial*, a cycle begins over the index N (number of orbits) until it reaches its maximum. For each orbit, firstly the values of average altitude, average density and the limits of $B_\perp$ are updated. Then, the control *correct_h* searches for an optimal impulse to correct the deviation of the next lobe, and if it is necessary to control the drift of the along-track position, also this manoeuvre is computed. The produced outputs are fed to the relative dynamics simulator, necessary to update the state and predict the behaviour of the $h_{2\pi}$ curve after the manoeuvres. This scheme is iterated twice per orbit (over the index n), to correct both the lobes.
Figure 5.4 instead represents the flowchart of the reconfiguration. The iterative structure

is similar to that of the previous chart, cycling over the number of orbits (index N) and the lobes (index n). However in this case there's no control on the along-track position, and the manoeuvres executed have the purpose of shifting the lobes in the height ambiguity curve. The last manoeuvre then is used to cancel the δa term introduced with the shifts compensating it with a variation of the relative inclination vector (da_to_di).
The rationale followed in the presentation of the results for each case study, and each simulation, will be the following: firstly the performances of the control algorithms will be discussed looking at the plots of the height ambiguity curve. To get a deeper insight on the actions exerted, then, the analysis will focus on the evolution of the ROE under the effects of the control. Finally, the results in terms of impulses required and algorithms performances will be presented to conclude the discussion.

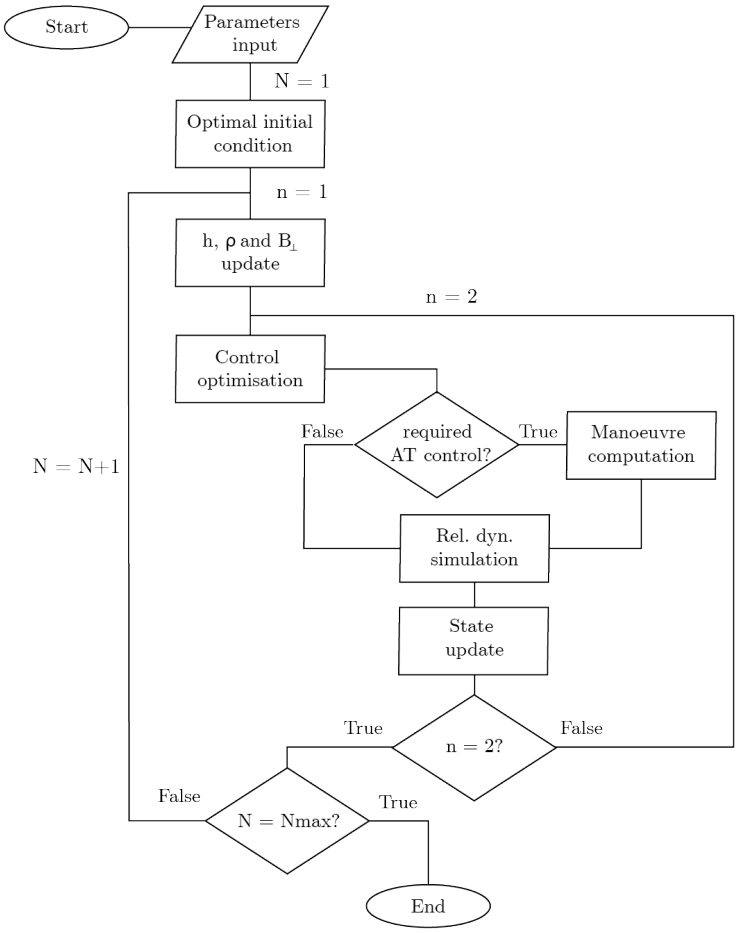

Figure 5.3: Flowchart of the scientific activity simulation: index N identifies the number of the orbit, while index n represents the number of the lobe (twice per orbit) to correct. The number N_{max} is 15 for the reduced simulation and 225 for the extended one.

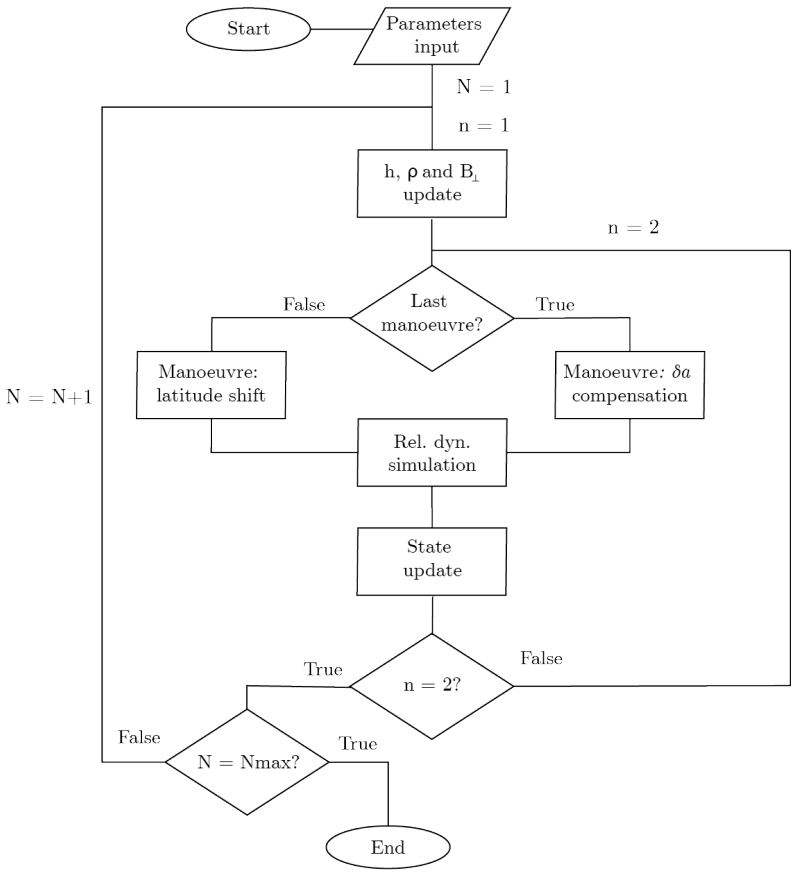

Figure 5.4: Flowchart of the reconfiguration: again index N identifies the number of the orbit while index n represents the number of the lobe (twice per orbit) to shift.

5.1. Case study $h_{2\pi}^{obj} = 50$ m

This first case considered has a large perpendicular baseline, comprised between 227 and 246 m for the ambiguity interval of interest. The optimal solution found with the optimisation algorithm *roe_initial* as initial condition is reported in Table 5.2. Figure 5.5 instead represents the behaviour of the height of ambiguity and the inter-satellites distance over time starting from this initial condition, in case no control is applied to the spacecrafts.

$a\delta a$	$a\delta\lambda$	$a\delta e_x$	$a\delta e_y$	$a\delta i_x$	$a\delta i_y$
0 m	32.5 m	-3.7 m	-177.3 m	24.5 m	-248.4 m

Table 5.1: Optimal initial condition found for the case $h_{2\pi}^{obj} = 50$ m.

Look Angle	Swath	Duty Cycle	$B_{\perp}^{crit}$	δr_t^{crit}	δr_t trigger
25°	93.3 km	15'10"	5.15 km	33 km	±800 m m

Table 5.2: Optimal initial condition found for the case $h_{2\pi}^{obj} = 50$ m.

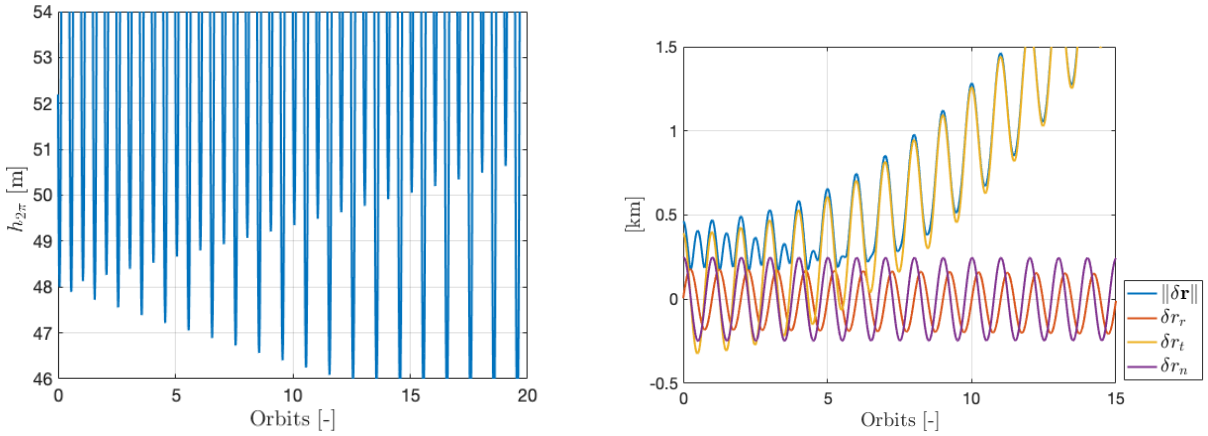

(a) (b)

Figure 5.5: Evolution over time of the height ambiguity (a) and spacecraft's distance together with the components of $\delta\boldsymbol{r}$ (b) for the case $h_{2\pi}^{obj} = 50$ m in conditions of free motion.

It can be observed that the height ambiguity valleys slowly drift from the 48 m objective, causing a difference of roughly ±1 m after seven orbits (i.e. 11 hours). During the same period of time the spacecrafts get to find themselves at a distance of about 1 km, mostly because of the along-track drift introduced by drag, as it can be recognised a quadratic behaviour in δr_t. Since the principal cause of the valleys drift is the relative semi-major

axis decay, this slow deviation observable suggests that the case under examination has, in this sense, a light sensitivity on drag.

5.1.1. Extended Simulation

The first objective of the control system is to correct the valleys deviation of the curve in Figure 5.5.a, to enable a continuous scientific activity over the latitudes range of interest. The results for the first configuration are shown in Figure 5.6, together with a description of the principal features. The plot shows an initial transitory (ca. three orbits) in the first

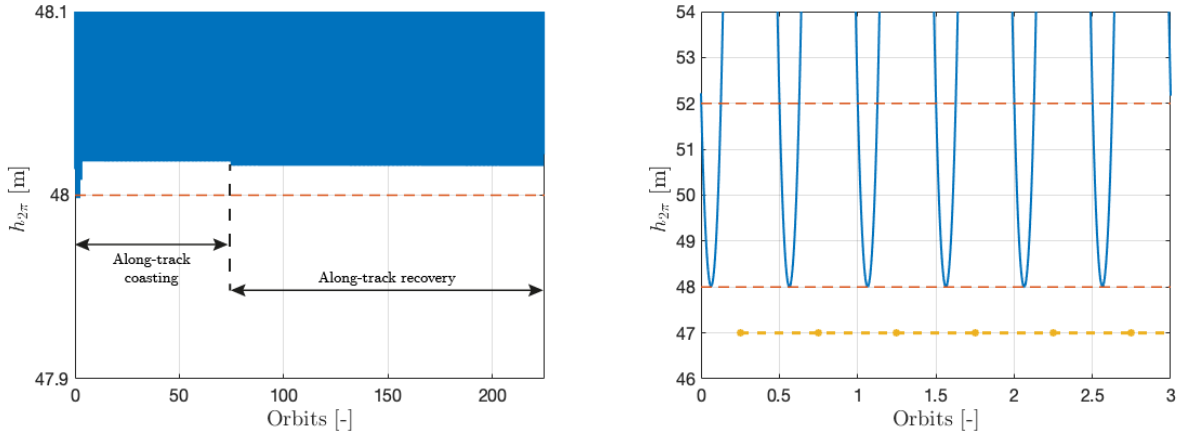

(a) (b)

Figure 5.6: A zoom close to the lower limit of 48 m (a) and a detail (b) of the resulting height ambiguity plot after the application of control. The red dotted lines identify the boundaries of the ±2 m range. On the bottom of image (b), the dots on the yellow line represent the manoeuvres location along the orbits.

orbits that drives the curve below the 48 m limit. Detecting this overpass, the control algorithms try to correct this behaviour by raising the value of h_{min} in the optimisation by 1 cm. This can be better noted in Figure 5.7. For the entire along-track coasting phase the curve remains above the lower limit of 48 m. It happens that on the fifth day (orbit 78) the along-track recovery phase begins, because the spacecrafts get to find at a distance greater, in modulus, than 800 m. The additional impulses given 30 seconds after the principal manoeuvres lowers a bit the curve, that however remains above the lower limit until the end of the simulation. The overall result is that for this simulation the condition $h_{2\pi} \geq 48$ m is verified more than 99.999% of the time.
For what concerns the upper boundary of 52 m instead, what's important to verify is that the height ambiguity range of interest for imaging is located at the same angular position along each orbit, in order to effectively cover one great circle of latitude with

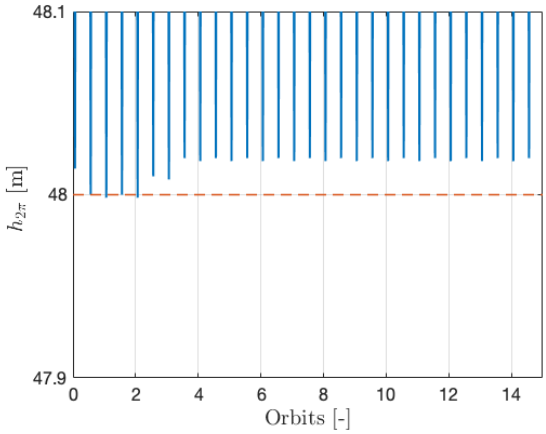

Figure 5.7: First configuration of the first case study. The plots point out the transitory in the initial three orbits of the simulation.

each configuration. Figure 5.8 represents how the angular position of the initial and final instants of imaging u_{in} and u_{out} vary along the orbits. It reports the behaviour of the relative shift u^{err}, defined as the difference between the real measured initial/final instants and the ideal case in which each interval is separated by half an orbit, normalised by the length of the first interval. Mathematically it means:

$$\begin{cases} u^{id}_{in/out} = u_{in0/out0} + \pi\,[0:1:2\times 15\times 15-1] \\ u^{err}_{in/out} = \dfrac{(u^{id}_{in/out} - u^{meas}_{in/out})}{(u_{out0} - u_{in0})} \times 100 \end{cases} \tag{5.1}$$

where the notation $\pi\,[0:1:2\times 15\times 15-1]$ identifies a vector of 450 elements (2 lobes times 15 orbits times 15 days of simulation) from 0 to 449 with span 1, multiplied by π, and represents a straight line with angular coefficient π.

The plots shows some interesting results.
The first thing to note is the three orbits transitory that introduces a non-zero relative error, slightly forwarding the instants u_{in} and backing u_{out}. The latter then, under the effect of control actions remains fixed while the position of u_{in} shows short oscillations of about 0.05%, or 0.02°. It is noted that, as mentioned at the beginning of this chapter, that is exactly the size of the discretised temporal variable u of the problem. Thus, these oscillations represent a discretisation error of the problem, and their real value is comprised between the two extremes. During the along-track recovery, because of the additional manoeuvres the curve gets slightly lowered, and this discretisation error is overcome. From these considerations it's possible to understand that even the linear behaviour observed

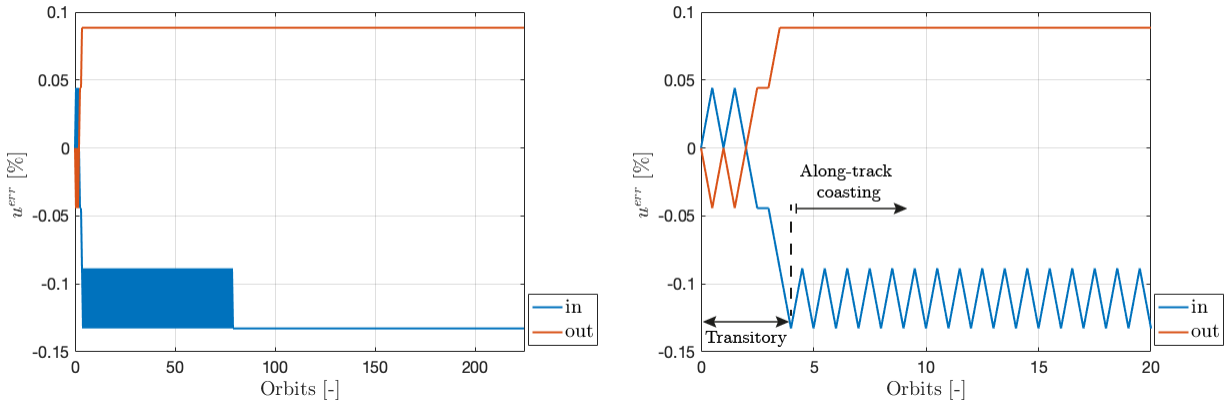

Figure 5.8: Relative shift of u_{in} and u_{out} along the orbits for the first half of the simulation, in the case $h_{2\pi} = 50$ m.

in u_{out} is a consequence of the discrete nature of the problem. Generally speaking, the greatest result observable is the effectiveness of the control algorithms in maintaining the positions of u_{in} and u_{out} along the orbits.
With these relative shifts of about ± 0.1 % (i.e. $\approx \pm\, 0.04\,^{\circ}$) the size of the imaging windows gets slightly modified as reported in Figure 5.9. The changes in the size, normalised with respect to the first span $u_{out0} - u_{in0}$, show a reduction of about 0.2%, coherently with the results of the relative shift analysed above.

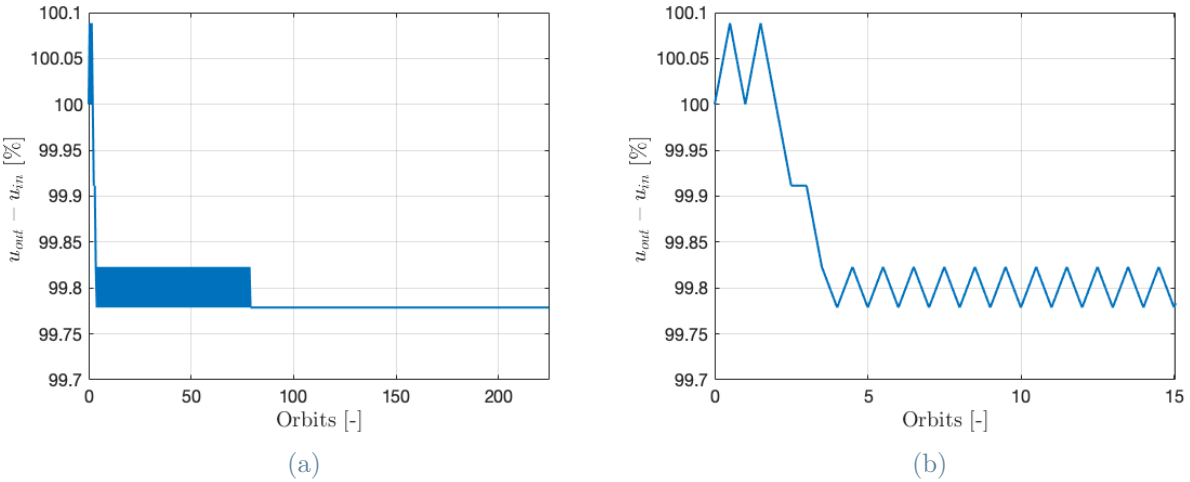

Figure 5.9: Imaging window size for the first configuration of the case study $h_{2\pi}^{obj} = 50$ m.

The discussion above should have clarified the importance analysing both these results: for the control strategy to be effective, it is necessary not only that the windows maintain

their size (apart from small acceptable variations), but also that their location is kept fixed along the orbits.

To better understand the results presented above, it can be interesting to study the evolution of the ROE over time when subject to control actions. In this sense, probably the most important to start with is the relative semi-major axis δa, since it's the principal source of drift in the lobes of the curve. Figure 5.10 reports its evolution over the first 15 days of simulation.

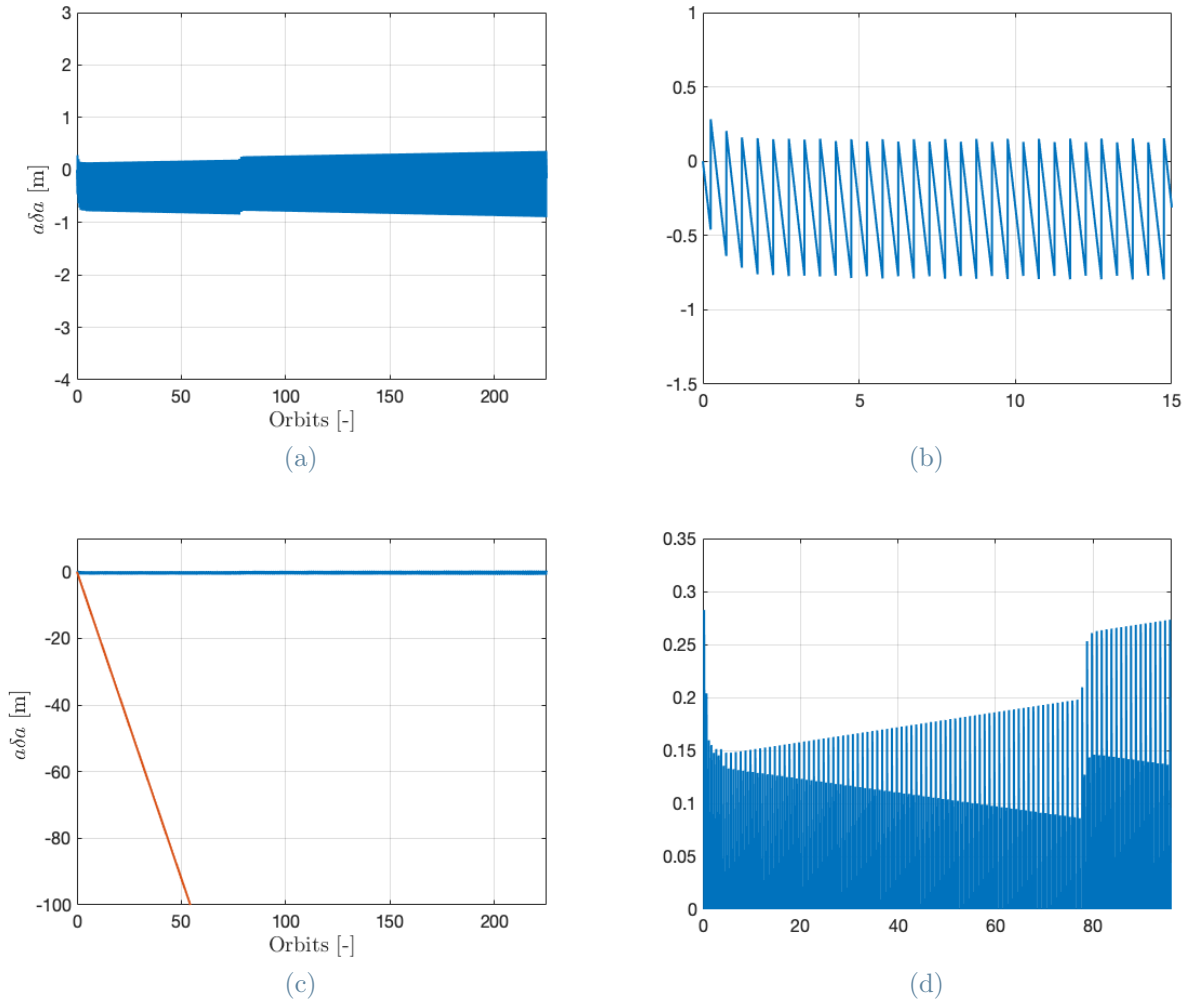

Figure 5.10: First case study. Relative semi-major axis evolution, subject to the control actions for the first 15 days of simulation (a) and a detail of the initial 15 orbits (b). Image (c) shows the effect of control in comparison with the evolution in case of free motion (red line), and image (d) gives a zoom on the fringes.

The first thing noticeable at a glance looking at image 5.10.c is the overall effect of the control actions when compared to the free motion case: to maintain a stable height am-

biguity, is necessary to keep a small δa. More in detail, the plots show that after the transitory the relative semi-major axis keeps oscillating around -0.6 m. During recovery this average gets raised because of the additional manoeuvres, staying anyway close to zero. By looking closer (Figure 5.10.d), it's possible to note an intrinsic asymmetry in the curve, with one lobe in each orbit higher than the other. This characteristic behaviour, introduced by the control actions, will be encountered commonly in the results of both the case studies, and is justified by the small evolution of the ROE (and thus the perpendicular baseline) in the orbits.
Once the behaviour of the semi-major axis is accounted for, the remaining degrees of freedom of the problem (δv_r and δv_n) are tuned to refine the solution and exploit as much as possible the ± 2 m range of height ambiguity available.
This can be somehow noted looking at the evolution of the relative eccentricity and inclination vectors. In Figure 5.11 it's possible to distinguish between two different behaviours:

- a **short term** evolution, in the time scale of the orbital period. It's characterised by small cyclical variations of the vectors' magnitudes, that increase in the first half of the orbit and decrease in the second (or viceversa). This particular pattern can be clearly linked to the asymmetry observed and commented above.
- a **long term** evolution, in which $a\delta e$ rises and $a\delta i$ lowers. This is the result of the adaption of the control scheme to the complex interaction between the secular variation of the relative perigee ϕ and the relative ascending node θ (introduced by J_2) and the orbital decay (caused by drag) that change the atmosphere's density and the values of $B_\perp^{min}$, $B_\perp^{max}$ every orbit.

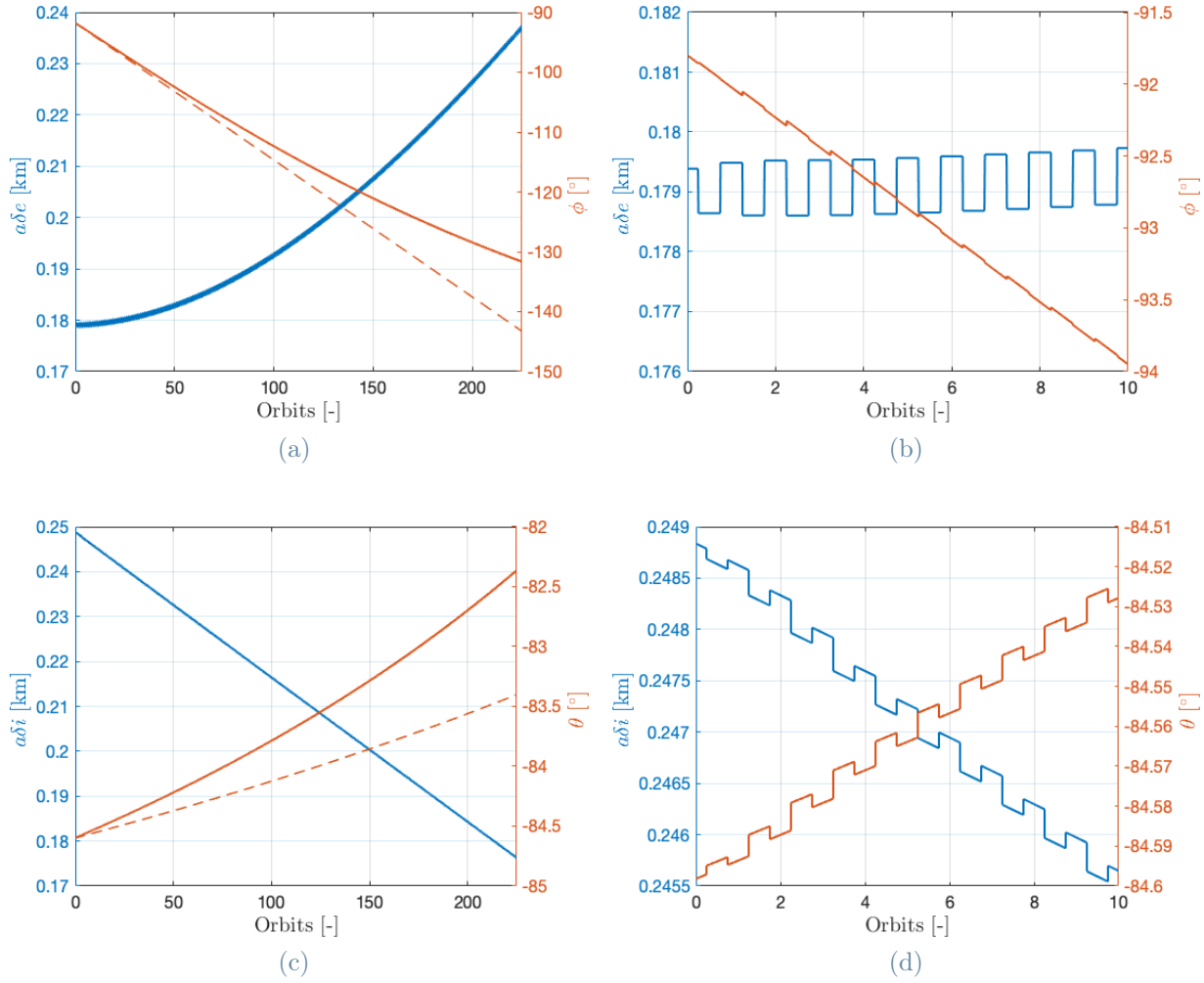

Figure 5.11: First configuration, case study $h_{2\pi}^{obj} = 50$ m. The evolution of norm and phase ϕ of the relative eccentricity vector (a), zoomed in (b), and the relative inclination vector (c), zoomed in (d). The dotted lines represents the variation of the phases in case no control is applied to the spacecrafts. In both the vectors it is possible to recognise the short term and long term variations.

To conclude the presentation of the effectiveness of the control scheme, the only thing that's left to verify is the safety requirements satisfaction. This part is strictly related, in particular, to the along-track position control, and the phases of coasting and recovery. Looking at Figure 5.12, is possible to see that for the first part of this simulation the strategy adopted does its job in maintaining to the along-track position where desired.

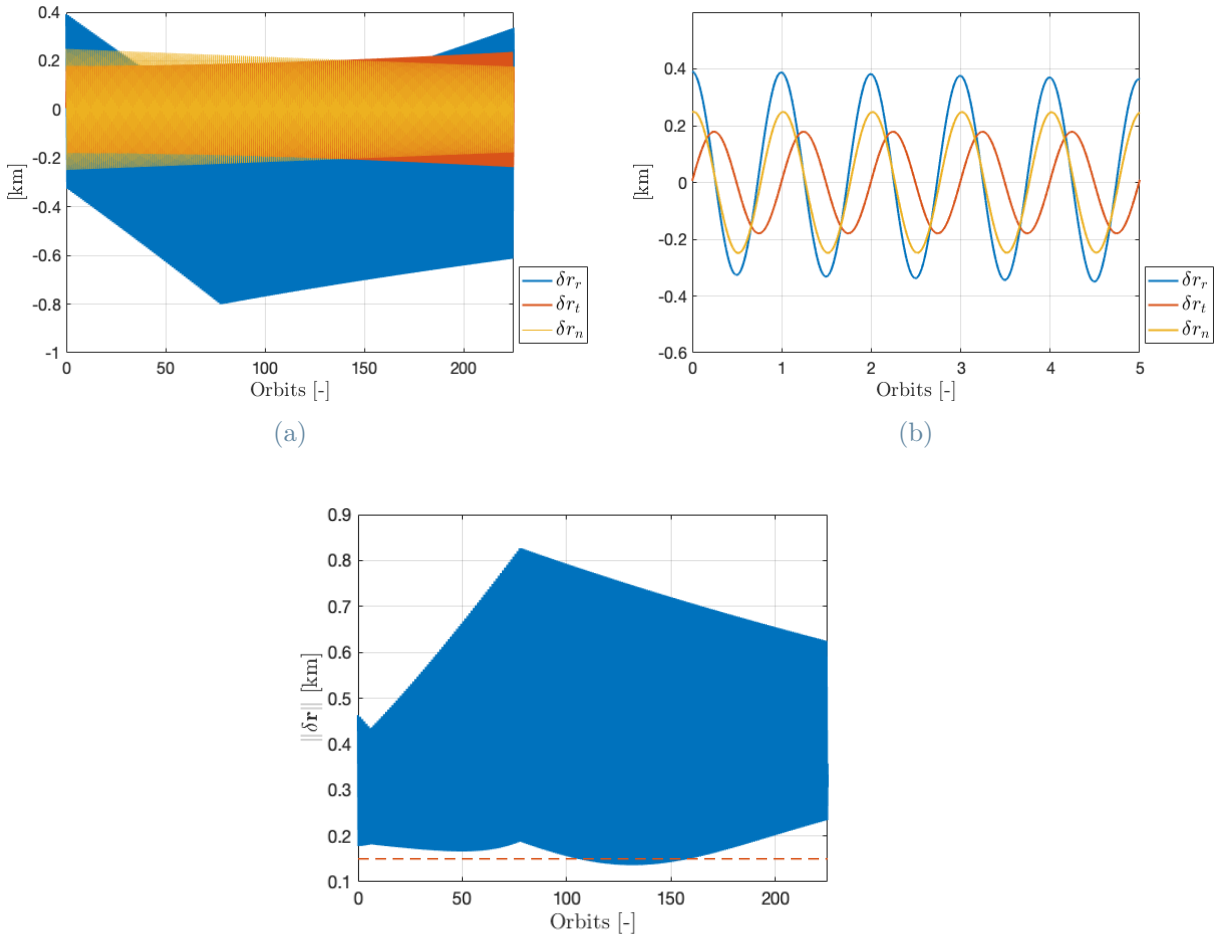

Figure 5.12: Relative positions of the spacecrafts for the first configuration of the case $h_{2\pi}^{obj} = 50$ m. In (a) and (b) the evolution of the three components of $\delta \boldsymbol{r}$. It can be noted the effect of the along-track recovery phase on δr_t, together with the long term evolution of the amplitudes δe and δi. In (c) the norm of $\delta \boldsymbol{r}$, where the dotted line identifies the lower boundary on the distance of 150 m.

However, during the recovery between orbits 100 and 150 it is noted that the spacecrafts get to find to distances lower than the safety limit. This is because of the evolution of the three components of $\delta \boldsymbol{r}$ and their relative phases, caused by both the perturbations and the control actions. Figure 5.13 shows that in correspondence of the region where δr_r and δr_n have relatively small norms (in the order of 200 m), during recovery the peaks of δr_t get to find close to zero, causing an overall inter-satellite distance lower than 150 m. A practical solution to this problem could be to modify the triggers of the along-track control strategy. Starting the coasting phase when the valleys of δr_t get above -150 m, and

switching to recovery when the peaks get below 150 m, it could be possible to ensure an inter-satellite distance larger than the prescribed limit with an additional safety margin given by the non-zeros radial and out-of-plane positions. The relative trajectory of the deputy for the coasting phase is pictured in Figure 5.14.

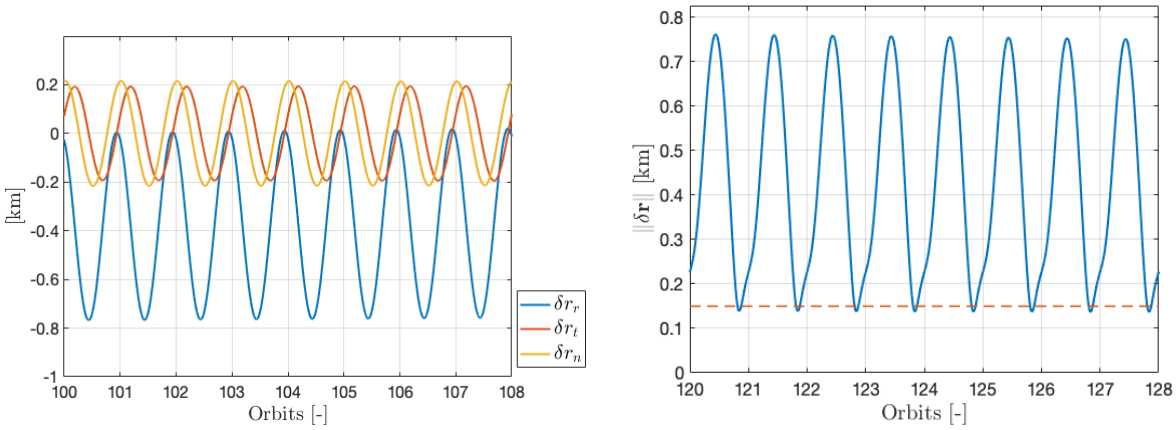

(a) (b)

Figure 5.13: Zoom of the out-of-boundary condition. In (a) it's possible to identify the contributes of each component of $\delta \boldsymbol{r}$, while (b) reports the overall norm.

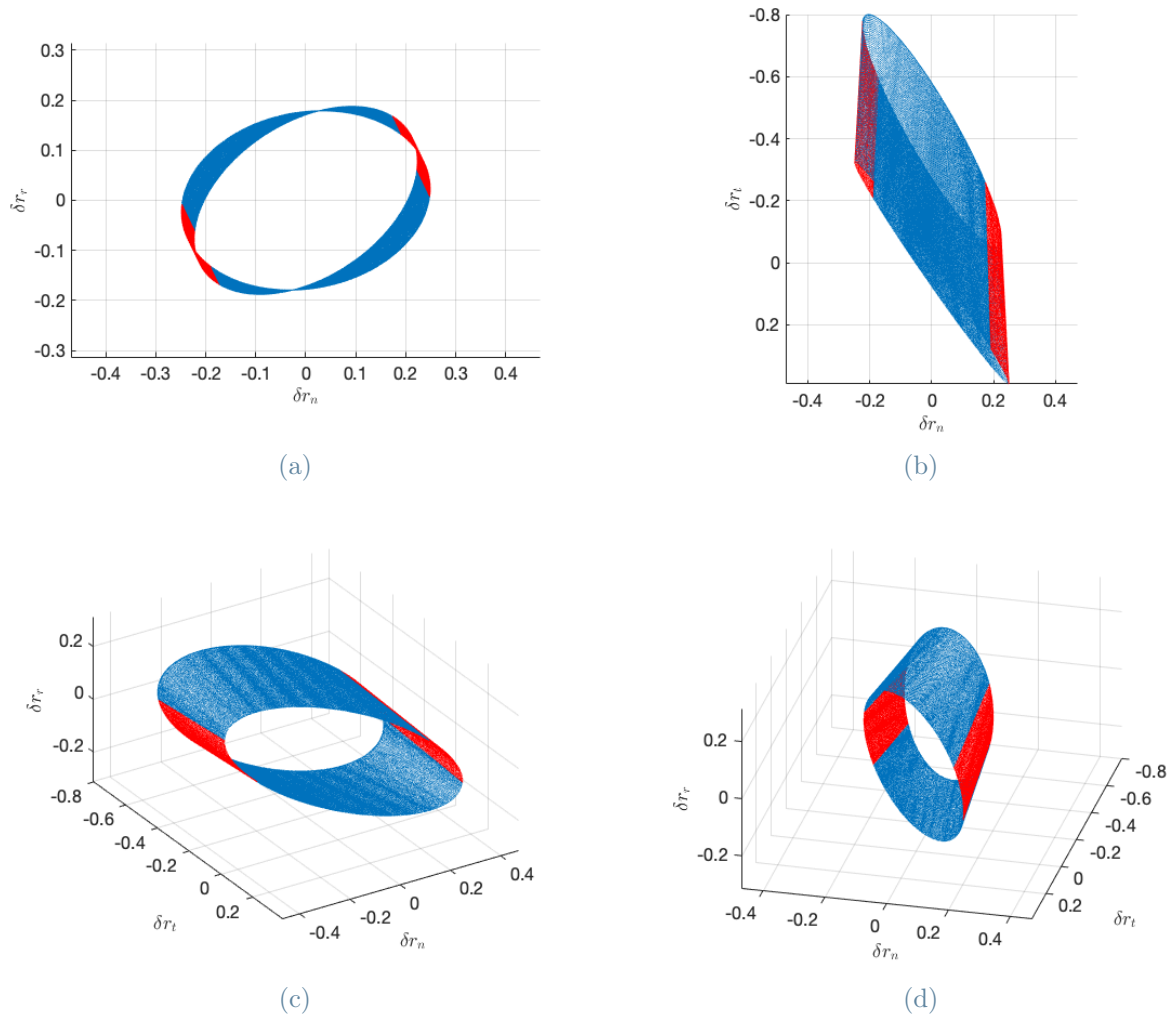

Figure 5.14: Different views of the deputy's relative trajectory, limited to the along-track coasting phase for clarity.

All the results above come from the first half of the simulation, related to the first configuration. After the reconfiguration manoeuvre, the control system has to deal with a new initial condition and new requirements to satisfy. In this sense, the greatest difference with the previous configuration is the shorter time span between the manoeuvres instants (always located at $u = \pi/2 + k\pi$) and the windows for imaging.
From the height ambiguity point of view, Figure 5.15 shows a trend similar to the one observed in the previous configuration. It's possible to distinguish the presence of an initial oscillatory phase lasting around five orbits (a bit longer with respect to the previous case of three), in which the curve, again, gets below the 48 m limit. The control system, adapting to this violation, rises the value of h_{min} bringing back safely the curve inside the boundary. From this point on, the curve will remain above the 48 m limit for the rest of the simulation. In the end, the height ambiguity remains inside the limits for more than 99.998% of the time. The points u_{in} and u_{out}, because of the transitory, slightly shift from the respective initial values of about 0.68° and 0.9° respectively. But since they shift in the exact same way, in the end, the size of the imaging windows remains almost constant, reduced by only 0.2° with respect to the initial span. In general it's possible to note that the intervals, this time, have visible oscillations, larger than the discretisation step but anyway limited in the range of tenths (or even hundredths) of a degree.

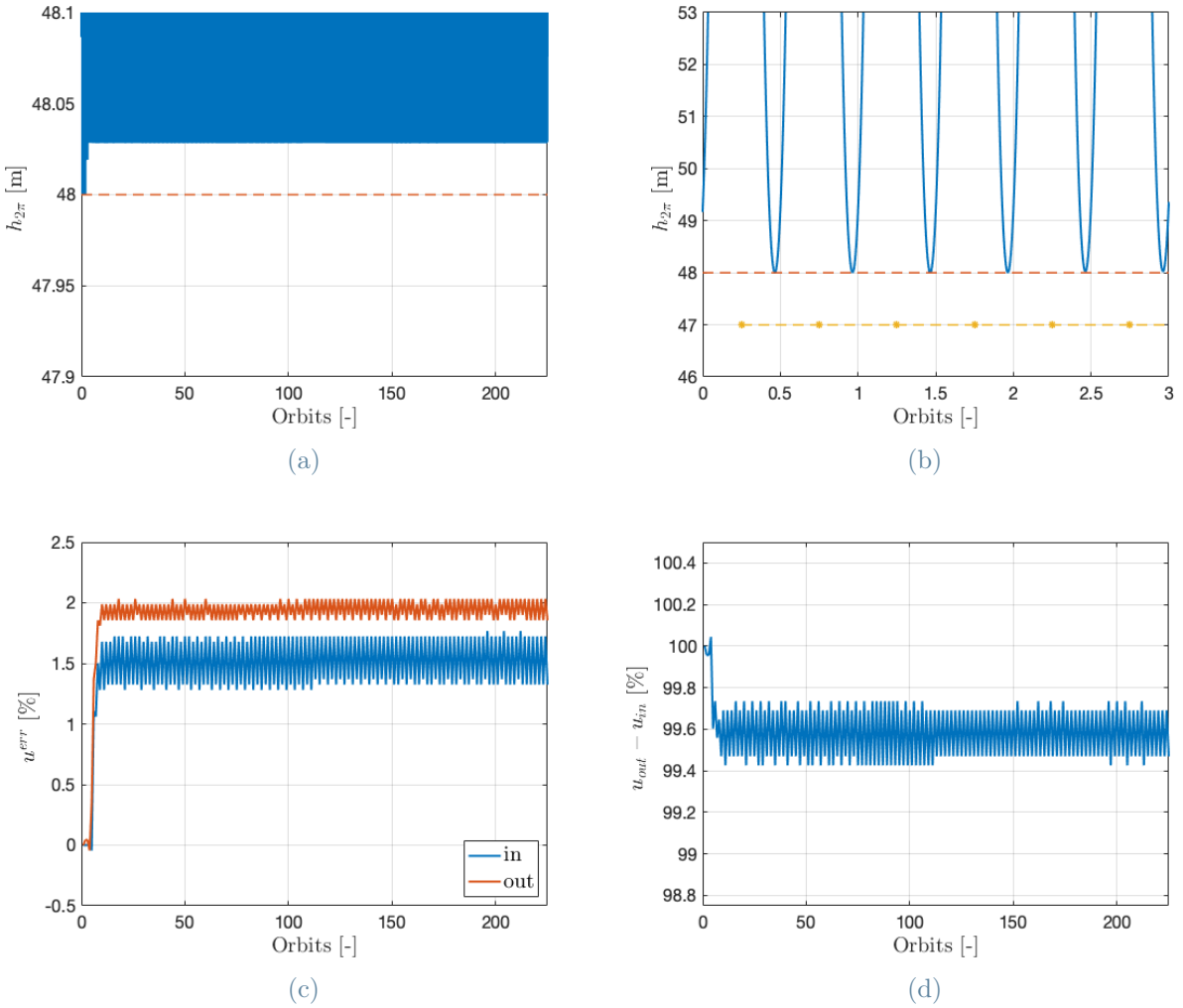

Figure 5.15: Simulation results for the second configuration with $h_{2\pi}^{obj} = 50$ m. In (a) an overview of the height ambiguity, detailed in (b) and shown together with the manoeuvres location (the yellow dots). Image (c) shows the relative shift of the instants u_{in} and u_{out}, with respect to the new u_{in0} and u_{out0}. To conclude, in (d) the relative variation of the window size during the 15 days.

Also the ROE (Figure 5.16) follow a trend similar to the one observed in the previous configuration, even if with some important differences. After the transitory, the relative semi-major axis is kept around an average value of -1.5 m, almost three times the average value of the previous configuration, and shows oscillations more intense in amplitude. Furthermore, as can be better seen if Figure 5.16.b the asymmetry in the orbits is more evident in this configuration, with the first impulse of each couple of manoeuvres smaller than the second.

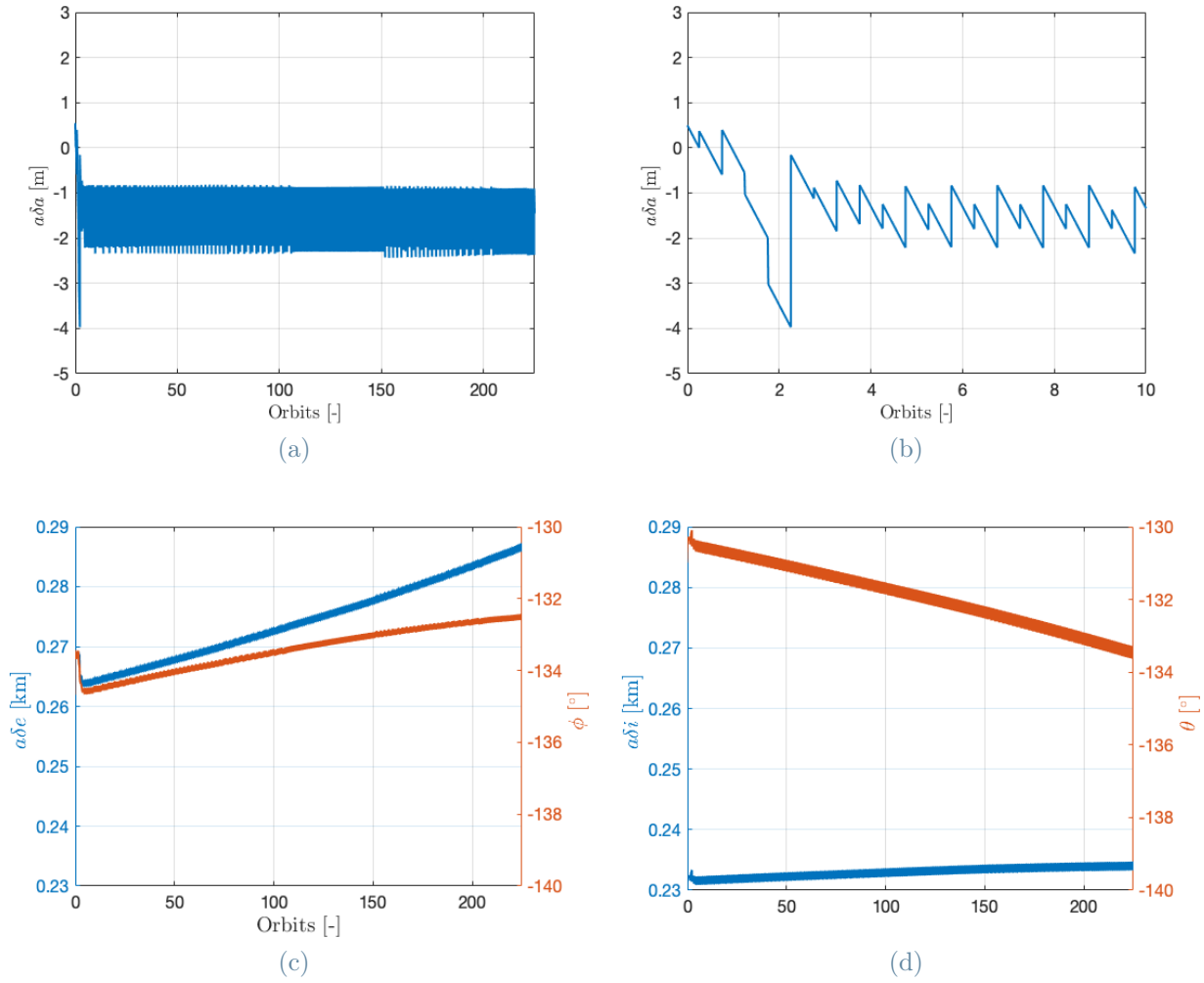

Figure 5.16: ROE variation for the second configuration, case study $h_{2\pi}^{obj} = 50$ m. A close resembling can be found in particular with the plots in Figure 5.11, regarding the relative eccentricity and inclination vectors of the first configuration

The relative eccentricity and inclination vectors show overall smaller long-term variations: a few degrees for the phases, that maintain the quasi-parallel vectors condition, and some meters for the norms. The short-term evolution in the orbits instead is still present, with slightly enhanced amplitude in the oscillations. The resulting relative positions, reported in Figure 5.17, point out an unexpected condition. Looking in particular at the along-track position, it is observed that the distance δr_t keeps increasing even during the coasting phase, bringing the spacecrafts to a distance of 900 m after 15 days. Trying to search for the causes of this strange behaviour, it can be useful to recall the expression of

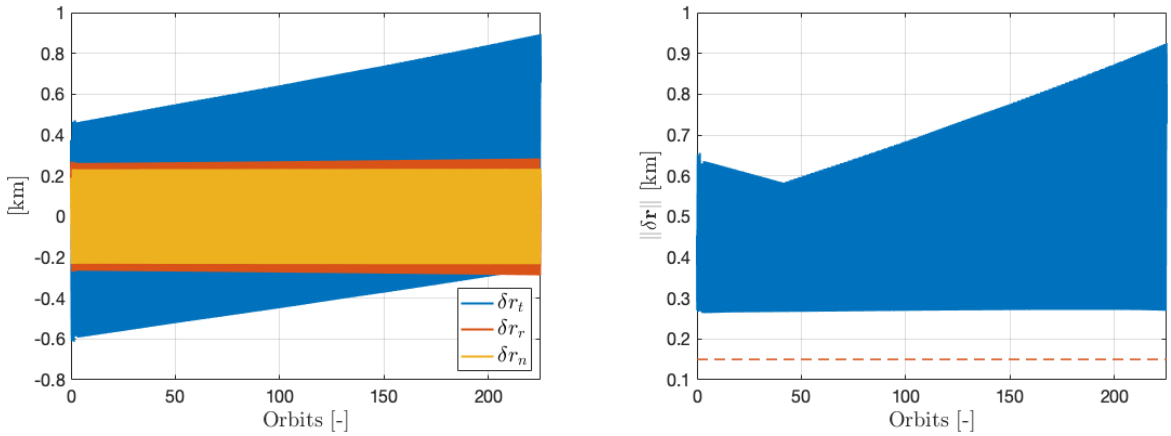

(a) (b)

Figure 5.17: Relative positions of the spacecrafts (a) and inter-satellite distance (b) in the second configuration, for the case study $h_{2\pi}^{obj} = 50$ m. It's possible to note the slow long term evolution of δe and δi, and the effects of the large drift introduced by the relative semi-major axis on the along-track component.

the along-track position as function of the mean argument of latitude:

$$\delta r_t / a_c \propto -\frac{21}{2}(\gamma \sin(2i_c)\delta i_{x,0} + \frac{1}{7}\delta a_0)(u(t) - u_0) + \frac{3}{4n^2}\Delta B \rho a_c v_c^2 (u - u_0)^2 \; - \; 3\Delta(\delta v_t)(u - u_M)/n$$

where constant/harmonic terms were discarded, retaining only the quantities that introduce a drift in time, that are essentially those related to $\delta\lambda$ and its evolution. To understand which are the roles of each term in the definition of this relative orbital element, it's possible to have a look at the plots in Figure 5.18. These represent the evolution of the single terms that contribute to the relative mean longitude evolution, compared with the longitude itself. To have a proper comparison, each of the terms in the equation above is compared with a mean longitude "unwrapped" with respect to the initial conditions. It means that, while the classical simulation of the relative dynamics foresees at each manoeuvre instant to update the new initial condition and propagate until the next manoeuvre time, the $\delta\lambda$ term represented below instead is obtained without the initial condition update. Thus, it represents the real changes introduced in $\delta\lambda$ instant per instant, without considering the history of its evolution.

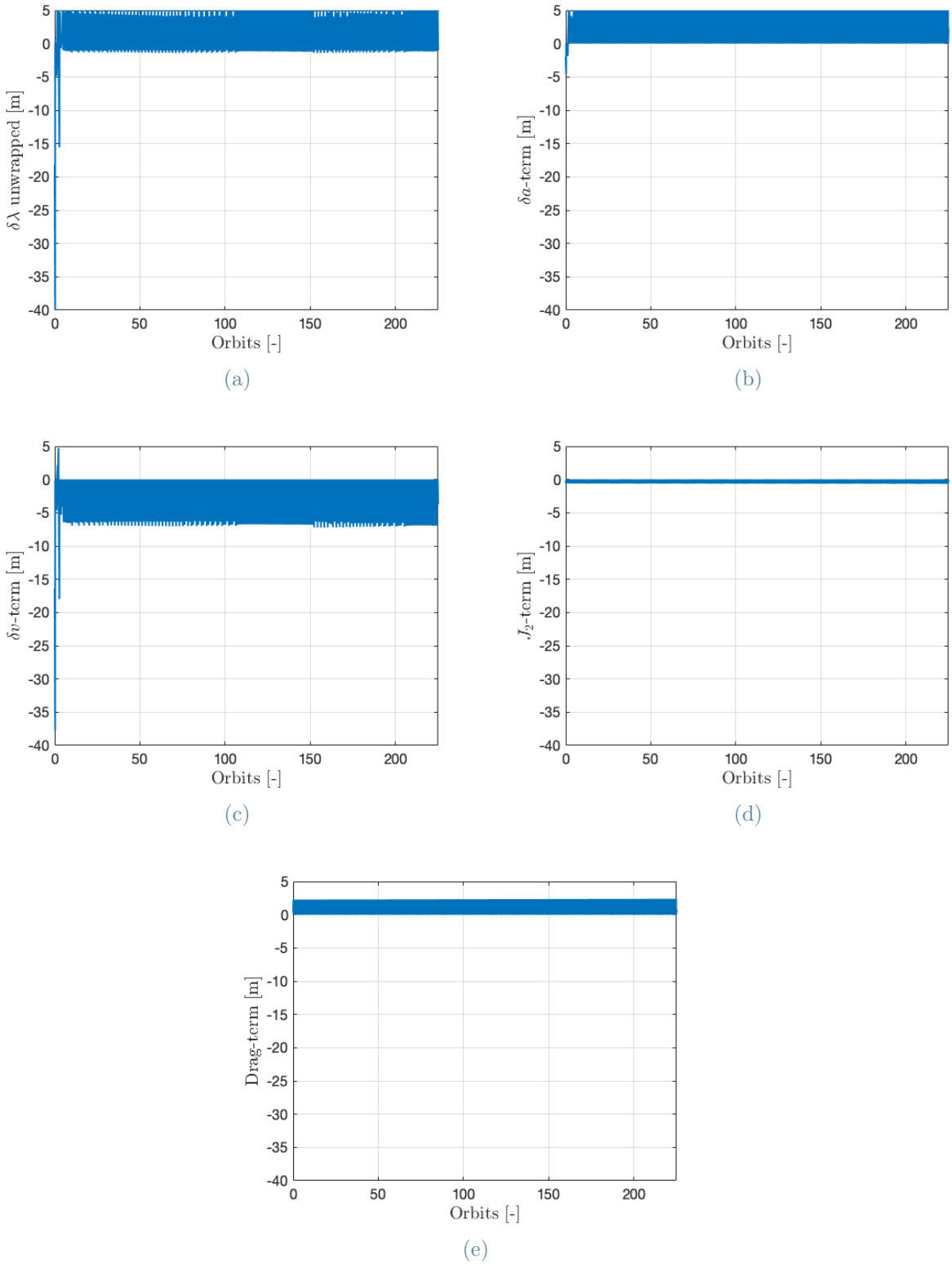

Figure 5.18: Comparison term-by-term to identify the cause of the undesired along-track drift of the second configuration. In (a) the unwrapped mean longitude, in (b) and (c) respectively the terms related to the semi-major axis and the along-track impulses, clearly linked to the first plot. The last two images represent the effects of perturbations: J_2 (d) and drag (e).

Looking at the figures it's possible to see that the most influencing terms are those given by the relative semi-major axis and the along-track manoeuvres drifts. This means that the cause of this undesired behaviour is the solution found by the optimisation itself, that requires a too large (negative) semi-major axis to maintain the imaging windows along the orbits, and consequently introduces that strong, positive, along-track drift.
It's possible to note this also looking back at the plot of δa in Figure 5.16.a. The initial orbits maintained an average relative semi-major axis much smaller than the -1.8 m value notable after the along-track recovery (ca. orbit 40). This results evidence an important limit of the along-track position control strategy adopted: being based on the assumption of a small relative semi-major axis, once it has to deal with values of negative δa too large (and this example identifies this "too large" to be, at least, in the order of -1.5 m on average) it cannot be used anymore, since there's a too strong natural drift.
Trying to solve this problem maintaining a smaller semi-major axis by applying larger manoeuvres would be counterproductive for two reasons: firstly, it would interfere with the solution of the optimisation and the scientific objectives of the mission. Secondly, it would rise even more the consumption of propellant, and hence ideally the overall mission complexity and the costs. Furthermore, it should be considered that the 1 km limit on the maximum distance was imposed with the aim of maintaining the validity of the relative motion model close to its maximum. Overcoming this boundary doesn't necessary mean to jeopardise the mission or its objectives, but just reducing the accuracy of the solution. It is therefore important to verify the impact this violation has on the reliability of the results, through a proper validation.
The overall relative trajectory for this second configuration is plot in Figure 5.19

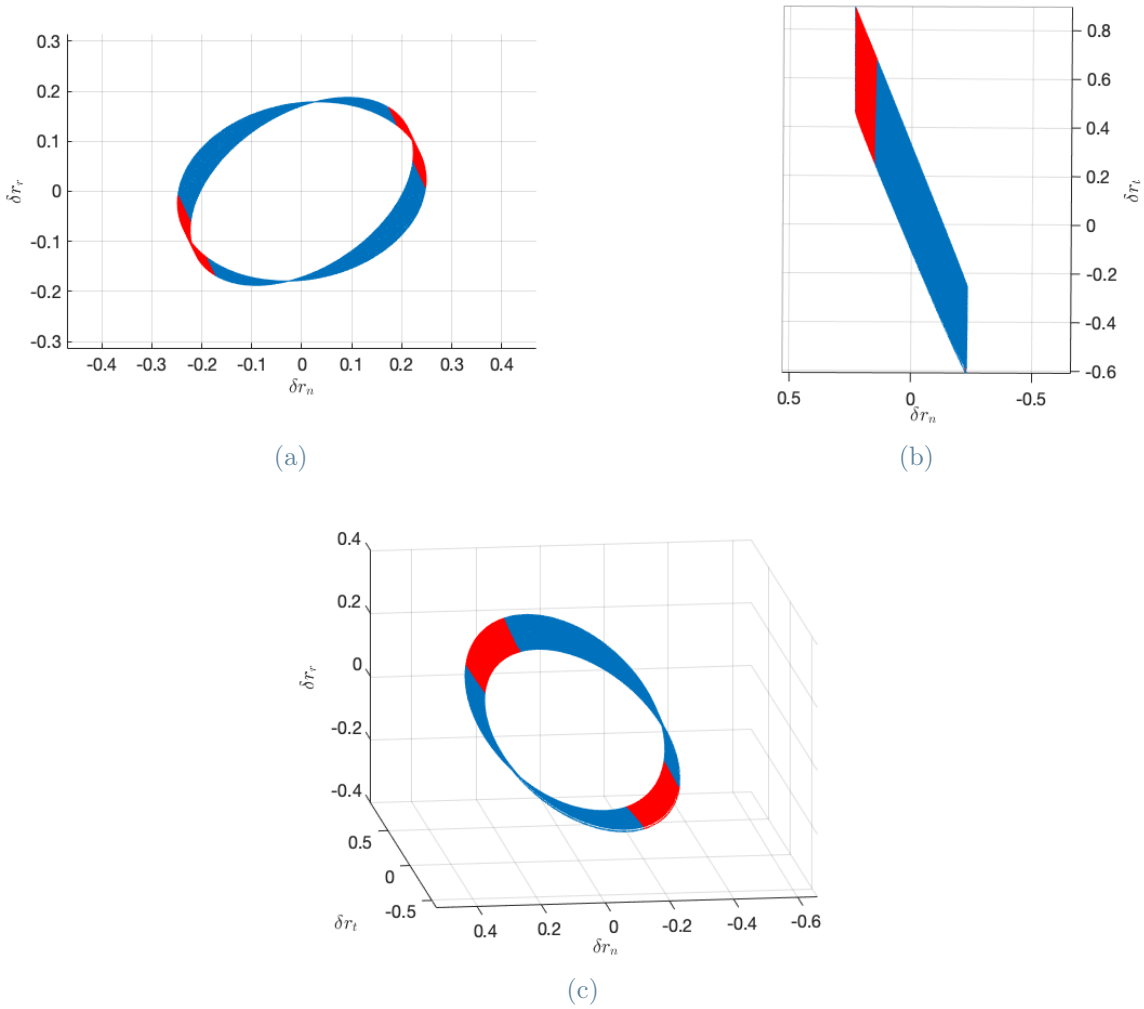

Figure 5.19: Different views of the deputy's relative trajectory for the second configuration.

The analysis of this case study is concluded with the report of the algorithms performances in Table 5.3 and the information about the total δv required for the control (Table 5.4 and Figure 5.20). The total impulse in the second configuration is found to be about three times larger, accordingly to the tighter control perceivable through the shorter excursions of the ROE. To have an idea of the applicability in real-life contexts, these results can be compared with data coming from past missions. Taking as benchmark the mission TanDEM-X, during scientific activities in average conditions it foresees each day two manoeuvres of about 0.5 cm/s each [15], thus about 10 mm/s per day. The results of the simulation here proposed require an average of 17 and 53 mm/s per day. The results are larger, but in the same order of magnitude of the benchmark. Therefore, the results can be considered realistic. Furthermore, it has to be considered that the operational

conditions of the two spacecrafts of TanDEM-X are a bit different. Specifically, the two have been designed to exhibit very similar drag coefficients, resulting in a very small relative semi-major axis decay of about 10 cm per day, while for the simulation under exam, as observed in Figure 5.10, the decay is about 30 m per day. By changing the relative ballistic coefficient to 0.0001 m^2/kg (two orders of magnitude smaller), it was verified that the total impulse (at least for the first configuration) can be lowered to 2.5 mm/s per day.

Algorithm	No. iterations	Duration	No. repetitions
roe_initial	3	1.5 s	1
correct_h	5	4.1 s	900
Algorithms simulation time:		1 hour 4 min	
Relative dynamics simulation time:		5 hours 51 min	
Reconfiguration simulation time:		3 min	
Total simulation time:		6 hours 58 min	

Table 5.3: Algorithms performances for the Extended Simulation of the first case study. The algorithms and the relative dynamics simulation times define the total duration of the scientific activity simulation.

The number of iterations and the duration in Table 5.3 are meant on average. The data reported focus on the algorithms directly involved in the scientific activity simulation, without detailing those related to the reconfiguration that will be commented in the next section. The algorithms prove to be very fast in the problem solution, and converge within a small number of iterations, never exceeding the fixed maximum of 12.

Parameter	Config. 1	Config. 2
$h_{2\pi} \geq 48$ m	≥ 99.999 % of time	≥ 99.998 % of time
u_{in}^{err}	- 0.12 % (0.045°)	+ 1.5 % (0.68°)
u_{out}^{err}	+ 0.1 % (0.04°)	+ 1.9 % (0.9°)
$u_{out} - u_{in}$ %	99.8 % (45.26°)	99.6 % (45.08°)
δa average	- 0.6 m	- 1.6 m
$\Delta\delta e$ (end - start)	+ 60 m	+ 15 m
$\Delta\phi$ (end - start)	- 40°	+ 2°
$\Delta\delta i$ (end - start)	- 70 m	+ 5 m
$\Delta\theta$ (end - start)	+ 3 °	- 4°
$\Delta(\delta v_{tot})$	263.15 mm/s	789.6 mm/s
$\Delta(\delta v)$ for recovery	3.5 mm/s (1.33% of total)	0 mm/s

Table 5.4: Sum up of the results achieved in the two configurations of the first case study.

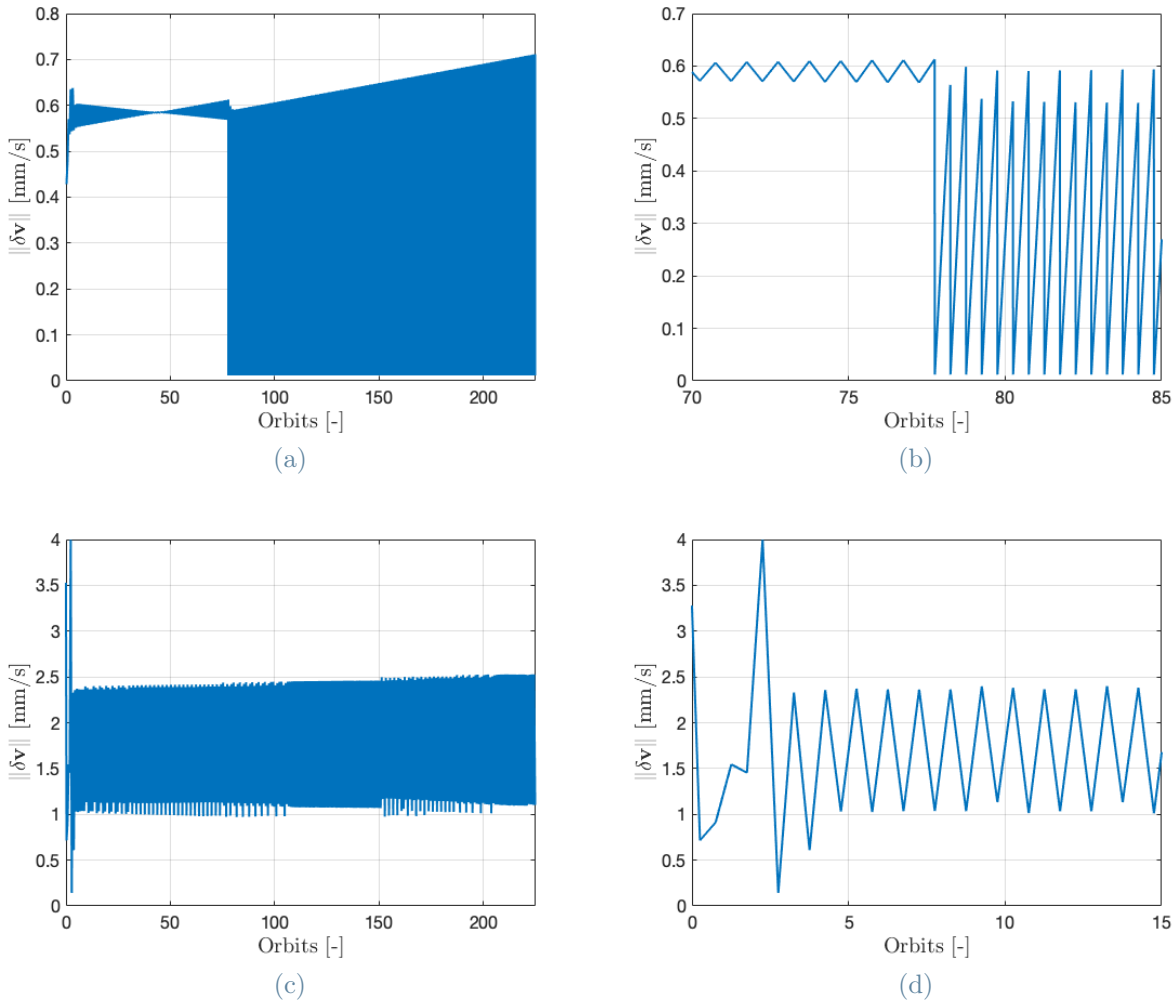

Figure 5.20: Magnitude of the impulses for the first (a) and the second (c) configuration. Detail (b) shows the how the additional impulses for along-track recovery, given 30 seconds after the main manoeuvres, are effectively small when compared to them. Detail (d) instead points out the behaviour of the solution in the transitory of the second configuration.

5.1.2. Reduced Simulation

The reduced simulation instead aims at showing the results of the various reconfiguration manoeuvres. For the first case study, as observed in the previous simulation the imaging windows cover about 44.3° of mean argument of latitude each, that's 12.3 % of each orbit. Considering that there are two windows for every orbital period, it is sufficient to employ five configurations to cover all the latitudes reachable, including also an adequate overlay margin between adjacent configurations. In fact:

$$12.3\% \frac{\text{coverage}}{\text{lobe}} \quad \times \quad 2 \frac{\text{lobes}}{\text{configuration}} \quad \times \quad 5\,\text{configurations} = 123\% \text{ total coverage}$$

which means that the lobes of the last and the first configurations, in case no overlapping is considered, would overlay for 23% of the windows duration. Because of the high redundancy in this case study a good choice for this margin could be 9° (20% of the window), far more than sufficient to handle the relative shifts u_{in}^{err} and u_{out}^{err} observed in Table 5.4 and adequate to evenly spread the overlaying between configurations.
The algorithms implemented require to input the desired number of manoeuvres for each reconfiguration. Since no constraints have been defined in this sense, the results shown in this section will arbitrarily consider six manoeuvres for each reconfiguration. However, it has been verified that the algorithms are capable of adapting over a large range of total manoeuvres (with a minimum of four): generally speaking it was observed that the overall variations introduced in the ROE are similar, and the higher is the number of manoeuvres, the lower is the total $\Delta(\delta v)$ required. This can be verified by looking at Figure 5.21, where the total impulses required for different number of manoeuvres are reported for both the case studies.

The results of the Reduced Simulation for the first case study, considering 6 maneuvers per reconfiguration, are reported in Figure 5.22. The plot compares the lobes in the first orbit after each reconfiguration (identified by a number, e.g. configuration 1 = # 1) There are two interesting things to note. First of all, the efficacy of the manoeuvres: the lobes are correctly shifted backwards along the orbit, remaining inside the ±2 m range around the objective value of 50 m. The second thing is the regularity of the solution: the lobes get similarly shifted of about the same degrees, determining a quasi-uniform superimposition pattern for imaging. A qualitative idea of this result can be obtained by looking at Figure 5.23, where the average values of the overlay windows for the configurations under exam are reported. The overlay between configurations #1 and #5 is just reported for completeness, since it's not consequential to a direct reconfiguration.

The relative error of the overlay margin in the first and fourth reconfigurations is main-

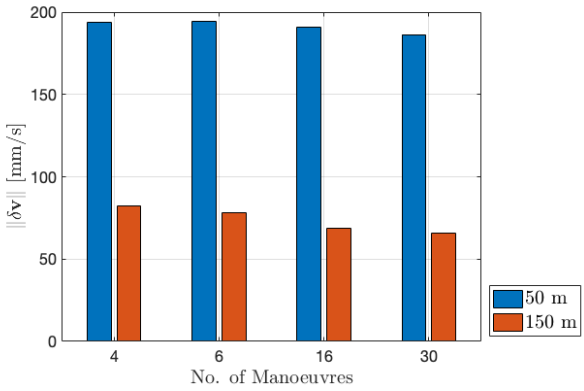

(a)

Figure 5.21: Total $\Delta(\delta v)$ in the first reconfiguration for a different number of total manoeuvres: 4, 6, 16 and 30 (one day). In blue the values for the case study $h_{2\pi}^{obj} = 50$ m, in red for $h_{2\pi}^{obj} = 150$ m.

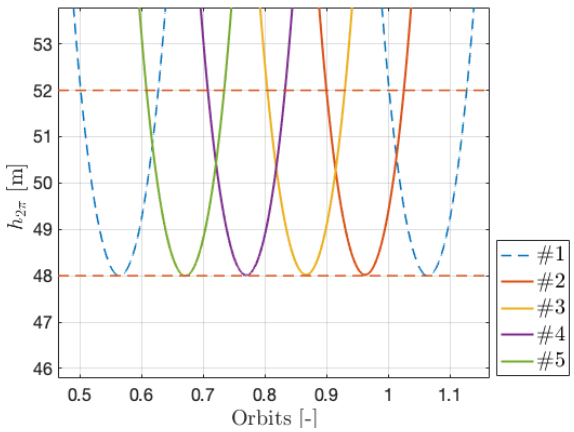

(a)

Figure 5.22: Reconfiguration results for the first case study. The lobes belong to the first orbits of each configuration (numerated in the legend).

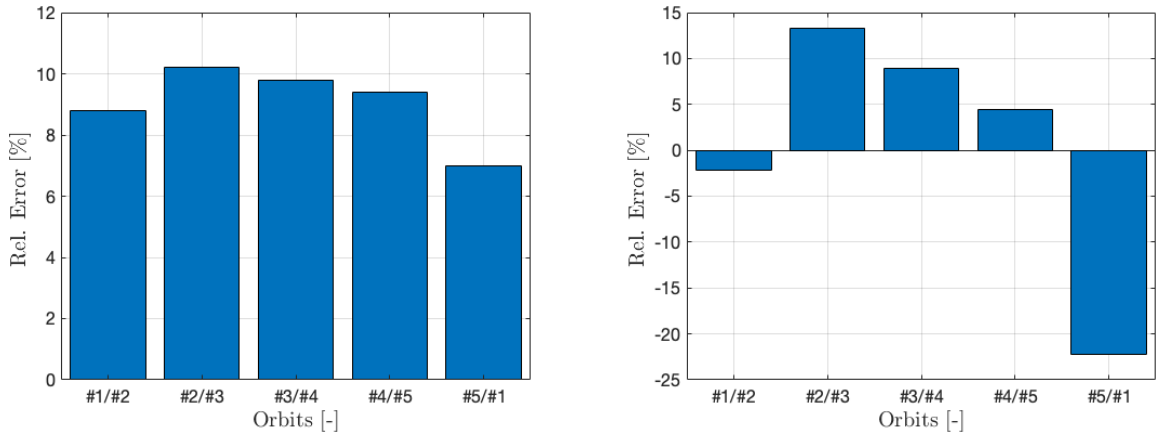

Figure 5.23: Average size of the overlay windows (a) for adjacent couples of configurations and relative error (b) of the size with respect to the 9° objective.

tained within a ±5% range (i.e. ±0.45°) around zero. It's possible to note that instead the passages that involve configuration #3 show larger deviations, up to 15%. In principle, this is not a problem because as long as there's a positive error it means that the overlap between the configurations is higher than programmed, thus the solution found is just more conservative and does not represent a hazard for the scientific objectives. Nevertheless, it's important to understand which are the motivations behind this behaviour.
By looking at Figure 5.24, it's possible to note two important characteristics in the plot of the height ambiguity for this simulation.

The first thing to note is that during reconfiguration, the optimisation sometimes fails at maintaining the curve close to the 48 m limit. For the purpose of the mission, this is not a problem since the satellite are not expected to image the ground in this phase; however, this inaccuracy might partly justify the differences observed in the sizes of the overlay windows with respect to the desired value of 9°. The second thing to note is that the curve of the third configuration shows small fringes, and remains a little bit higher than the lower limit. There's a justification for this behaviour.
Since the lobes in each configuration get shifted backwards in the orbits while the deviation-control manoeuvres are fixed, it happens that at a certain point the lobes are found too close to the manoeuvres location for the control system to find a stable solution. It is hence necessary to introduce a shift in the control, where each manoeuvre is used to correct the behaviour of the lobe immediately following the lobe closer to the manoeuvre instant. The logic of this shift in the control windows is illustrated in Figure 5.25.

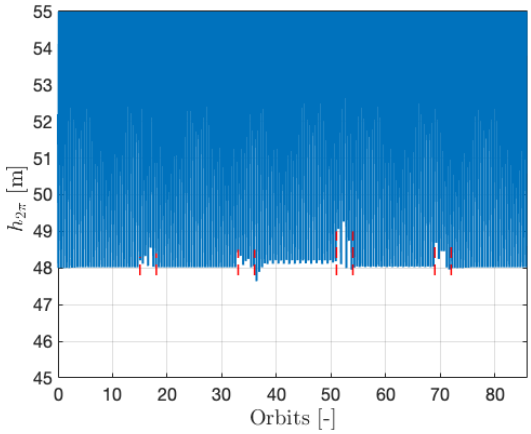

(a)

Figure 5.24: Reduced simulation result for the height ambiguity of the first case study, where it's possible to recognise the 5 science phases and the following reconfigurations. As observed in the Extended Simulation, each scientific phase shows an initial transitory of few orbits in which it might happen that the lobes overpass the 48 m limit.

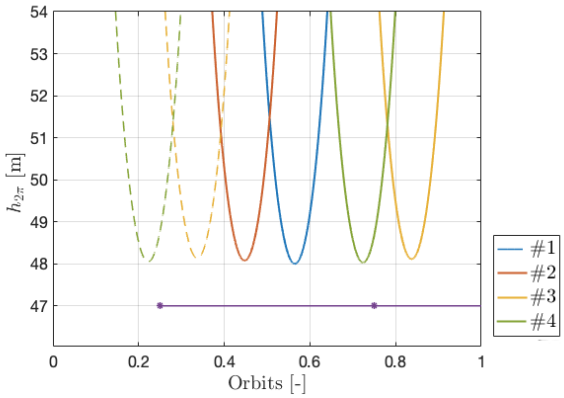

(a)

Figure 5.25: Control windows shift for the first case study, considering four configurations. The purple dots identify the location of the manoeuvres, exploited to control the windows contoured by solid lines.

In this case study, the configurations interested by the control windows shift are the number #3 and the number #4. However, while in configuration #4 the control manoeuvre for each window is executed inside the immediately previous window (thus the latter is not so much affected by the manoeuvre), in configuration #3 the manoeuvres are executed a slightly before. This causes each manoeuvre to have a small interference with the solution imposed through the previous maneuver: that's why the lobes in this configuration remain

slightly above the 48 m limit. Furthermore, the lobes are slightly displaced/distorted in the orbit. This shift is the principal cause of the deviations previously observed in Figure 5.23 where the overlay windows among configuration #3 resulted larger with respect to the others.
To better understand the effects of the reconfiguration manoeuvres it might be useful to have a look at the variations introduced in the ROE. The relative eccentricity vector

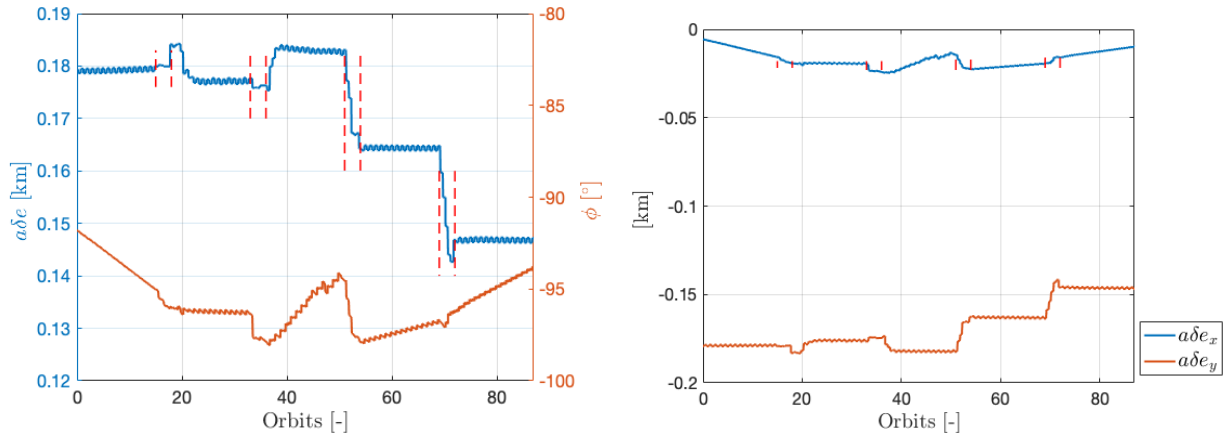

Figure 5.26: Relative eccentricity vector variations during the Reduced Simulation, in polar representation (a) and Cartesian (b). The red dotted lines delimit the reconfiguration manoeuvres.

(Figure 5.26) is slightly controlled. The most important changes imposed with each reconfiguration mainly address the y-component while the x-component is kept small. In general it's possible to note how after each reconfiguration the transitory might introduce from small to sensible changes, but mostly in the norm. During scientific activities instead this vector is kept almost unchanged. The relative inclination instead, in Figure 5.27 shows a more regular behaviour and the effects of each reconfiguration are more evident. During scientific activities, its norm and phase are maintained approximately constant, while the reconfiguration manoeuvres instead enlarge the magnitude and decrease the phase. In the passage form the configuration #4 to the #5, both the components are raised, determining a 180° shift in the phase because of the passage from negative to positive of the y-component. The stronger changes applied to these ROE demonstrate how the relative inclination vector has, for the control algorithms, a crucial importance to shift the lobes along the orbits, even higher than the relative eccentricity. In particular, it is noted how in reconfigurations where the norm of $\delta \boldsymbol{i}$ has stronger variations, the norm of $\delta \boldsymbol{e}$ undergoes smaller changes, and viceversa. To conclude, the relative semi-major axis shows important excursions, in the order of some meters. In this simulation this ROE

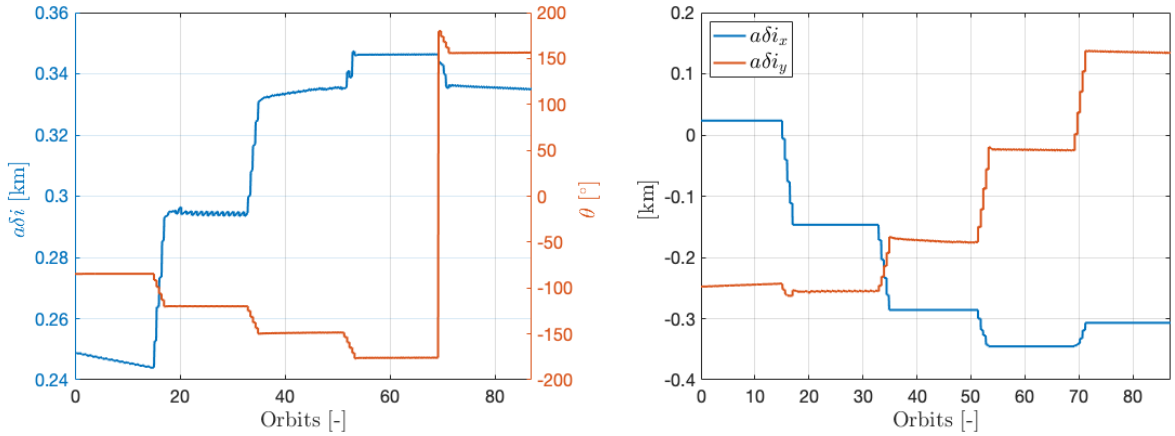

Figure 5.27: Relative inclination vector variations during the Reduced Simulation, in norm (a) and phase (b) and Cartesian components (c).

becomes of secondary importance, for two reasons. First of all because its major effect is to determine a shift in the altitude of the lobes, rather than on their position along the orbit. The variations observed in Figure 5.28 are mainly side effects of the desired variations of the relative eccentricity vector, that explain the voids observed in the height of ambiguity in Figure 5.24. And secondly, because the last impulse of each reconfiguration is designed to cancel these undesired variations induced in the previous manoeuvres, to facilitate the beginning of the scientific activities.
The results presented above refer to the Reduced Simulation with 6 reconfiguration manoeuvres. The values of the total $\Delta(\delta v)$ required for each reconfiguration are reported in Table 5.5 and in Figure 5.29 categorised by algorithm.

In general it's possible to see that all the reconfigurations have very similar costs in terms of impulses, and that the last manoeuvres to correct the deviations introduced in the relative semi-major axis are less than 1.5% of the total cost. Comparing with the results in Table 5.4 it's possible to see that despite having a much lower number of maneuvers, because of the higher impact on the ROE each reconfiguration requires a total $\Delta(\delta v)$ larger than the results of the scientific activity in the Extended Simulation. The algorithms performances are reported in Table 5.11.

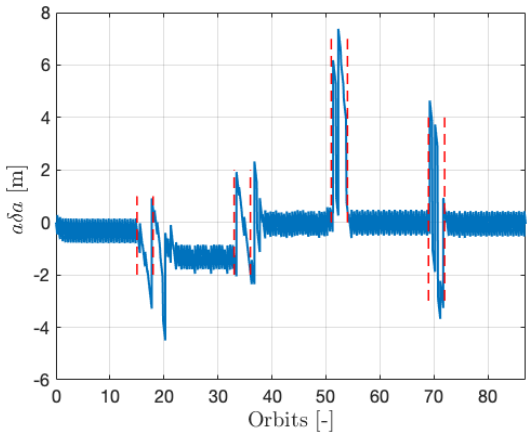

(a)

Figure 5.28: Relative semi-major axis variations in the Reduced Simulation, first case study.

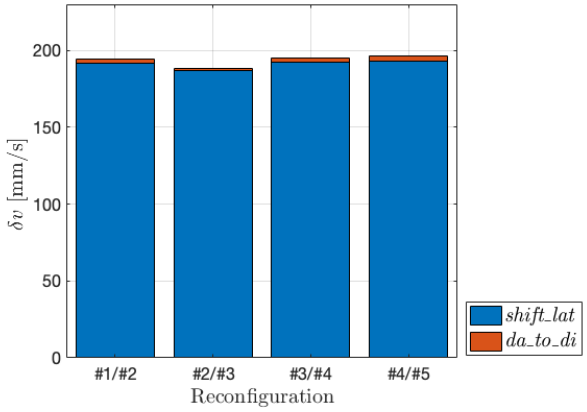

Figure 5.29: $\Delta(\delta v)$ of the reconfiguration manoeuvres for the first case study. In blue the $\Delta(\delta v)$ found with algorithm *shift_lat*, in red the δa corrections computed by algorithm *da_to_di*.

Reconfiguration	$\Delta(\delta v)$ [mm/s]
#1/#2	194.27
#2/#3	188.09
#3/#4	194.72
#4/#5	196.11
Total	801.3

Table 5.5: Total $\Delta(\delta v)$ for the reconfiguration manoeuvres.

Algorithm	No. iterations	Duration	No. repetitions
shift_lat	7	23 s	15
da_to_di	5	9 s	3
Reconfiguration simulation time:		9 min	
Scientific activity simulation time:		20 min	
Total simulation time:		29 min	

Table 5.6: Algorithms performances for the Reduced Simulation of the first case study. For the number of iterations and the duration, the values shown are meant on average.

5.2. Case study $h_{2\pi}^{obj} = 150$ m

The second case study considered has a shorter range of perpendicular baseline available for science, between 140.2 and 144 m. The optimal initial condition found for this scenario is reported in Table 5.7, while figure 5.30 represents the behaviour of the height of ambiguity and the inter-satellites distance over time starting from this initial condition, again in case no control is applied to the spacecrafts. Table 5.8 reports the critical boundaries for this case study, along with the relevant mapping parameters.

$a\delta a$	$a\delta\lambda$	$a\delta e_x$	$a\delta e_y$	$a\delta i_x$	$a\delta i_y$
0 m	4.02 m	-180.8 m	-114.1 m	-49.9 m	-30.7 m

Table 5.7: Optimal initial condition found for the case $h_{2\pi}^{obj} = 150$ m.

Look Angle	Swath	Duty Cycle	$B_{\perp}^{crit}$	δr_t^{crit}	δr_t trigger
40°	61.4 km	8'48"	7.21 km	25.79 km	±800 m

Table 5.8: Mapping parameters and critical quantities for the second case study. The duty cycle is referred to a single orbit.

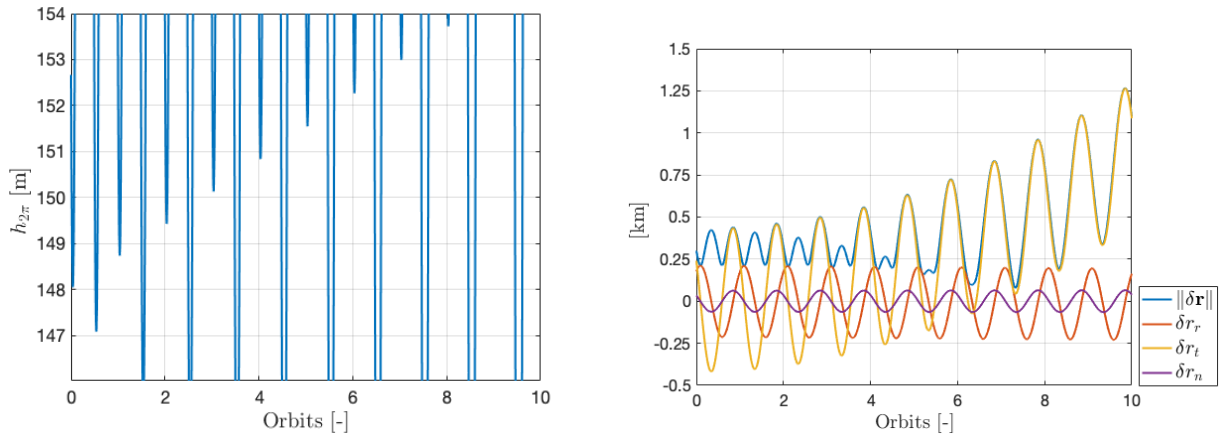

(a) (b)

Figure 5.30: Evolution over time of the height ambiguity (a) and spacecraft's distance together with the components of $\delta\boldsymbol{r}$ (b) for the case $h_{2\pi}^{obj} = 150$ m in conditions of free motion.

It can be observed that this time the height ambiguity valleys drift much faster from the target of 148 m: this scenario proves to be more sensible to the semi-major axis variations introduced by drag, reaching a difference from the objective value larger than 1 m after

just one orbit (i.e. 1.5 hours). This behaviour can be justified by the smaller value of the perpendicular baseline, that subject to the same semi-major axis variation of the previous case causes this larger drift. Because of this, it is expected that in this case more attention will be necessary for the control strategy actuation.
The inter-satellites distance instead behaves similarly to the previous scenario, and the spacecrafts get to the limit distance value of 1 km after more or less nine orbits of free motion conditions, again because of the along-track drift introduced by drag.

5.2.1. Extended Simulation

Figure 5.31 represents the result of the valleys drift correction for the first configuration in the case under exam. Again, the scientific requirements results satisfied for the majority

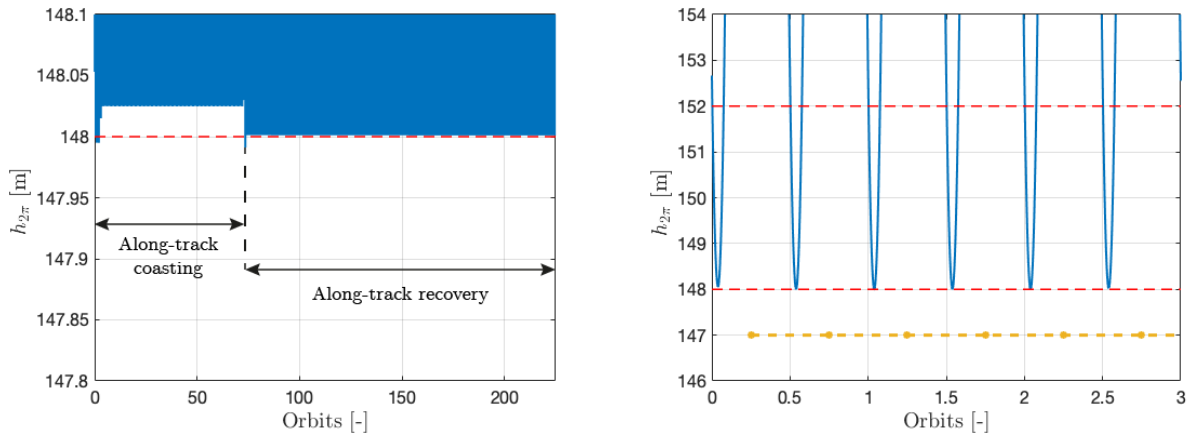

Figure 5.31: A zoom of the lower limit (a) and a detail (b) of the height ambiguity plot for the case $h_{2\pi}^{obj} = 150$ m. In (b) the dots on the line on the bottom represent the manoeuvre instants of the first configuration.

of the time. However, it is possible to note that during the first orbits of the simulation the lower limit gets shortly violated a couple of times. In Figure 5.32 it's possible to see that the curve shows, again, a short transitory (ca. two orbits), in which the minima decrease until they get below 148 m. At this point the control system detects the limits violation and updates the value of h_{min}, raising it up by 1 cm.
The curve enters then a stable phase, maintained for the rest of the simulation.
Close to the end of the fifth day (orbit 73), the coasting phase ends. At this point the control system starts the position-recovery phase, that can be identified by the fringes in the Figure 5.33, present because of the asymmetry introduced by this additional impulse. Because of this manoeuvres, during the very first orbit of the recovery phase the control

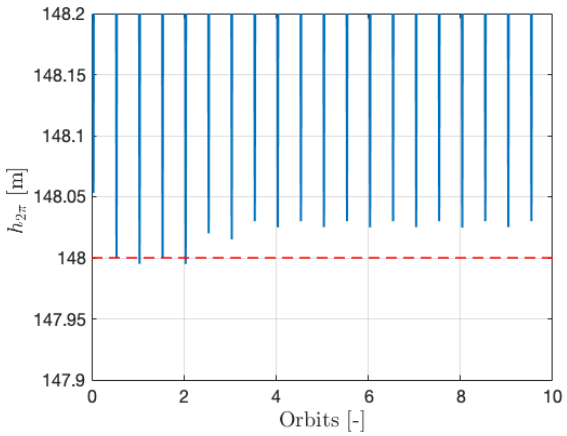

(a)

Figure 5.32: Initial transitory with violation of the lower boundary (orbits 1 and 2) and successive recovery. The plots refer to the first configuration of the case study $h_2\pi = 150$ m.

system detects another crossing of the lower boundary, and raises the limit value of h_{min} by another centimeter: this operation ensure a continuous scientific activity above the lower boundary for the rest of the simulation. In the end, the condition $h_{2\pi} \geq 148$ m is verified for 99.999% of the time.

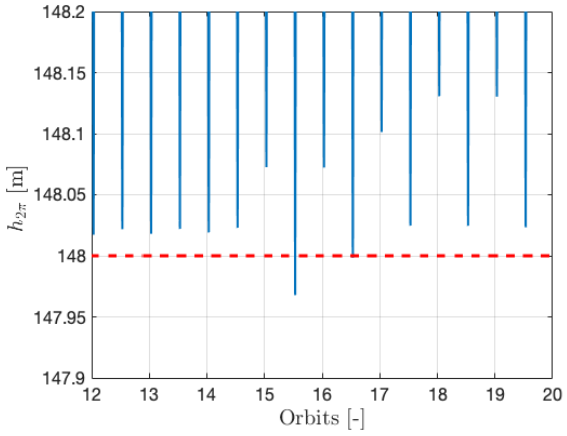

(a)

Figure 5.33: First configuration, case study $h_{2\pi}^{obj} = 148$ m. Begin of the along-track recovery phase (a) with the second (and last) boundary violation.

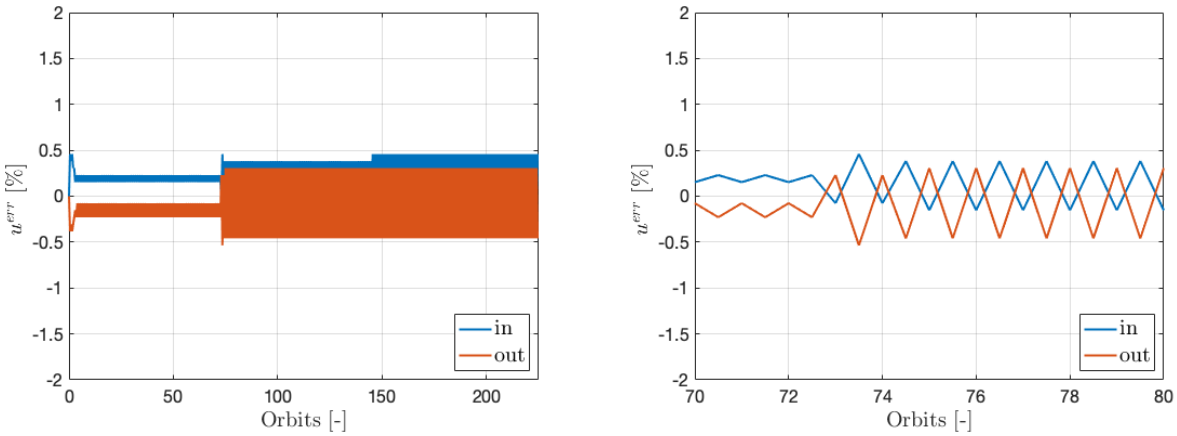

Figure 5.34: Relative shifts of u_{in} and u_{out} for the first configuration, in the case $h_{2\pi}^{obj} =$ 150 m. In (b) a detail of (a) focused on the beginning of the along-track recovery phase.

For what concerns the upper boundary of 152 m instead, the results of interest can be found in Figures 5.34. In the images it's possible to recognise the features already observed in the height of ambiguity: the initial transitory, the along-track coasting and the recovery phase, identified by the larger oscillations introduced with the additional manoeuvre. For both the instants u_{in} and u_{out} the relative shifts result fairly contained in small ranges close to zero, with maximum errors of ± 0.5 % ($\approx \pm 0.13°$). It is noted that slightly before the 150th orbit, the shift on u_{in} has a small jump. By inspection it was verified that this jump has the same size of the oscillations observed in the along-track coasting phase in the same plot, that's exactly the same size of the angular step of the temporal variable. Thus, these oscillations are nothing more than discretisation errors of the problem: the real relative shift stays in between the two extremes. The reason why the second error arises during the along-track recovery phase can be identified by looking closely to the height of ambiguity plot: Figure 5.35 shows that after orbit 70 the tips of the lobes get slowly lowered in time, coming closer and closer to the lower limit of 148 m and slightly increasing the distance between u_{in} and u_{out}.

Going deeper, it's interesting to verify how the duration of the time windows available for imaging changes in the orbits. The plots in Figure 5.36 point out that the size of the windows oscillate of about 1.5% of the initial size ($\approx 0.4°$), with an average slightly larger than the beginning. As already done for the previous case study, the next step of the analysis consists in the study of the ROE behaviour when subject to control actions. Figure 5.37 reports the evolution of the relative semi-major axis over the first 15 days simulation.

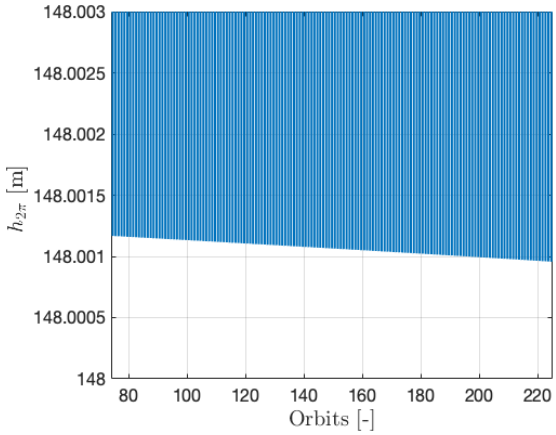

(a)

Figure 5.35: Relative shifts of u_{in} and u_{out} for the first configuration, in the case $h_{2\pi}^{obj} = 150$ m. In (b) a detail of (a) focused on the beginning of the along-track recovery phase.

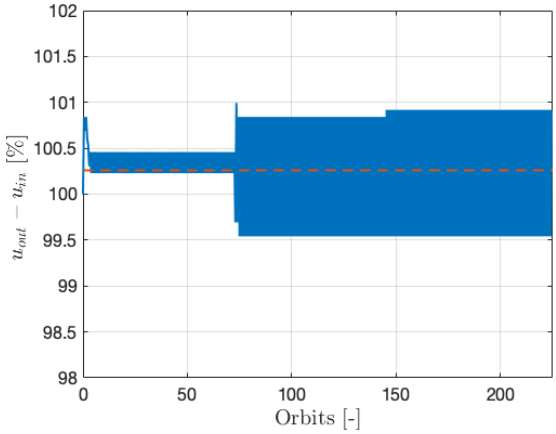

(a)

Figure 5.36: Imaging window duration for the first configuration in the case $h_{2\pi}^{obj} = 150$ m.

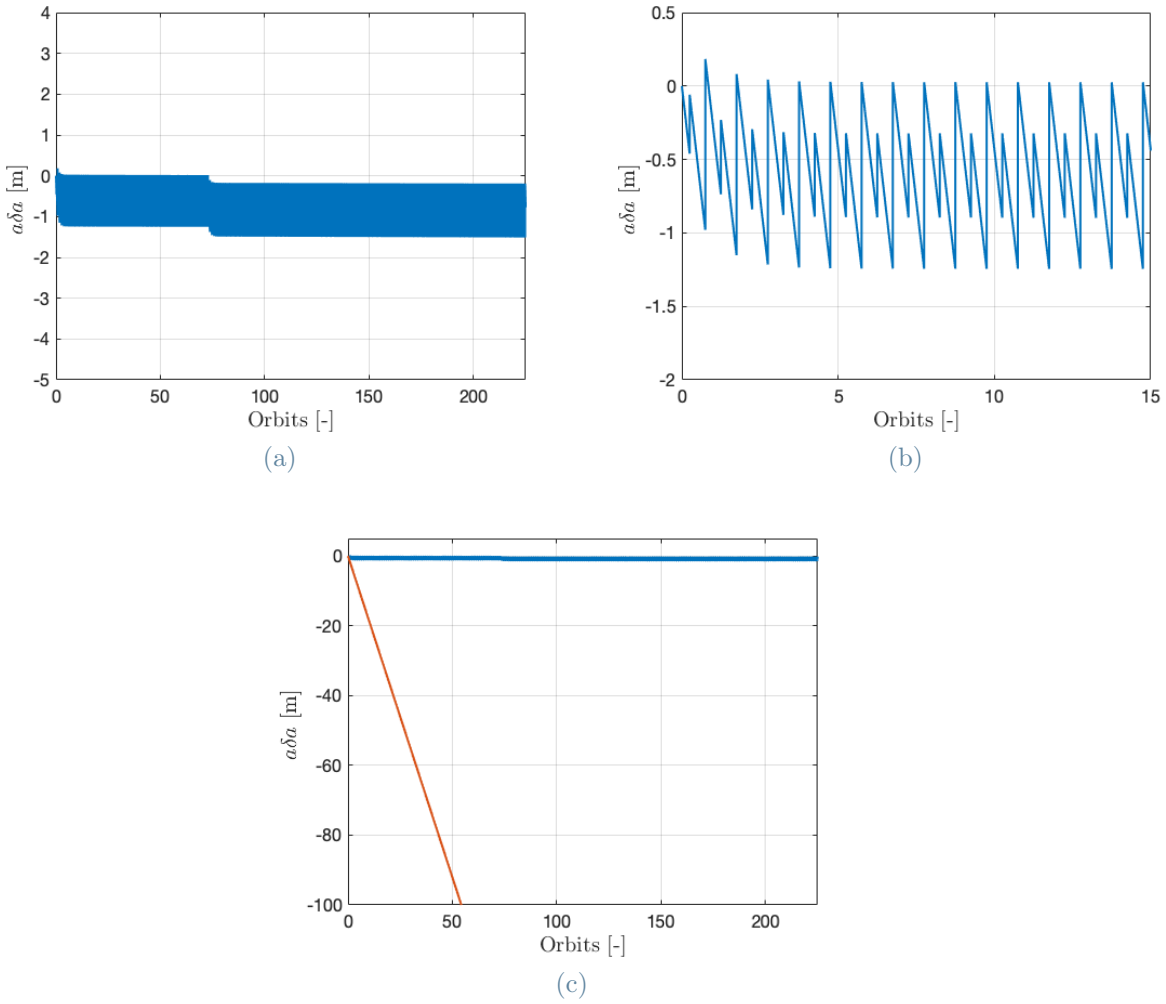

Figure 5.37: Relative semi-major axis evolution, subject to the control action for the case $h_{2\pi}^{obj} = 150$ m, first configuration. In (a) an overview of the evolution for the whole simulation. In (b) a detail of (a), and in (c) a comparison with the evolution in case no control is applied to the Deputy.

Starting from a large scale analysis, it can be observed how again the control acts to keep a small value of δa, with an average of -0.6 m. Then, after orbit 73 the average gets further lowered because of the additional manoeuvres. Figure 5.37.c points out again how for the phase of scientific activity, control of the relative semi-major axis is a key point for the maintenance of the lobes.

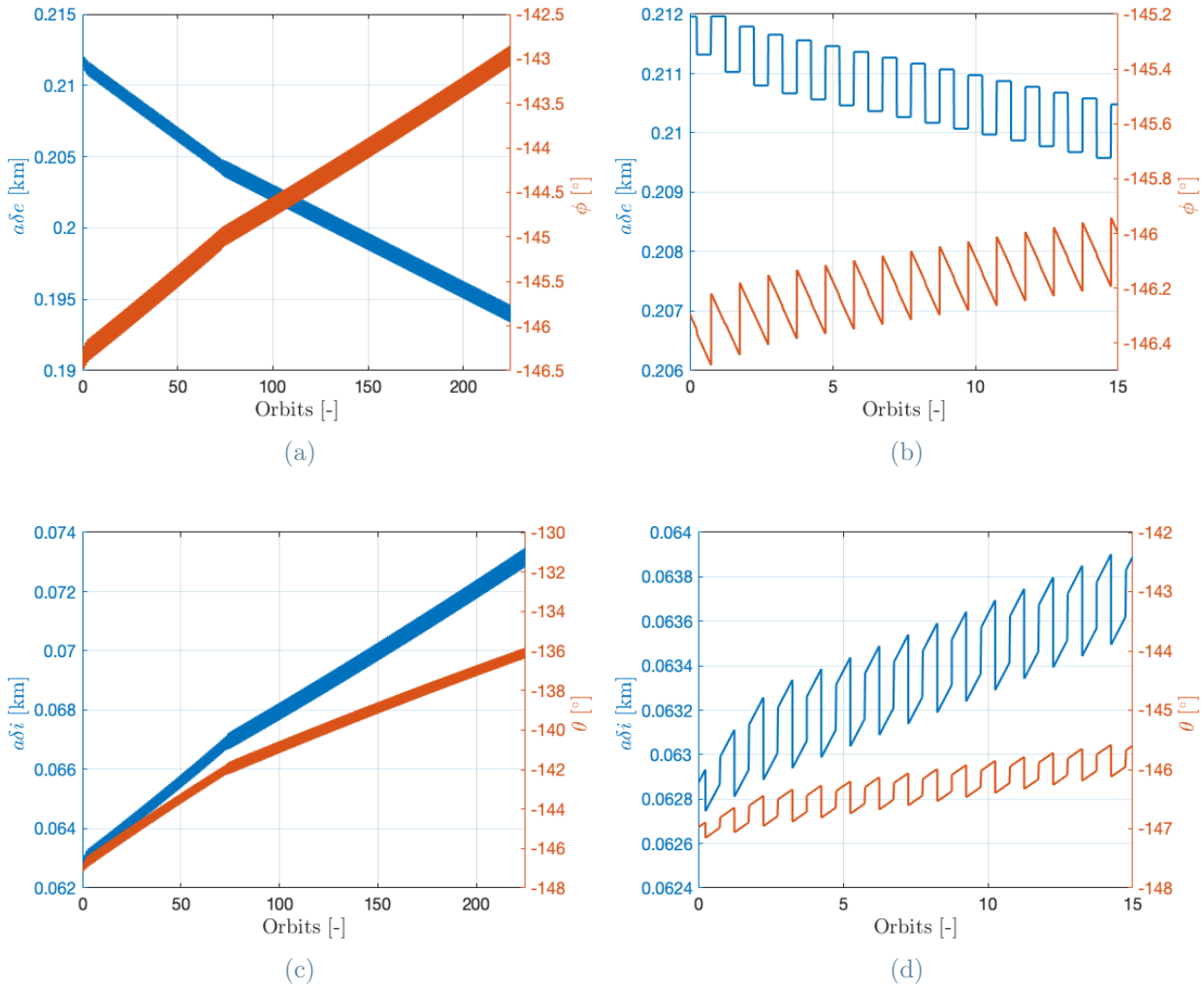

Figure 5.38: Relative eccentricity (a) and inclination (c) vectors over the first half of the simulation, in the case study $h_{2\pi}^{obj} = 150$ m. Images (b) and (d) show that the short term evolution is very similar to the previous case study, with the norms and the phases of the vectors that rise and lower alternating in each orbit.

Proceeding in the analysis, Figure 5.38 represents the effects on the relative eccentricity and inclination vectors. The magnitudes of these vectors are again slightly modified over the simulation, with excursions in the order of 10 m. In general, it's possible to see

that their long term evolution is slower with respect to the previous case study, where in the same number of days $a\delta e$ was raised by almost 60 m, the phase ϕ decreased by 40°, $a\delta i$ by 70. The additional manoeuvres in the recovery phase cause small increases in the magnitudes of the oscillations and a general change of inclination in the curves, slowing even more the ROE variations over time. Nevertheless, it's important to highlight how the relative perigee and ascending node maintain similar phases in the simulation, guaranteeing passive safety to the formation with respect to along-track uncertainties.
The components of the relative position vector represented in Figure 5.39 synthesise the effects of all the results reported. In particular, δr_r and δr_n show much smaller variations over time with respect to the previous case study, as understandable recalling the slow evolution observed of $a\delta e$ and $a\delta i$. The along-track position instead drifts similarly, getting to the limit of -800 m in about five days (73 orbits), and taking more than 10 days to recover the upper trigger.

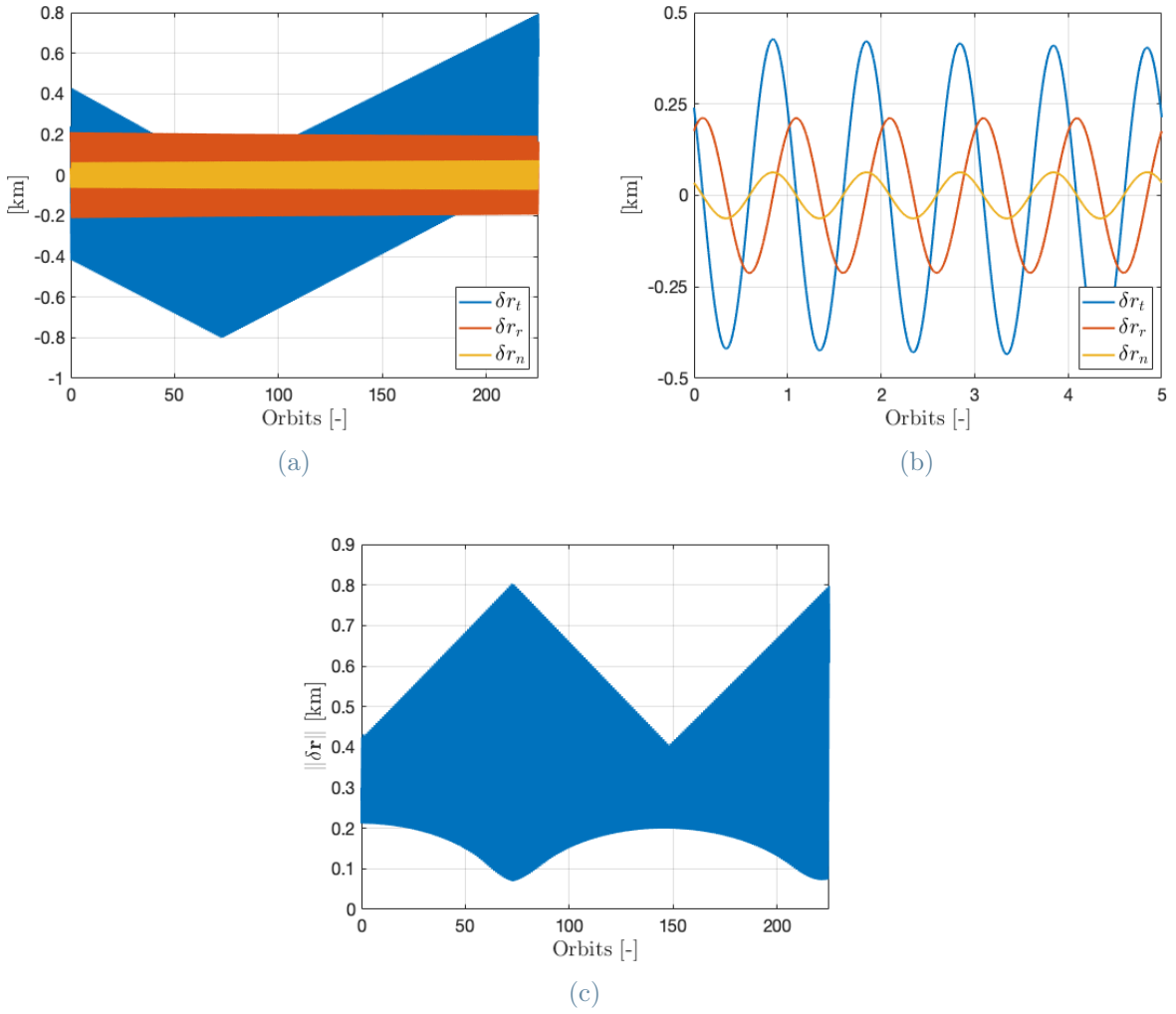

Figure 5.39: Relative positions of the spacecrafts for the first configuration in the case study $h_{2\pi}^{obj} = 150$ m. In (a) and (b) the evolution of the three components of $\delta\boldsymbol{r}$. It can be noted the effect of the along-track recovery phase on δr_t, and the slow long term evolution of the amplitudes δe and δi. In (c) the norm of $\delta\boldsymbol{r}$.

The along-track control strategy implemented proves to be effective in maintaining the relative position between the prescribed maximum boundaries. However, it turns out to have a side effect. Figure 5.39.c shows that close to the 50th orbit the inter-satellite distance violates the lower limit of 150 m imposed for safety. Similarly to what observed for the previous configuration, this behaviour is caused by the relative phases of the three components of $\delta\boldsymbol{r}$. Because of the almost parallel $\delta\mathbf{e}$ and $\delta\mathbf{i}$, when δr_r is at its maximum δr_n is at its minimum, and viceversa. It happens that δr_t follows the same trend of the relative out-of-plane position. But since the norm of $\delta\boldsymbol{i}$ is about 70 m, when the peaks of δr_t get below 150 m because of the drift, the relative distance becomes too small to

ensure a proper safety between the spacecrafts (Figure 5.40). A practical solution to this problem could be to modify the triggers of the along-track control strategy to maintain the peaks of δr_t above 150 m and the valleys below -150 m. The relative trajectory of

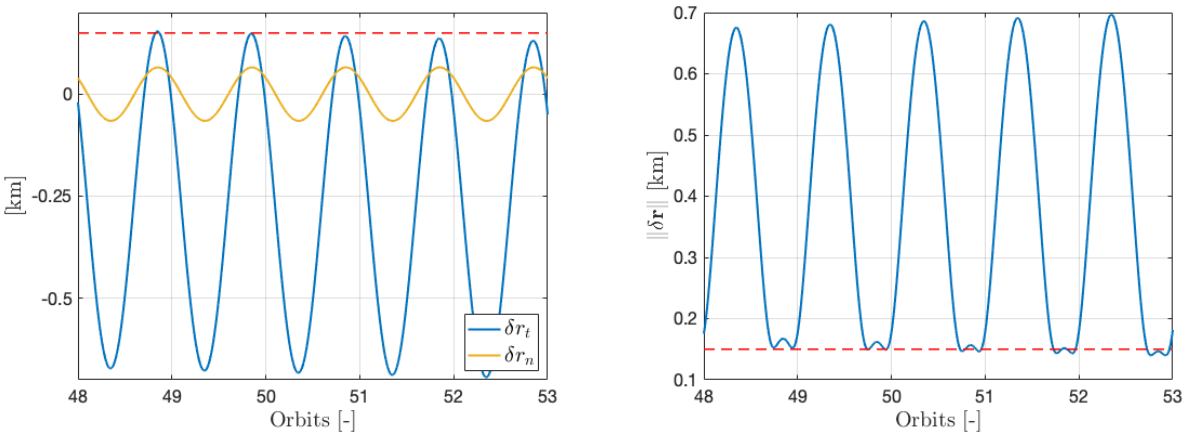

(a) (b)

Figure 5.40: Along-track and out-of-plane relative positions (a) and the violation of the lower boundary for the inter-satellite distance (b).

the deputy for this simulation is reported in Figure 5.41, where it's possible to verify the passive stability of the initial condition found. For clarity, the plot shows exclusively the trajectory for the coasting phase.

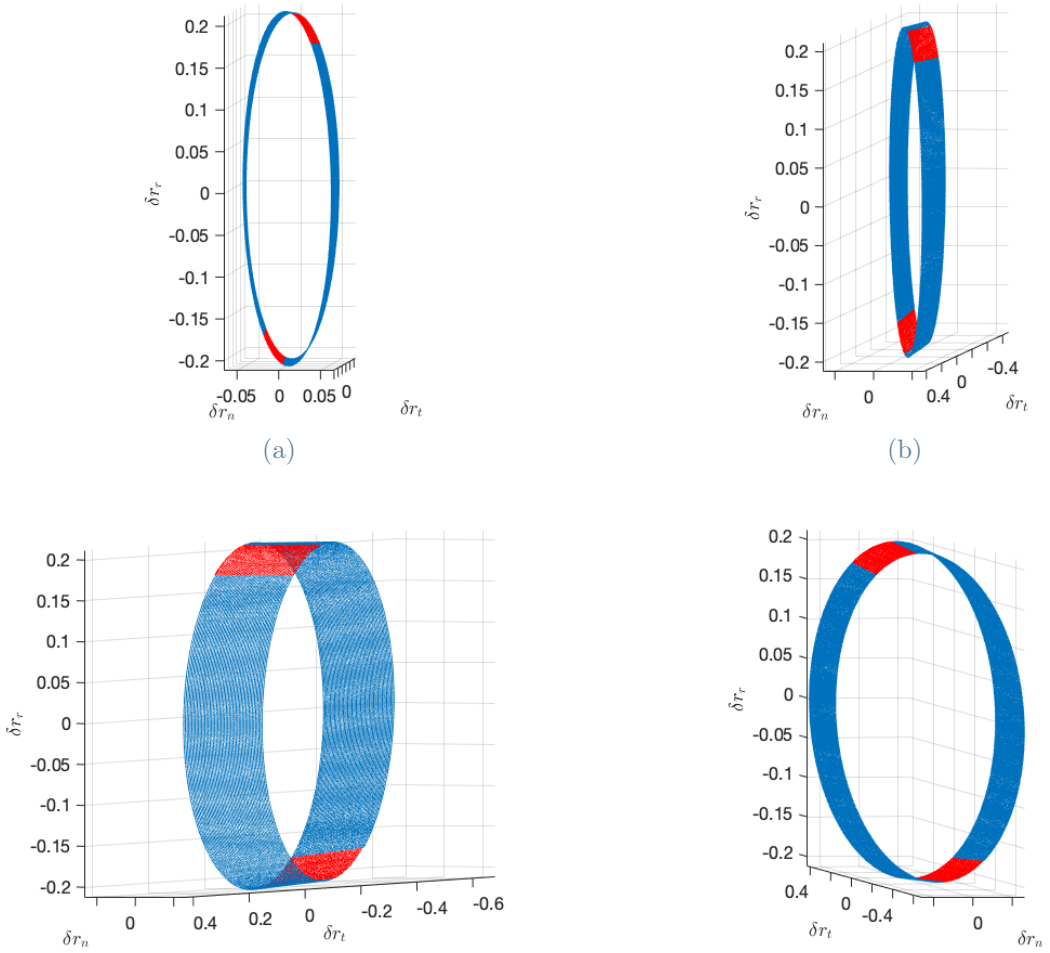

Figure 5.41: Different views of the deputy's relative trajectory. The red parts identify the imaging windows along the orbits.

The second half of the simulation deals with the control of the second configuration. The first interesting result is the plot of the height ambiguity (Figure 5.42), that stays within the 148 m limit for more than 99.98% of the time showing a trend similar to the one of the previous configuration, with the lower boundary of 148 m this time violated twice. In the first part of the simulation, the plot shows an irregular behaviour, lasting about 15 orbits after which the curve enters a stable phase with a slightly spiky behaviour. At the beginning of the along-track recovery, close to orbit 180, the additional impulses cause the plot to overpass the lower boundary. Detecting this violation, the algorithms act to recover the objectives by raising the values of h_{min} in the optimisation of 3 cm. A second stable phase then begins, lasting for the rest of the simulation.
The essential features observed in the height of ambiguity can be recognised also in the

behaviour of u_{in} and u_{out}. The relative shift introduced by the initial orbits of adaption trims around 11% of the original window size ($\approx 2.9°$). The similar shits of u_{in} and u_{out} leave the windows almost unchanged in size, as can be observed in Figure 5.42.d, at least for the phase of coasting. During along-track recovery instead the oscillations introduced by the additional manoeuvres cause the windows to contract of about 0.4 °. The major difference observed with respect to the first configuration is the noisy nature of the results, a characteristic already observed in the previous case study. But as long as these oscillations are confined in the order of tenths of degree, continuity in the scientific activity can be ensured selecting a proper overlay margin between consecutive configurations.

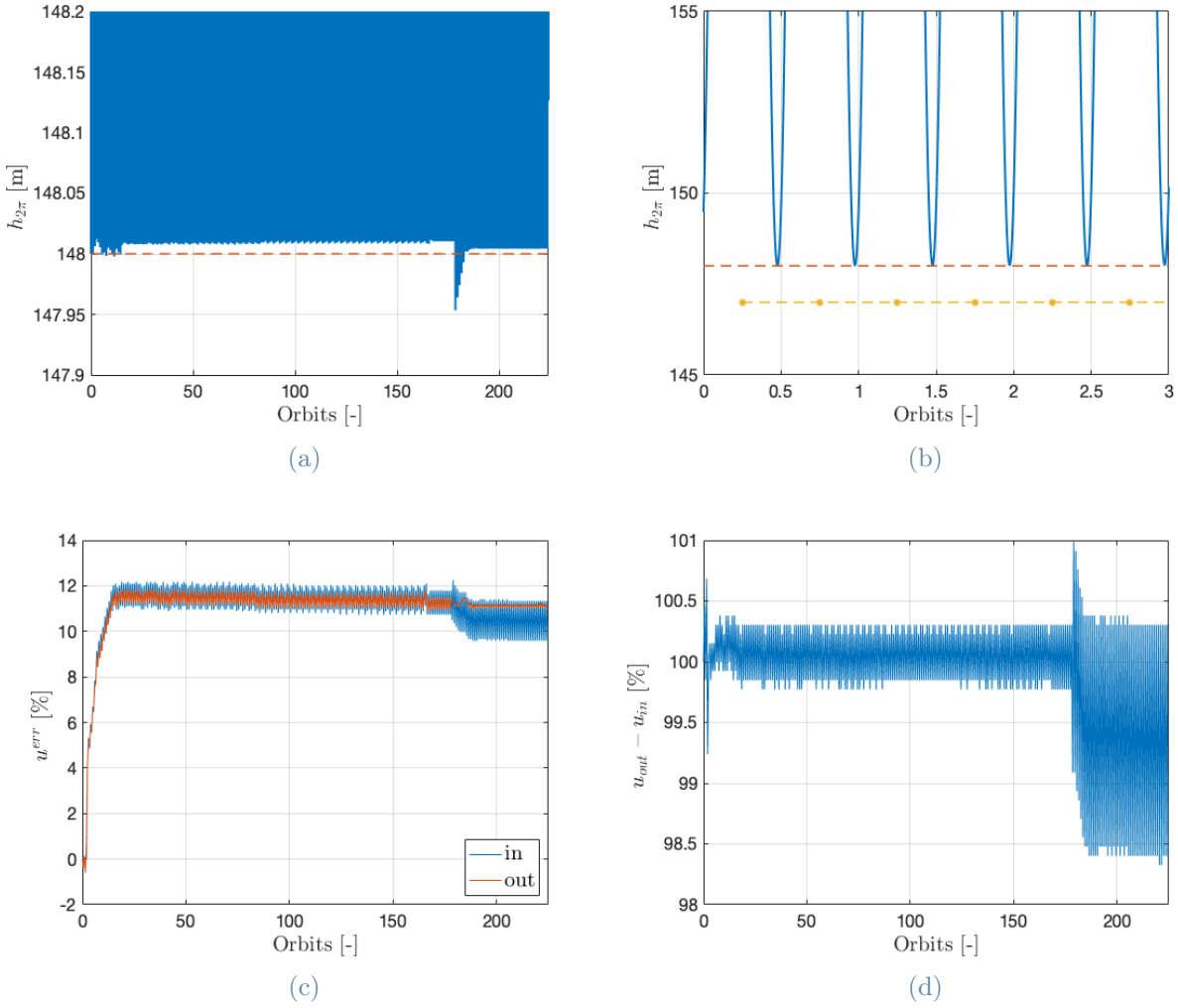

Figure 5.42: Height ambiguity ((a) and (b)) and imaging windows ((c) and (d)) results for the second configuration of the case study $h_{2\pi}^{obj} = 150$ m. The dotted line in (d) represents the average windows size.

A more noisy behaviour is encountered also in the ROE (Figure 5.43), where it's possible to note great similarities within the elements evolution in the previous configuration. The relative semi-major axis is kept close to zero, as expectable at this point of the presentation, with an average of -1 m. The norms of $\delta \boldsymbol{e}$ and $\delta \boldsymbol{i}$ have opposite drifts, and have total variations of similar values. In particular, it is noted that the relative perigee and ascending node maintain similar phases, ensuring again passive safety to the formation with respect to along-track uncertainties. Generally speaking, the ROE show larger excursions with respect to the previous configuration.

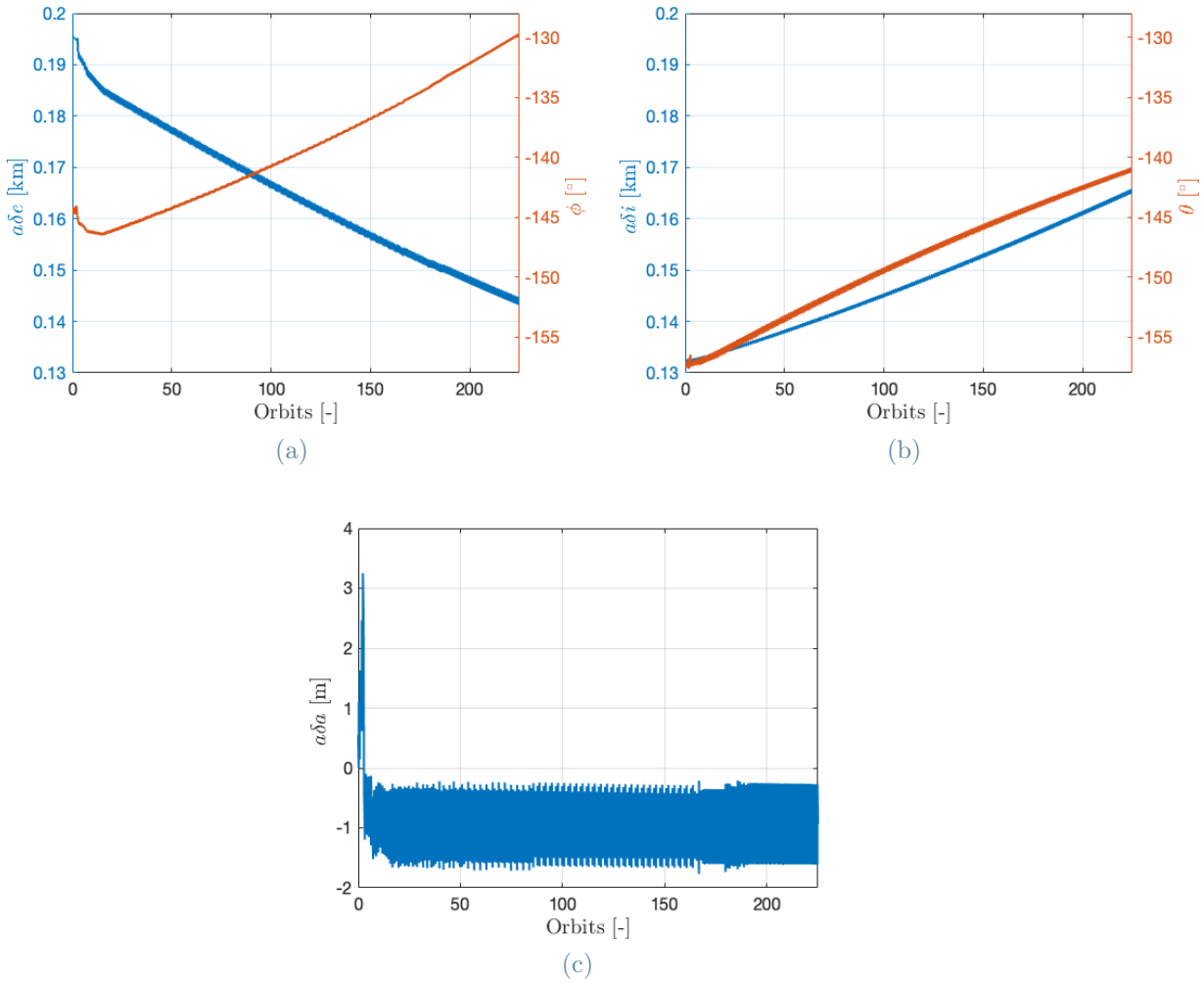

Figure 5.43: Relative orbital elements evolution for the second configuration, in the case study $h_{2\pi}^{obj} = 150$ m. In (a) the relative semi-major axis, in (b) the relative eccentricity vector and in (c) the relative inclination.

To conclude, the components of the relative positions vector are reported in Figure 5.44 together with the norm of $\|\delta \boldsymbol{r}\|$. The along-track position, raised in the previous con-

figuration, as expected shows a decrease, until orbit 178 where the along-track recovery phase begins. The position is correctly recovered and δr_t remains inside the prescribed boundaries for the whole simulation. Because of the relatively small norms of δr_r and δr_n, close to 150 m, the inter-satellite distance gets below the limit of 150 m when the peaks (or the valleys) of the along-track position are close to zero. This already observed condition can be, once again, simply resolved by properly changing the triggers of the control logic.

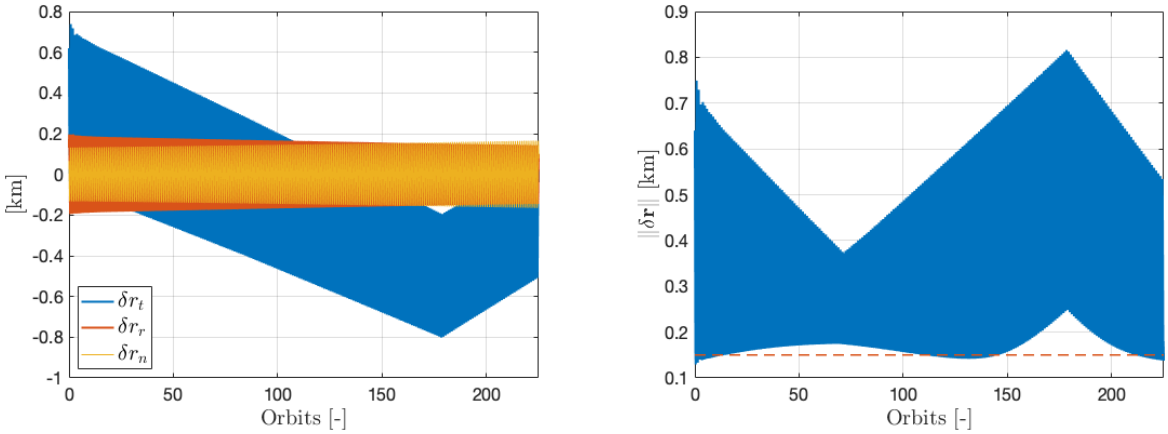

(a) (b)

Figure 5.44: Relative positions for the second configuration of the second case study. Image (a) shows the three components, while in (b) is reported the vector norm. The red dotted line identifies the 150 m boundary.

The overall relative trajectory is reported in Figure 5.45, where it's possible to verify once again the passive stability of the formation with respect to along-track uncertainties.

The solutions found by the algorithms to control the deputy, in terms of impulses, are reported in Figure Figure 5.46 for both the configurations. With respect to the previous case study, the total δv for the first configuration maintenance is approximately doubled, while for the second configuration the results are very similar. Overall, the simulation shows that the correction of the lobes requires on average 37 and 48 mm/s per day, still larger but anyway comparable with the 10 mm/s data from TanDEM-X. By repeating the simulation with a smaller relative ballistic coefficient (0.0001 m^2/kg), the total δv for the first configuration lower to 10.7 mm/s.

All the results achieved in the second case study are summarised in Table 5.9. The algorithm performances are instead not reported, because they're found to be very close to those of the previous case study.

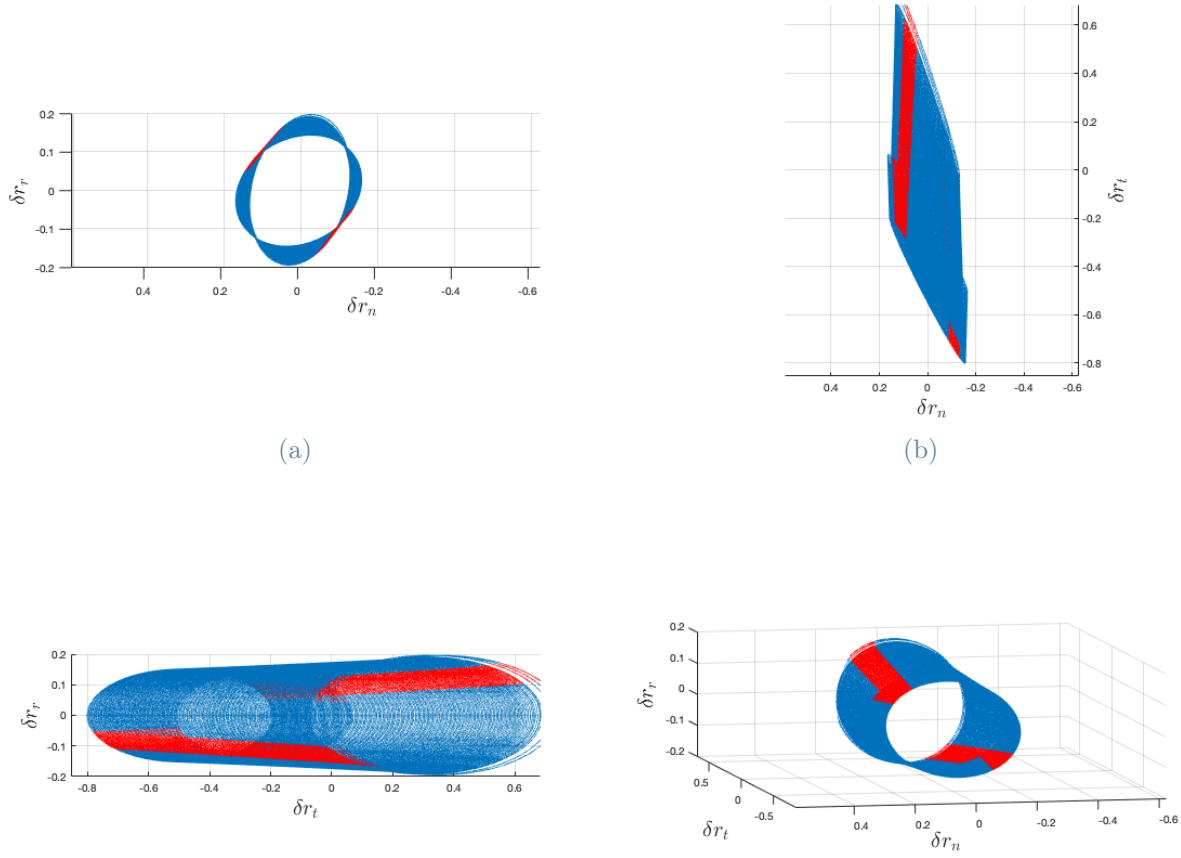

(a) (b)

(c) (d)

Figure 5.45: Relative trajectory of the deputy for the second configuration of the second case study. The red parts along the orbits identify the imaging windows.

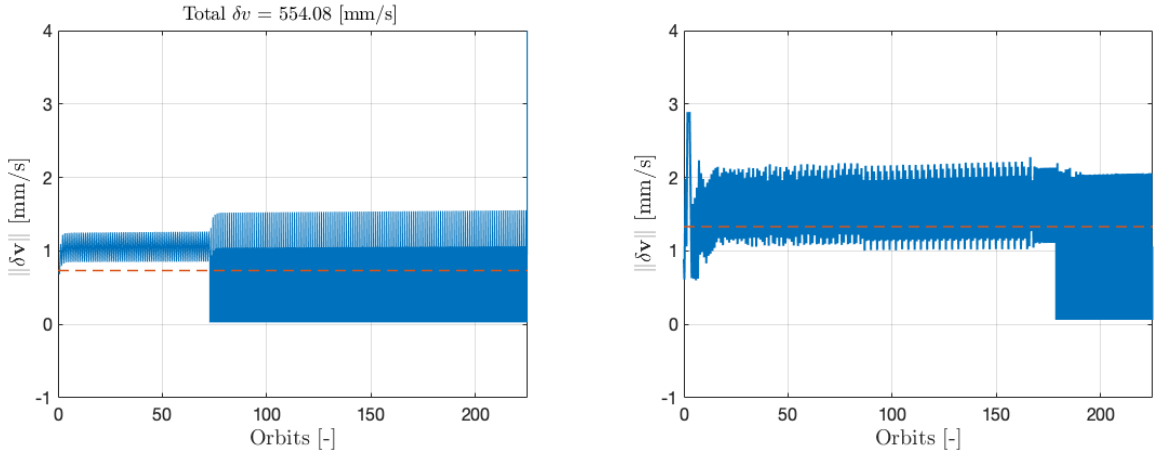

Figure 5.46: Magnitude of the impulses for the first (a) and the second (b) configuration. The dotted lines represent the average values of each configuration.

Parameter	Config. 1	Config. 2
$h_{2\pi} \geq 148$ m	$\geq 99.999\%$ of time	$\geq 99.98\%$ of time
u_{in}^{err}	+ 0.5% (+0.13°)	+ 11% (+2.9°)
u_{out}^{err}	- 0.5% (-0.13°)	+ 11% (+2.9°)
$u_{out} - u_{in}$ %	100.3 % (26.65°)	100.1% (26.66°)
δa average	- 0.6 m	- 1 m
$\Delta\delta e$ (end - start)	- 15 m	- 60 m
$\Delta\phi$ (end - start)	+ 3.5°	+ 15°
$\Delta\delta i$ (end - start)	+ 10 m	+ 30 m
$\Delta\delta\theta$ (end - start)	+ 12°	+ 20°
$\Delta(\delta v_{tot})$	554.09 mm/s	722.15 mm/s
$\Delta(\delta v)$ for recovery	8.14 mm/s (1.47% of total)	5.75 mm/s (0.79% of total)

Table 5.9: Sum up of the results achieved in the two configurations of the second case study.

5.2.2. Reduced Simulation

From the results shown above, is immediate to see that this case study requires more reconfigurations than the previous. Considering an average window size of 26.2°, it is necessary to consider at least eight configurations, to have a sufficient overlap margin. The adequate value for this case study is found to be 4°, corresponding to 15.1% the average size of the imaging windows, again far more than sufficient to cover the excursions observed in the Extended Simulation.

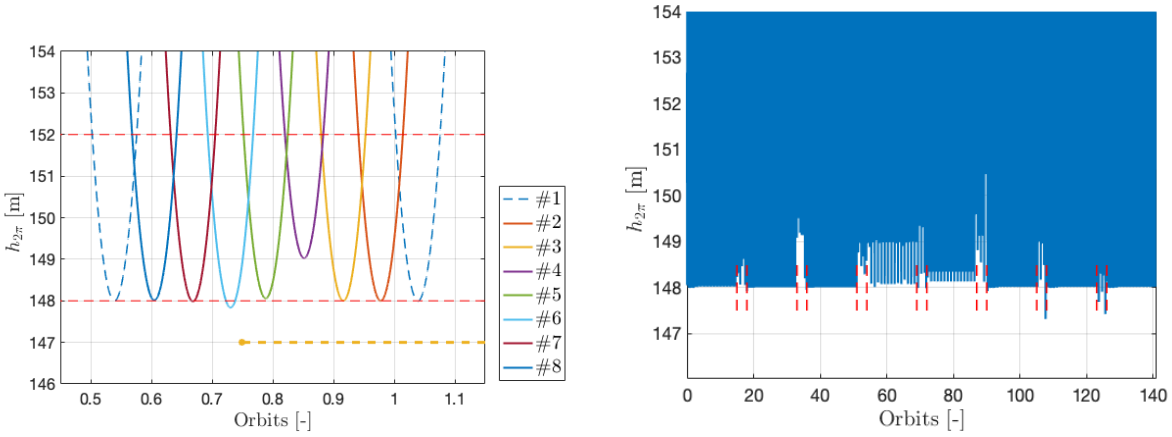

Figure 5.47: Lobes shift after reconfiguration (a) and the overall height of ambiguity (b) for the reduced simulation of the second case study. In (b) the dotted lines delimit the reconfiguration manoeuvres.

The results of the successive reconfiguration manoeuvres are reported in Figure 5.47. As in the previous case, it can be observed how the lobes after each reconfiguration get adequately shifted, remaining sufficiently close to the 148 m limit. Even though small excursions can be noted for some cases, these don't really represent a problem since as it has been extensively observed in this chapter, after each reconfiguration is always present a small transitory in which the lobes might slightly overpass the lower limit. This can be confirmed by looking at Figure 5.47.b, where it's also possible to see the effects of the control window shift introduced for the configurations in which the manoeuvres are executed too close (about 30°) to the imaging windows. The control shift affects mostly the fourth and the fifth configurations. Because of this, as can be observed in Figure 5.48, the overlay margins across these configurations substantially deviate from the 4° objective.

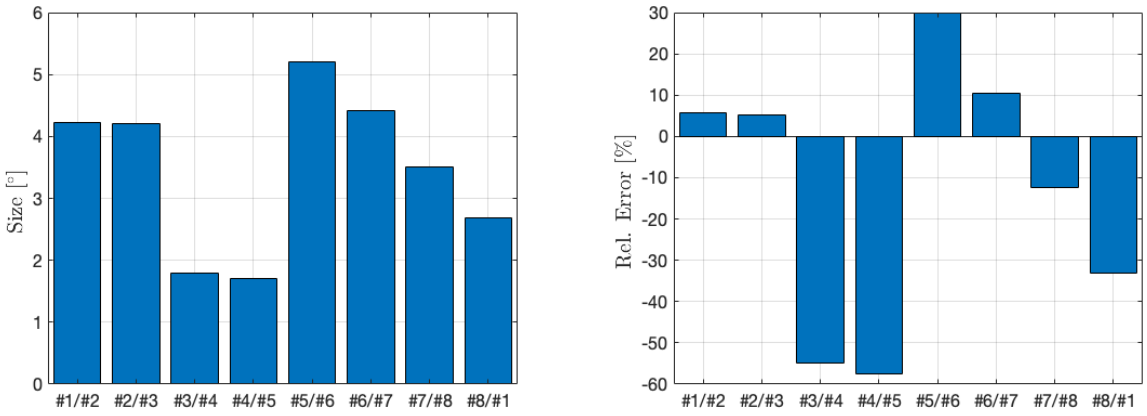

(a) (b)

Figure 5.48: Average overlay margin size (a) and relative error with respect to the 4° objective (b) for the second case study.

During reconfigurations the control algorithms change the ROE to properly shift the location of the lobes. Figure 5.49 shows the most important variations introduced in the relative state vector for the Reduced Simulation.

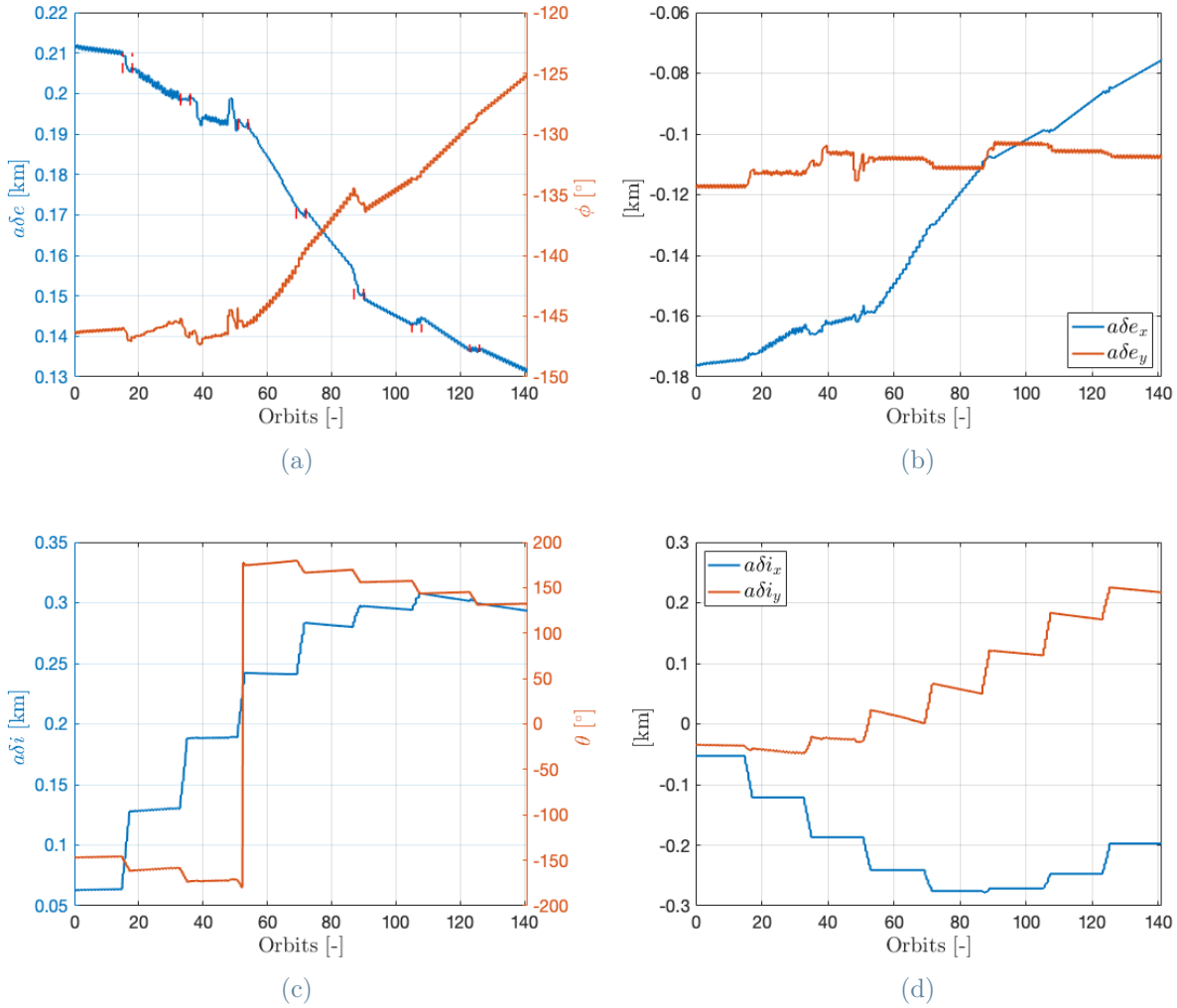

Figure 5.49: Evolution of the relative eccentricity and inclination vectors during the Reduced Simulation, second case study. The vectors are represented both with polar, in (a) and (c), and Cartesian coordinates, in (b) and (d).

The relative eccentricity shows smaller variations this time, both in the norm and in the phase. The greatest variations verify during the one-day scientific activity phases. To shift the lobes, as already observed in the previous case study the algorithm finds it easier to intervene on the relative inclination, changing both in norm and phase. In particular it is noted a regular increase in the norm, along with a decrease in the phase except for the passage between configurations #3 and #4, where the phase changes of 180° because of the passage of δi_y from negative to positive. During scientific activities instead both the norm and the phase remain almost constant.

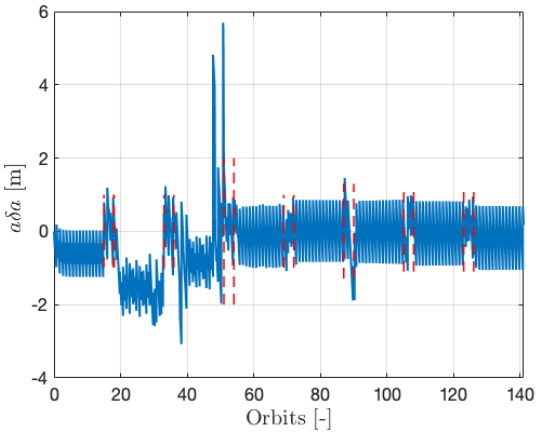

(a)

Figure 5.50: Relative semi-major axis of the Reduced Simulation for the second case study.

The relative semi-major axis instead undergoes more contained excursions with respect to the previous case study for all the reconfiguration phases, coherently with the small variations observed in the relative eccentricity. Again, apparently δa doesn't follow a specific pattern. The transitories (observed especially in the first and the third configurations) are short, and they last up to maximum four orbits. Generally it can be sad that once again, the relative semi-major axis reveals to be a parameter more crucial for the scientific activity, rather than the reconfiguration phases.
The solutions found by the control algorithms in terms of impulses are reported in Figure 5.51 and Table 5.10.

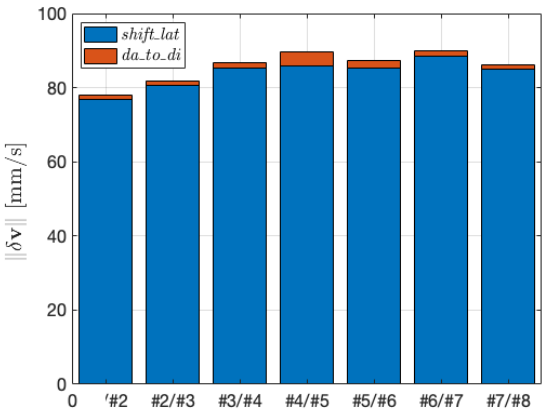

Figure 5.51: $\Delta(\delta v)$ of the reconfiguration manoeuvres for the second case study, categorised by algorithm.

Reconfiguration	$\Delta(\delta v)$ [mm/s]
#1/#2	78
#2/#3	81.9
#3/#4	86.8
#4/#5	89.7
#5/#6	87.4
#6/#7	89.9
#7/#8	86.1
Total	599.8

Table 5.10: Total $\Delta(\delta v)$ for the reconfiguration manoeuvres.

The impulses required for the second case study result to be sensibly cheaper with respect to the previous: even though this time a higher number of reconfigurations is considered, the total necessary δv is lower, because the shift applied to the lobes is lower. The overall behaviour however in general is the same observed before: the various reconfigurations have approximately the same cost, with less than 3% (6% in the fourth reconfiguration) of the δv employed to cancel the variations introduced in the relative semi-major axis.

Algorithm	No. iterations	Duration	No. repetitions
shift_lat	10	40 s	35
da_to_di	5	6 s	7
Reconfiguration simulation time:		26 min	
Scientific activity simulation time:		1 hour 2 min	
Total simulation time:		1 hour 28 min	

Table 5.11: Algorithms performances for the Reduced Simulation of the first case study. For the number of iterations and the duration, the values shown are meant on average.

5.3. Validation Campaign

For each case study the performances and the results of the algorithms presented have been validated through more accurate models. The comparison is carried out with *General Mission Analysis Tool* (GMAT) by NASA, an open-license software that implements refined propagators for mission analysis. The software is employed to propagate the absolute dynamics of the chief and the deputy in the ECI frame subject to perturbations and control actions (only the latter) that simulate the scientific activity phase and the reconfiguration. In particular the simulations are setup to include gravitational potential disturbances expanded up to the fourth order and atmospheric drag with a time-step of 0.316 seconds, that approximately corresponds to the discretisation step of the mean argument of latitude in the linearised model. The properties of the spacecrafts are selected such that the related absolute ballistic coefficients are $\beta_c = 0.1$ m^2/kg and $\beta_d = 0.11$ m^2/kg, in accordance with the term $\Delta\beta = 0.01$ m^2/kg set for the relative dynamics simulations. The validation aims at verifying both the long-term results of the height of ambiguity correction and the lobes shift of the reconfiguration. However, being a more refined model some kind of divergence in the results is to be expected since the algorithms developed rely on linearised equations of motion. Therefore, the validation campaign for both the case studies is structured as follows:

- partial validation of the reduced simulation: a three-days simulation to verify the results of the algorithm *correct_h*

Spacecraft	a [km]	e [-]	i [°]	Ω [°]	ω [°]	ν [°]
Chief	6891	0.0015	97.4671	180	0	0
Deputy	6891	0.0014996	97.4673	179.9979	359.0169	0.9860

Table 5.12: Initial conditions for the validation, expressed in Keplerian orbital elements.

- validation of the reconfiguration: simulation of a single reconfiguration phase considering six manoeuvres.

From the absolute positions of the spacecrafts it is retrieved the relative position of the deputy in the LVLH frame, and the results are compared with those of the linearised model. The height of ambiguity is estimated, for both the models, starting from the relative positions and considering the altitude constant along the orbits.

5.3.1. Case $h_{2\pi}^{obj} = 50$ m

The absolute initial conditions of the spacecrafts for this case study are summarised in Table 5.12.

Science Validation

The first validation aims at verifying whether the control actions computed with the model predictive approach are capable of maintaining a stable height of ambiguity close to the limits imposed. For the first case study, the results of the validation are reported in Figure 5.52.

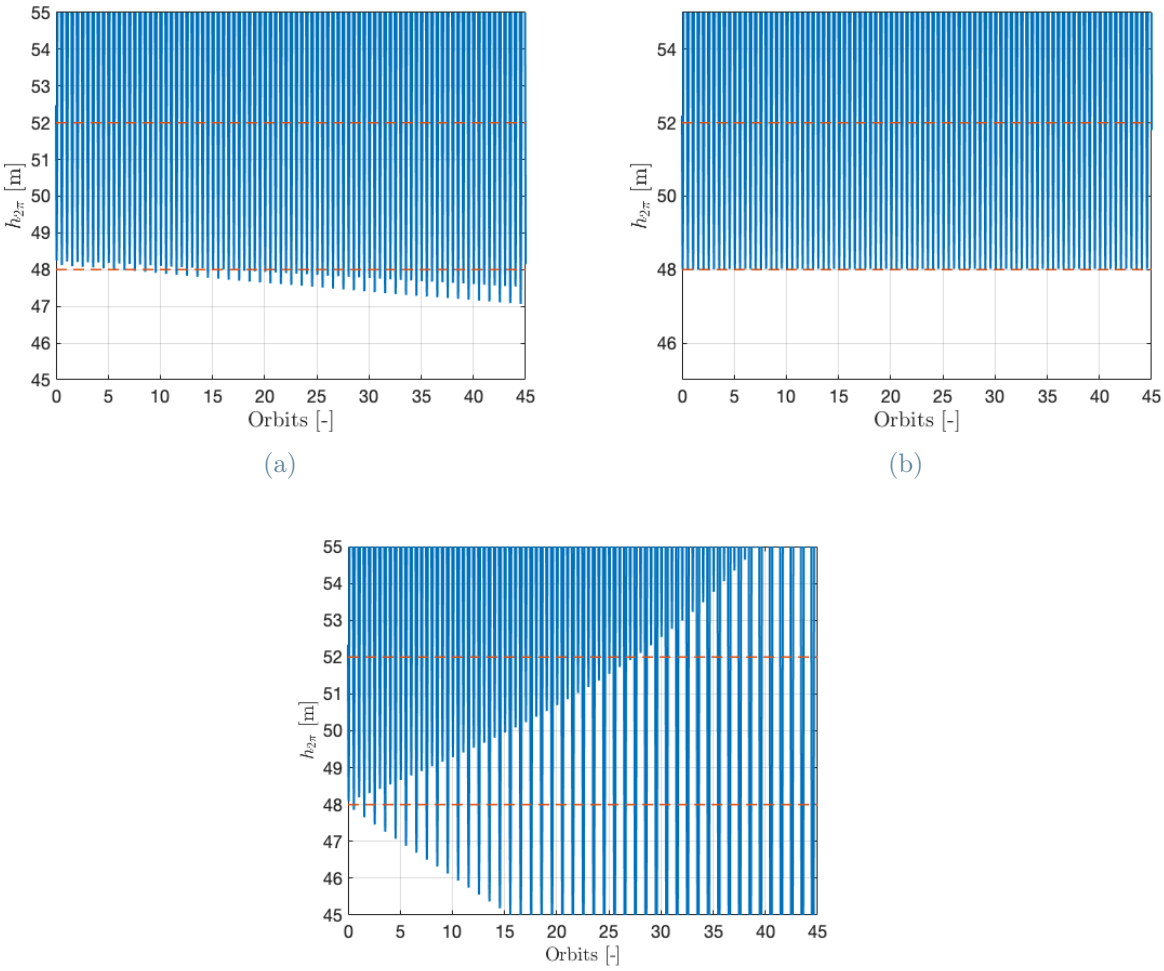

Figure 5.52: Height of ambiguity computed simulating with the validation (a) and the linearised relative (b) dynamics models. Image (c) shows the behaviour of the height of ambiguity in case no control is applied, simulated with the validation model

The first thing to note is the different look of the reference (Figure 5.52.a) and linearised (Figure 5.52.b) solutions. In the first the asymmetry of the lobes in the orbits is more evident, and increases over time. The plot shows that the algorithms are indeed capable of maintaining the curve close to the limits: in the first nine orbits, in particular, the height of ambiguity remains entirely inside the ± 2 m range for the whole imaging windows. Then, due to inaccuracies and divergences between the models, the curve has a drift towards lower altitudes and the minima overpass the 48 m limit. However it is noted that, because of the aforementioned asymmetry, one of the lobes still remains above the 48 m limit for six other orbits.

The results shown become even more significant by comparing them with the free-motion

simulation, in which no control is applied to the deputy (Figure 5.52.c). It's clearly notable the high efficacy of the computed manoeuvres in maintaining the lobes both close to each other and to the 48 m limit, even thought the precision lowers in time. Due to the different level of accuracy of the models, the relative positions show a diverging behaviour when compared, that grows to tents of meters after three days (Figure 5.53), or even hundreds in the case of the along-track position.

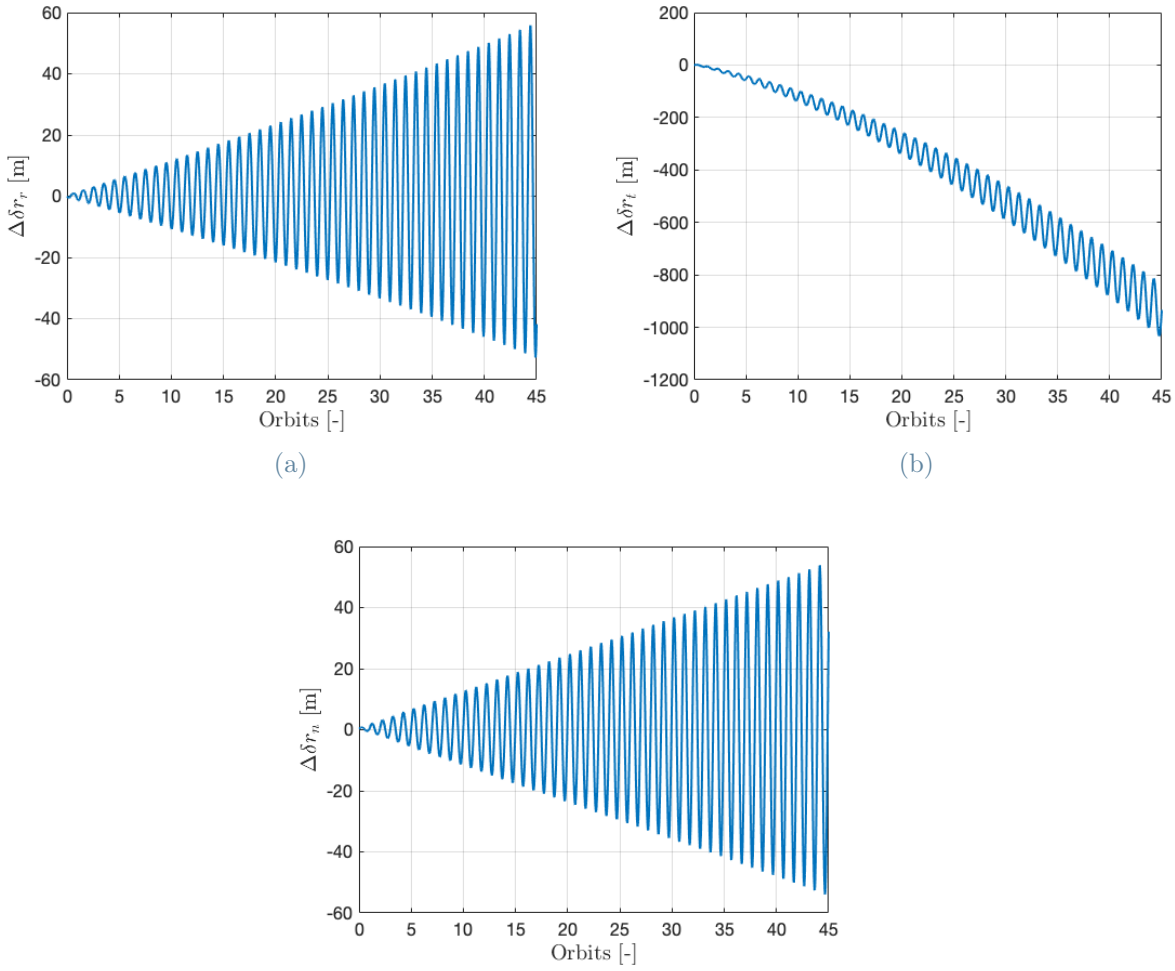

Figure 5.53: Differences in the relative radial (a), tangential (b) and out-of-plane (c) positions between the models.

The large deviations observed in Figure 5.53.b in particular might be given by multiple factors, on top of which a visible drift of the relative semi-major axis, as notable in Figure 5.54. In this picture, the relative semi-major axis computer with the linearised model is compared with the difference in the osculating semi-major axes of the chief and the

deputy computer with the validation model. Even though the linearised model employs short-periodic averaged ROE, from the osculating orbital elements of the validation model it's possible to have a clear insight of the general behaviour of this ROE and its differences in the two models. Other factors that could explain the differences observed in the along-track positions are approximations in the atmospheric drag modelling and a small imprecision in the conversion of the manoeuvre instants from mean argument of latitude of the linearised model to to time, the temporal variable of the validation model, because of truncation errors.

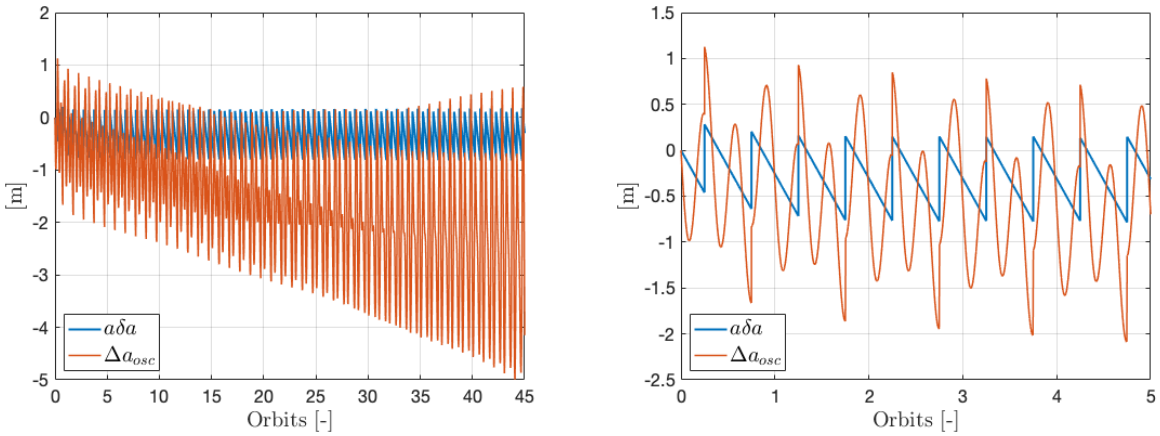

(a) (b)

Figure 5.54: Relative semi-major axis evolution from the linearised model (in blue) and difference between the osculating semi-major axes (in red) coming from the validation model. Image (b) zooms (a) over the first 5 orbits.

Reconfiguration Validation

The second validation aims at verifying whether the HoA can be shifted correctly to another range of latitudes. The initial conditions for this simulation are the same of the first configuration in section 5.1. Figure 5.55 reports the result in the height of ambiguity plot.

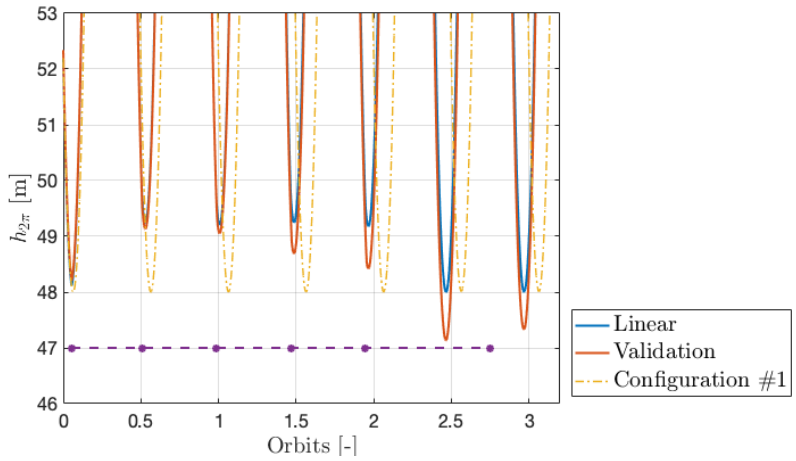

(a)

Figure 5.55: Reconfiguration validation for the first case study. The plot compares the results of the linearised model (in blue) with those of the validation model(in red). To verify the shift, the dotted line represents the behaviour of the HoA during scientific activity with the first configuration. Finally, the purple dots on the bottom identify the maneuvers location.

The results point out that the manoeuvre is successfully conducted: the curves of the two models remain close to each other for all the simulation. The only notable difference is that with the validation model, the lobes show a small overshoot below the 48 m limit. However, in the ideal mission scenario this detail wouldn't represent a problem since during reconfiguration the spacecrafts are not supposed to image the ground. Going deeper, Figure 5.56 reports the differences between the instant u_{in} and u_{out} in the two models.

Spacecraft	a [km]	e [-]	i [°]	Ω [°]	ω [°]	ν [°]
Chief	6891	0.0015	97.467	180	0	0
Deputy	6891	0.0014738	97.4666	179.9997	359.3563	0.6455

Table 5.13: Initial conditions for the second case study validation, expressed in Keplerian orbital elements.

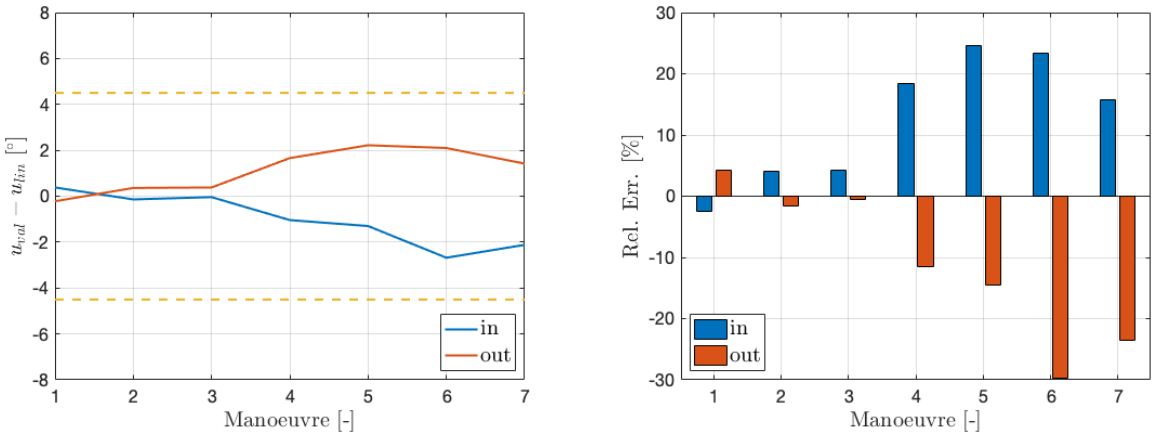

(a) (b)

Figure 5.56: Absoulte (a) and relative (b) errors of u_{in} and u_{out} in the two models. The dotted lines in (a) represent the ±4.5° boundaries for the shift, corresponding to half the selected overlay margin. In (b), the differences between the models are normalised with respect to the overlay margin itself. Point number 7 in both the plots doesn't actually represent a manoeuvre, but the first lobe of the HoA after reconfiguration.

The plots confirm the validity of the manoeuvre showing how, even though the instants u_{in} and u_{out} don't precisely correspond in the two models, the differences in the shifts are safely maintained inside the overlay boundaries for the entire simulation.

5.3.2. Case $h_{2\pi}^{obj} = 150$ m

The initial conditions of the spacecrafts for the second case study are reported in Table 5.13.

Science Validation

The results of the simulation with the validation model are reported in Figure 5.57, compared with those coming from the linearised model.

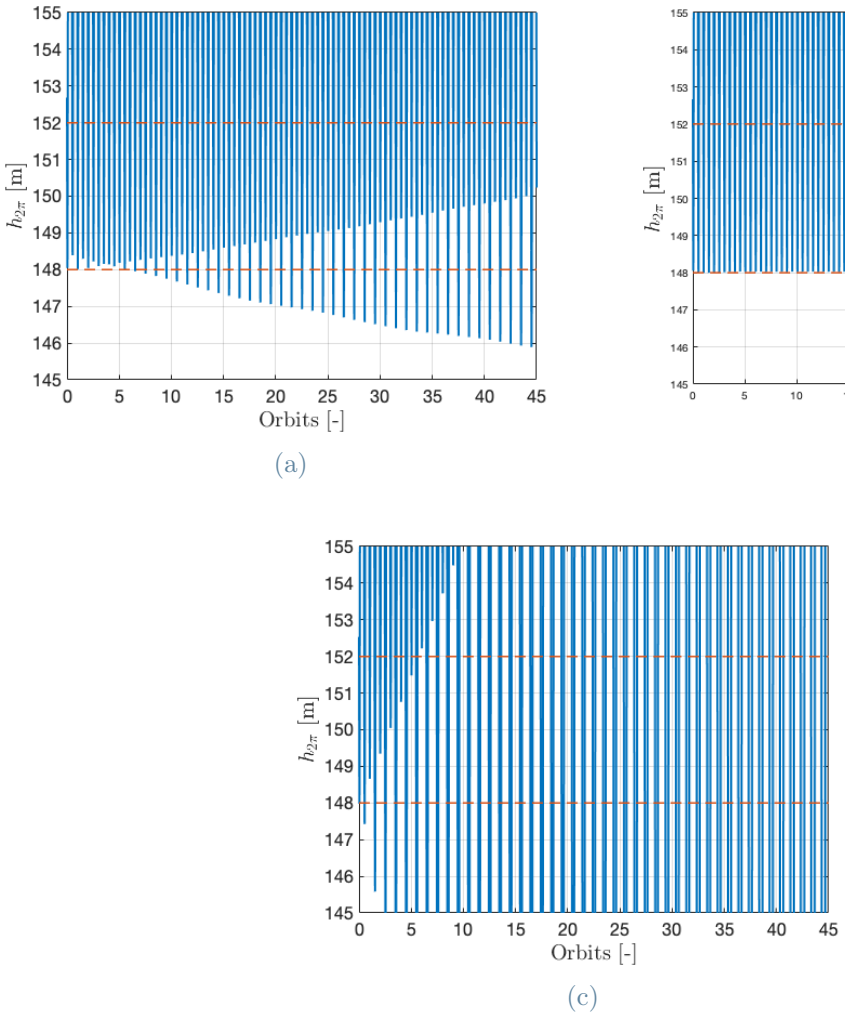

Figure 5.57: Height of ambiguity computed simulating with the validation (a) and the linearised relative (b) dynamics models. Image (c) shows the behaviour of the height of ambiguity in case no control is applied, simulated with the validation model.

Also for this case study the plot shows the effectiveness of the algorithms, at least for the first orbits, in maintaining the lobes close to each other, and close to the lower limit of 148 m. The higher sensitivity of this case study with respect to the previous, already observed in the Chapter, is reflected in a more clearly visible asymmetry inside each orbit that around the 10th orbit acquires a larger importance and separates the lobes couples, always maintaining one of the two inside the ± 2 m interval. The comparison with Figure 5.57 highlights that despite the higher inaccuracy of the last orbits, the control algorithms still maintain the curve close to the desired objective in contrast to the strong drift observable in case no control is applied (Figure 5.57.c).
The differences noted in the validation results are caused by a divergence in the relative

positions estimations of the two models. Figure 5.58 tests the validity of the linearised model differentiating its results from those of the validation model. It is recognised a behaviour analogous to that of the previous case study, with a smaller error on the radial and out-of-plane relative positions.

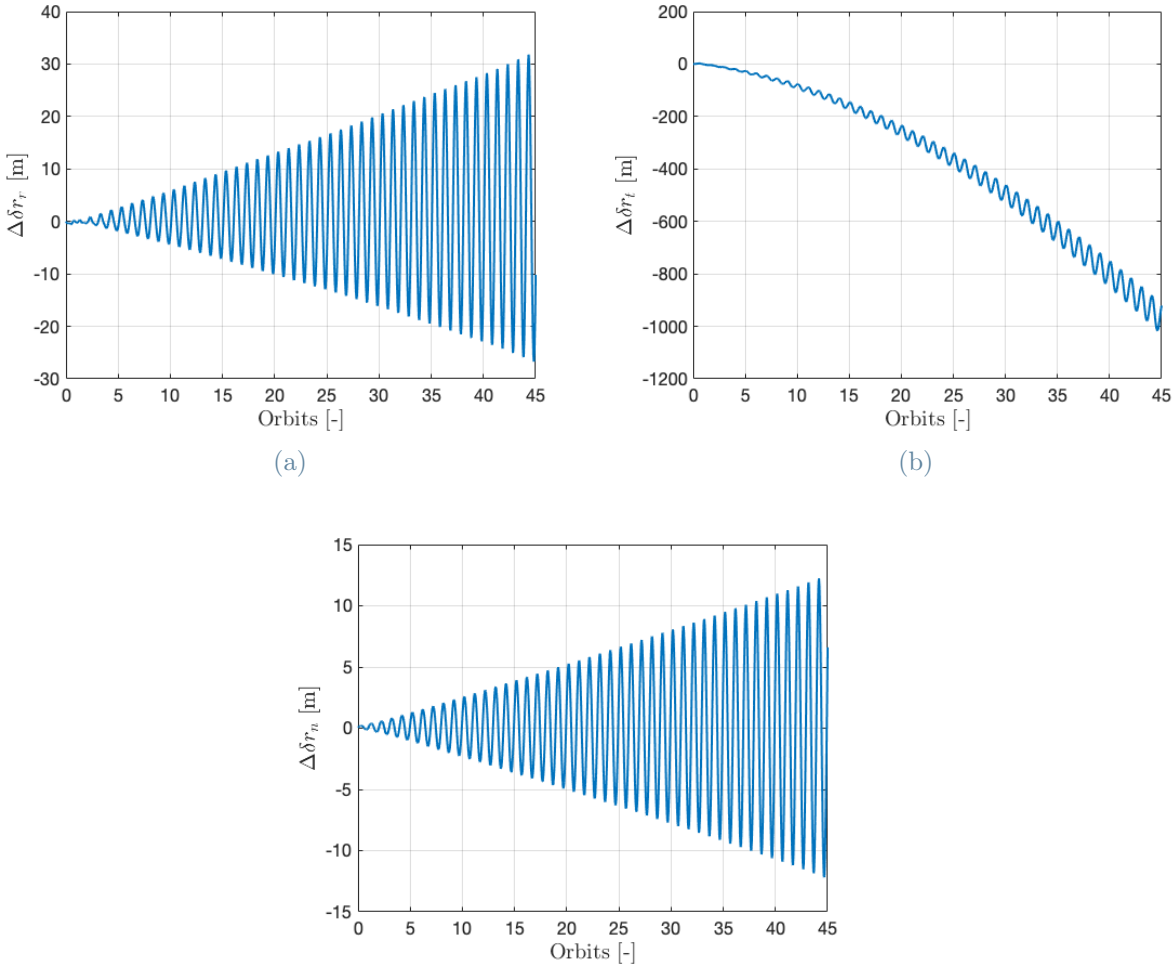

Figure 5.58: Differences in the relative radial (a), tangential (b) and out-of-plane (c) positions between the models.

Even though the absolute errors on the relative positions are lower, their weight on the perpendicular baseline is larger because of the shorter range available for imaging. This can be verified by looking at Figure 5.59, where the errors on $B_\perp$ are reported normalised with respect to the interval $B_\perp^{max} - B_\perp^{min}$. This explains the important differences in the results observed with respect to the previous case study.

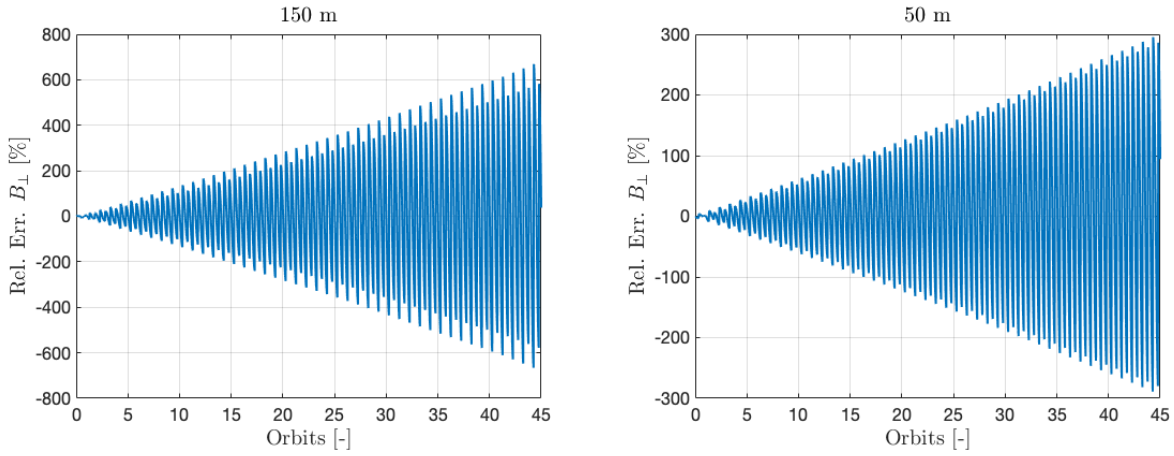

(a) (b)

Figure 5.59: Relative error on the perpendicular baseline for the case study under exam (a), compared to the error of the previous (b). The errors are normalised by respectively 4 and 19 m.

Reconfiguration Validation

The validation of the reconfiguration manoeuvres is reported in Figure 5.60.

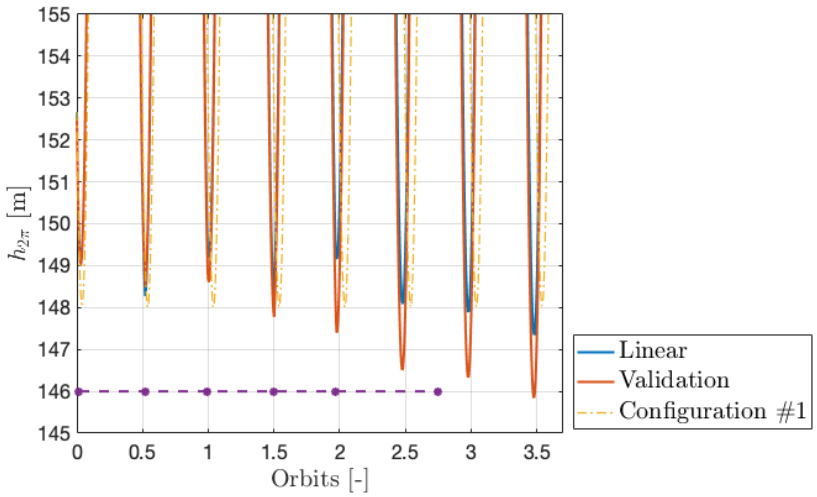

(a)

Figure 5.60: Reconfiguration validation for the second case study. The plot compares the results of the linearised model (in blue) with those of the validation model(in red). To verify the shift, the dotted line represents the behaviour of the HoA during scientific activity with the first configuration. Finally, the purple dots on the bottom identify the maneuvers location.

Also for this case study the plot shows how the two curves remain close to each other in the simulations. To have a more practical insight on the results, Figure 5.61 shows the differences in U_{in} and u_{out} between the two models.

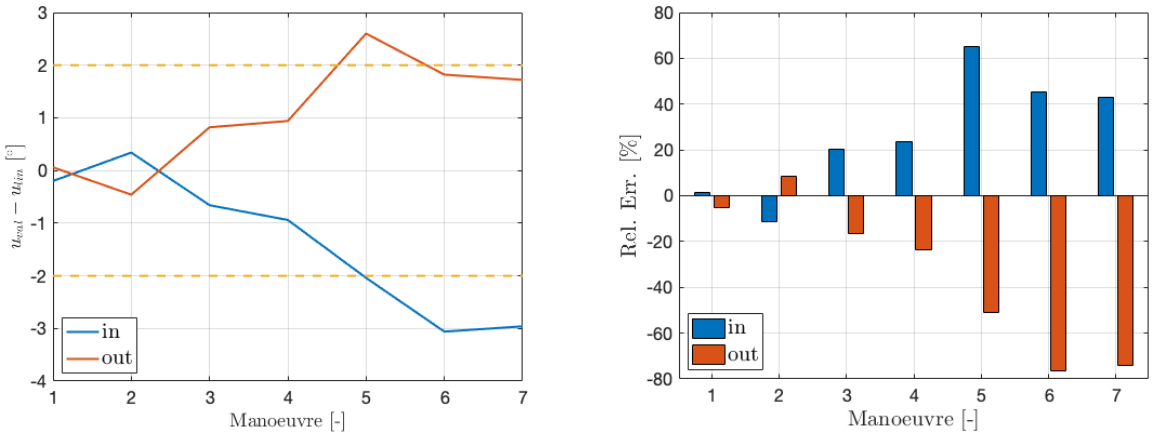

(a) (b)

Figure 5.61: Absoulte (a) and relative (b) errors of u_{in} and u_{out} between the models. The dotted lines in (a) represent the $\pm 2°$ boundaries for the shift, corresponding to half the selected overlay margin. In (b), the differences between the models are normalised with respect to the overlay margin. Point number 7 in both the plots doesn't actually represent a manoeuvre, but the first lobe of the HoA after reconfiguration.

This time, the overlay margin in shorter (4°). The plots show that in the last manoeuvres the shift of u_{in} and u_{out} gets them outside the overlay boundaries. However, it shall be noted that as long as the boundaries get violated in the first five manoeuvres, it doesn't necessary represent a problem. What's important to verify is that the points stay within these boundaries after the last manoeuvre, when the shift of the lobes is concluded. For the case under exam, the instant U_{out} satisfies this condition. Nevertheless, it is also noted that the HoA in Figure 5.60 shows an important overshoot, that inevitably forces u_{in} to back off and u_{out} to push forward. Thus, it is likely that during scientific activities through the control actions also u_{out} would re-enter within the boundaries.

6 | Conclusions and future developments

To resume, the purpose of this thesis was to design and test an approach to SAR satellites formation control starting from defined scientific requirements. With the aim of enhancing autonomous control, and at the same time reducing the complexity of on-board operations opting for a computationally efficient design, the work proposes a control strategy with a Model Predictive approach based on a linearised relative dynamics model to control the deputy spacecraft. To limit the control level on the formation, the strategy tries to exploit the natural formation evolution for scientific activities by counteracting the effects of perturbations when necessary. The results point out that the most important factor to keep into account for the mission design should be to minimise the relative semi-major axis drift by projecting the spacecrafts with ballistic coefficients as similar as possible. However, this may not always be possible, considering for example the class of pure bi-static missions, in which a large transmitter/receiver antenna flies in formation with smaller only-receiving payloads. Therefore, to consider a more general scenario, the simulation have been run employing a relatively high difference between the ballistic coefficients that introduced large drifts in the order of 30 m per day because of drag. By comparing the total impulses necessary with data coming from real missions it was highlighted how, despite the larger number of manoeuvres foreseen, the strategy implemented had a comparable cost, even improvable by selecting more similar ballistic coefficients for the spacecrafts. In the optics of reducing the total mission cost in terms of δv, apart from properly designing the platforms, it could be also thought to exploit the natural dynamics to reconfigure the formation instead of doing it through manoeuvres. In particular with the J_2, letting the relative perigee/ascending node drift to shift the lobes of the HoA over a different range of latitudes. However, given the relatively large time scales (the period of $\delta \boldsymbol{e}$ is ≈ 100 days), attention must be posed because this might strongly extend the mission duration, along with the economical costs.

From the on-board resources point of view, the algorithms developed prove to be very fast in convergence, both in terms of time and number of iterations. Because of unavoidable

limitations in the modelling accuracy, the validation shows a divergence in the relative positions estimation from the linearised model. However, inside the range of a few orbits (ten and six, for the considered case studies), encouraging results suggest that model can be considered valid and the control can be applied to maintain the height of ambiguity and satisfy the scientific requirements. A possible solution to enhance the validity of the results and further develop this work could be to correct the state of the deputy with accurate measurements, for example by implementing a relative navigation system. The major drawback of this solution would be a general increase of the complexity at system level, with the necessity to allocate a substantial fraction of the on-board computational resources to the relative state estimation. Drawbacks, in principle, largely compensated by the advantages of simplified ground operations and control capabilities not limited by visibility windows requirements.

In conclusion, this thesis demonstrates to be a good starting point for a hypothetical mission design. The critical points identified in these months of work are a valid hint for possible future studies in the field on autonomous formation flying SAR satellites, a strongly attractive topic with enormous growth potentialities over the next years.

Bibliography

[1] J.-S. Ardaens, S. D'Amico, D. Ulrich, and D. Fischer. Tandem-x autonomous formation flying system. 04 2008.

[2] F. Bovenga. Special issue "synthetic aperture radar (sar) techniques and applications". *Sensors*, 2020. URL `https://www.mdpi.com/1424-8220/20/7/1851`.

[3] A. Braun. Retrieval of digital elevation models from sentinel-1 radar data–open applications, techniques, and limitations. *Open Geosciences*, 2021. doi: doi:10.1515/geo-2020-0246. URL `https://doi.org/10.1515/geo-2020-0246`.

[4] H. M. Braun and F. Merkle. The new German high-resolution SAR reconnaissance system started its 10-year operations. In J. L. Cox and P. Motaghedi, editors, *Sensors and Systems for Space Applications III*, volume 7330, pages 9 – 14. International Society for Optics and Photonics, SPIE, 2009. doi: 10.1117/12.817521. URL `https://doi.org/10.1117/12.817521`.

[5] J. R. A. C. R. Jackson. *SAR Marine User's Manual*. 2004.

[6] D. Closson and N. Milisavljevic. Insar coherence and intensity changes detection. In *Mine Action*. IntechOpen, 2017.

[7] S. D'Amico. *Autonomous Formation Flying in Low Earth Orbit*. PhD thesis, Politecnico di Milano, 2010.

[8] S. D'Amico, E. Gill, and O. Montenbruck. Relative orbit control design for the prisma formation flying mission. 08 2006. doi: 10.2514/6.2006-6067.

[9] A. S. Facility. Alos phased array type l-band synthetic aperture radar. *Available online: https://asf.alaska.edu/data-sets/sar-data-sets/alos-palsar/alos-palsar-about/*, 2020.

[10] H. Fiedler, G. Krieger, M. Werner, K. Reiniger, M. Eineder, S. D'Amico, E. Diedrich, and M. Wickler. The tandem-x mission design and data acquisition plan. page 4, 05 2006.

[11] A. J. . M. O. Gaias, G. Model of j2 perturbed satellite relative motion with time-varying differential drag. *Celestial Mechanics and Dynamical Astronomy*, 2015.

[12] M.-H. Ka, P. E. Shimkin, A. I. Baskakov, and M. I. Babokin. A new single-pass sar interferometry technique with a single-antenna for terrain height measurements. *Remote Sensing*, 2019.

[13] M. Kirschner, O. Montenbruck, and S. Bettadpur. Flight dynamics aspects of the grace formation flying. pages 1–8, 01 2001.

[14] X. Liu and P. Lu. Solving non-convex optimal control problems by convex optimization. *Journal of Guidance Control and Dynamics*, 37, 04 2014. doi: 10.2514/1.62110.

[15] S. D. J.-S. A. O. Montenbruck, R. Kahle. Navigation and control of the tandem-x formation. *The Journal of the Astronautical Sciences*, 2008.

[16] S. D. S. B. O. Montenbruck, M. Kirschner. E/i-vector separation for safe switching of the grace formation. *Aerospace Science and Technology*, 2006.

[17] S. W. Paek, S. Balasubramanian, S. Kim, and O. de Weck. Small-satellite synthetic aperture radar for continuous global biospheric monitoring: A review. *Remote Sensing*, 12(16), 2020.

[18] A. Pepe and F. Calò. A review of interferometric synthetic aperture radar (insar) multi-track approaches for the retrieval of earth's surface displacements. *Applied Sciences*, 2017.

[19] F. R. D. G. Pietro Guccione, Andrea Monti Guarnieri and N. Gebert. Along-track multistatic synthetic aperture radar formations of minisatellites. *MDPI*, 2020.

[20] F. A. Rocca F., Prati C. An overview of sar interferometry. *Available online: https://earth.esa.int/workshops/ers97/program-details/speeches/rocca-et-al/*, 2014.

[21] L. V. S. Boyd. *Convex Optimization*. 2004.

[22] R. L. S. D'Amico, J.-S. Ardaens. Spaceborne autonomous formation flying experiment on the prisma mission. *Journal of Guidance, Control, and Dynamics*, 2011.

[23] S. Silvestrini and M. Lavagna. Neural-aided gnc reconfiguration algorithm for distributed space system: Development and pil test. *Advances in Space Research*, 67(5):1490–1505, 2021. ISSN 0273-1177. doi: https://doi.org/10.1016/j.asr.2020.12.014. URL `https://www.sciencedirect.com/science/article/pii/S027311772030870X`.

[24] S. Silvestrini, J. Prinetto, G. Zanotti, and M. Lavagna. Design of robust passively safe relative trajectories for uncooperative debris imaging in preparation to removal. 08 2020.

[25] C. Stringham, G. Farquharson, D. Castelletti, E. Quist, L. Riggi, D. Eddy, and S. Soenen. The capella x-band sar constellation for rapid imaging. In *IGARSS 2019 - 2019 IEEE International Geoscience and Remote Sensing Symposium*, pages 9248–9251, 2019. doi: 10.1109/IGARSS.2019.8900410.

[26] A. Torre and P. Capece. Cosmo-skymed: The advanced sar instrument. In *Proceedings of 5th International Conference on Recent Advances in Space Technologies - RAST2011*, pages 865–868, 2011. doi: 10.1109/RAST.2011.5966966.

[27] D. Vallado. *Fundamentals of Astrodynamics and Applications*. 2001.

[28] F. D. Zan. Esa radar remote sensing course. ESA, DLR, 2012.

[29] M. Zink, A. Moreira, M. Bachmann, B. Bräutigam, T. Fritz, I. Hajnsek, G. Krieger, and B. Wessel. Tandem-x mission status: The complete new topography of the earth. In *2016 IEEE International Geoscience and Remote Sensing Symposium (IGARSS)*, pages 317–320, 2016. doi: 10.1109/IGARSS.2016.7729075.

List of Figures

List of Tables

List of Symbols

Variable	Description	SI unit
$\boldsymbol{a}$	semi-major axis	km
$\boldsymbol{e}$	eccentricity	-
$\boldsymbol{i}$	inclination	rad
$\boldsymbol{B_\perp}$	perpendicular baseline	km
$\boldsymbol{H}$	orbit altitude	km
$\boldsymbol{h_{2\pi}}$	height of ambiguity	m
$\boldsymbol{L_a}$	antenna lenght	m
$\boldsymbol{S_g}$	swath width	km
$\boldsymbol{R}$	range distance	km
$\boldsymbol{u}$	mean argument of latitude	rad
$\boldsymbol{u}_M$	mean argument of latitude of manoeuvre	rad
$\boldsymbol{\beta}$	ballistic coefficient	m^2/kg
$\boldsymbol{\gamma}$	coherence	-
$\boldsymbol{\delta_a}$	azimuth resolution	m
$\boldsymbol{\delta_r}$	range resolution	m
$\boldsymbol{\delta a}$	relative semi-major axis	km
$\boldsymbol{\delta e}$	relative eccentricity	km
$\boldsymbol{\delta i}$	relative inclination	km
$\boldsymbol{\delta r}$	relative position	km
$\boldsymbol{\delta \lambda}$	relative mean argument of latitude	rad
$\boldsymbol{\theta}$	relative ascending node	rad
$\boldsymbol{\theta_L}$	look angle	rad
$\boldsymbol{\lambda}$	wavelength	m
$\boldsymbol{\phi}$	relative perigee	rad
$\boldsymbol{\Omega}$	right ascension of the ascending node	rad
$\boldsymbol{\omega}$	argument of perigee	rad

Acknowledgements

I ringraziamenti. La parte più riservata, ed emotiva, della tesi. Ho pensato a lungo, nelle molte notti di lavoro come questa, infinite, eppure giunte a una fine, a cosa avrei scritto qui. A chi avrei citato. E perchè l'avrei fatto.
Il tutto rigorosamente in italiano, perchè è la lingua più bella del mondo.
Due anni non sono molti, eppure sono successe così tante cose che ho perso il conto. Per come sono fatto, quando sto con qualcuno abbastanza a lungo da cominciare a conoscerlo, cerco sempre i punti di forza in quella persona e provo ad imparare come metterli in pratica. Provo a farli miei, seguendo il suo esempio. Non so perchè lo faccia, è istintivo, ma mi permette di entrare più facilmente in contatto con le persone. In cambio cerco di dare del tempo denso, di valore, da passare in mia compagnia come segno di riconoscimento. Per questo la lista dei nomi da citare sarebbe molto più lunga di quanto mi è concesso. Non me ne vogliano, le persone che non sono riuscito a includere. Sarò più che felice di offrivrvi un caffè per sdebitarmi, la prossima volta che ci incontreremo.
Abbastanza canonicamente, i miei primi ringraziamenti vanno alla mia Famiglia. Ma non per mancanza di fantasia, o alto. Perchè sono le persone che più a lungo hanno convissuto con il Federico sotto esami, o il Federico che stava lavorando alla tesi, o un sacco di altre versioni di me poco raccomandabili. Queste sono più che altro delle scuse, travestite da ringraziamenti. I veri ringraziamenti arrivano quando dico che vi sono grato per la pazienza, e il supporto che mi avete dato nei momenti giusti, quando ne avevo più bisogno. Per le esperienze fantastiche che mi avete permesso di vivere in questi anni. Ringrazio Fra e Pes, i miei compagni di vita, e di sventure, perchè il nostro è uno di quei legami che "nel bene, e nel male". Avete reso tutto più leggero, più affrontabile. Non so come avrei fatto senza di voi e non so se vi ringrazierò mai abbastanza. Ringrazio Teo e Michi, perchè siamo legati nonostante le differenze negli interessi e nel modo di essere di ognuno. È sempre bello trovarsi e passare una serata con voi, vi voglio bene ragazzi. Ringrazio la dolce, fragile, resiliente Betta, per il supporto che ci siamo dati a vicenda nei momenti più bui di questi anni. Vorrei ringraziare anche i miei compagni di università, o meglio i miei colleghi, i miei amici. Ringrazio Alessandra, per avermi dato così tanto che non basterebbero venti pagine per scriverlo. Ringrazio quell'uomo di cultura che è

Emi, il saggio Teo e il nobile Mane, il famigerato triumvirato, per essere ognuno pazzo a modo suo. Tutti i ragazzi di "La Rosa News 24", perchè insieme abbiamo affrontato ostacoli giganteschi. È inevitabile che ognuno abbia preso la propria strada, ma mi avete fatto passare i cinque anni migliori della mia vita. Ringrazio Jorge, per tutte le nostre serate in videochiamata passate a bere birre, lavorare per SMAD e a giocare a scacchi o Pokèmon Showdown. Ringrazio tutti i membri di Polispace: ragazzi increbili, brillanti e determinati. Sono fiero di aver lavorato con voi. Mi avete fatto sentire una parte piccola, ma fondamentale, di questo enorme progetto e auguro ad ognuno di voi il meglio nella vita. Ringrazio Amir e la sua mente libera, indomabile. Ringrazio la prof. Lavagna per avermi dato l'opportunità di lavorare a questo progetto, e ringrazio il mio co-relatore Stefano, per tutto l'aiuto che mi ha dato. Pure a Sant'Ambrogio :'). Infine, vorrei dire grazie a un'ultima persona, che ho imparato ad amare e a rispettare in questi anni. Quella che ha saputo stupirmi più di tutti, che ha saputo dimostrarmi di valere davvero. La persona con cui ho litigato di più, ma che ho imparato a perdonare e confortare nel momento del bisogno.
Ringrazio me stesso.
Per tutte le scelte corrette, e soprattutto per quelle sbagliate. Per aver attraversato il Paradiso e l'Inferno con coraggio e con timore, sicurezza incrollabile e fragilità paralizzante, Dante e Virgilio allo stesso momento.
Grazie.

See you, space cowboy.